Summer 2021

Numerical and experimental study of mechanical properties for Laser Metal Deposition (LMD) process part

Lan Li

Department: Mechanical and Aerospace Engineering

NUMERICAL AND EXPERIMENTAL STUDY OF MECHANICAL PROPERTIES FOR LASER METAL DEPOSITION (LMD) PROCESS PART

by

LAN LI

A DISSERTATION

Presented to the Graduate Faculty of the

MISSOURI UNIVERSITY OF SCIENCE AND TECHNOLOGY

In Partial Fulfillment of the Requirements for the Degree

DOCTOR OF PHILOSOPHY

in

MECHANICAL ENGINEERING

2021

Approved by:

Frank Liou, Advisor
Ashok Midha
Cheng Wang
K.M. Isaac
Akim Adekpedjou

PUBLICATION DISSERTATION OPTION

This dissertation consists of the following four articles, formatted in the style used by the Missouri University of Science and Technology:

Paper I: Pages 7-38, has been published by *International Journal of Advanced Manufacturing Technology*.

Paper II: Pages 39-71, has been published by *International Journal of Advanced Manufacturing Technology*.

Paper III: Pages 72-103, has been submitted to *International Journal of Precision Engineering and Manufacturing-Green Technology*.

Paper IV: Pages 104-134, has been published by *Materials*.

ABSTRACT

Laser Metal Deposition (LMD), also called as, Laser Engineered Net Shaping (LENS), Directed Energy Deposition (DED), is a typical Additive Manufacturing (AM) technology, is used for advanced free-form fabrication. It creates parts by directly melting materials and depositing them on the workpiece layer by layer. In this process, the metal powder or fiber is melted within the melting pool by laser beam or electron beam and quickly solidifies to the deposited layer. LMD technology shows great advantages over traditional manufacturing on complex structure fabrication, including high building rates, easy material replacement and reduced material waste. These merits make the wide application of this technology in industry, such as new components fabrication and parts repairing manufacturing, coatings, rapid prototyping, tooling, repair, etc.

The proposed project is to investigate the key parameters to improve the mechanical properties of different fabricate parts in LMD manufacturing by combined approach of experimental analysis and FEA simulation method. Therefore, several sets of experiments will be designed to reveal the processing parameters on properties of deposited components in the method of LMD process. The microstructure, Vickers hardness, phase identification, tensile properties of LMD parts are measured to investigate the fabricated qualities. The features of thermal stress and deformation involved in the DMD process were predicted by the FEA model. This work helps to fully study the thermal analysis to analyze the temperature profile, cooling rate and temperature gradients on microstructure and residual stress, which further influences the engineered mechanical properties of build parts.

ACKNOWLEDGMENTS

First and foremost, I would like to extend my highest respect and most heartfelt thanks to my advisor, Dr. Frank Liou, for his extensive professional knowledge, rigorous academic attitude, selfless work spirit, and honest demeanor have benefited me a lot during my Ph.D. study at Missouri University of Science and Technology, and these wealth will surely benefit me throughout my life. He patiently guided me through every stage of my research while granted me a great deal of independence. He gave me careful guidance and full support from the topic selection of the dissertation, the implementation of the dissertation to the finalization of the final dissertation.

I would also like to extend my appreciation to all my dissertation committee members, Dr. Ashok Midha, Dr. Cheng Wang, Dr. K.M. Isaac, Dr. Akim Adekpedjou. Without their patient support and valuable comments, it would have been impossible for me to complete my dissertation. This dissertation was supported by the Laser Aided Manufacturing Processes (LAMP) Laboratory, and Center for Aerospace Manufacturing Technologies (CAMT), which are gratefully acknowledged.

I would like to express my deep thanks to my lab-mates and friends, Mr. Todd Sparks, Mr. Aaron Flood, Mr. Xinchang Zhang, Mr. Yitao Chen, Mr. Mianqing Yang, and Ms. Wenyuan Cui for their support during my PhD study in Rolla.

Last but not the least, I wish to extend my special and sincere thanks to my parents and my husband for their love and unwavering support.

TABLE OF CONTENTS

LIST OF ILLUSTRATIONS

PAPER I Page

PAPER II

PAPER III

PAPER IV

LIST OF TABLES

SECTION

1. INTRODUCTION

1.1. BACKGROUND

The laser metal deposition (LMD) technique, also known as the laser engineered net shaping (LENS), directed metal deposition (DMD), is a layer by layer additive manufacturing (AM) process that can build fully dense complex parts following CAD data by layered deposition [1]. In this process, the deposited material is melted by the high-power laser with a very small concentration area to create a melt pool. Irradiating by the laser energy, the newly adding material undergoes melting and cooling cycles, and then solidifies to form a deposition, thereby forming a good bond between two materials. The next layer is then built upon the previous one, resulting in a 3D part. Because of the layer after layer building manner, LMD technique has the possibility to design internal features and does not require special tooling, thus it has many benefits compared with traditional manufacturing techniques, such as casting or powder metallurgy [2]. This encourages a variety of metallic parts fabricated by LMD, such as stainless steels (304L, 316L, 17-4PH), Co-Cr alloys (Co28Cr6Mo), tool steels (H13) [3-4], Ni-based superalloys (Inconel 625, Inconel 728), Ti-based alloy (commercial purity grade 1 and 2, Ti-6Al-4V) [5-6], functionally gradient materials (304 SS to Ti-6Al-4V, 304 SS to Inconel 625, 316 SS to Ti-6Al-4V, Cu to Inconel 718) [7].

While producing a component with LMD process, controlling and improvement on final product quality is affected by temperatures history, residual states,

microstructures, and mechanical properties, key factors for AM process. Thermal input and distributions controls melt pool configuration, over and insufficient melting, which has an important influence on the formation of the microstructure. Mechanical properties of LMD parts depend primarily on their microstructure (e.g. grain size and morphology), which, in turn, is influenced by the thermal history during manufacturing, i.e. cooling rates, thermal gradients and reheating cycles. Careful characterization of part microstructure under various process settings is pivotal toward understanding process–property relationships. In addition, defects are frequently formed during LMD process, which can be detrimental to mechanical properties and microstructures of a component. The cooling and solidification rates [8] during the LMD process, determined the microstructure, composition and phase of the fabricated components based on the comprehensive experiments. Wang et al. [9] studied the effect of processing parameters on the microstructure and tensile mechanical properties of the LMD part using stainless steel 304L powder. In their study, the linear heat input could result in the anisotropic and heterogeneous microstructure and tensile mechanical properties within the component. The heat treatment also makes an impact on the microstructures and properties [10-11]. Lin et al. found out the age-hardening occurred in the temperate range between 350-950 °C. The formation of the brittle sigma phase was detected around 1273K, which could restrict their usage in high temperatures. FCC phase was formed at the grain boundaries after ageing, which helped to improve the ductility but decrease the yield strength.

Due to the highly localized heat input and short interaction time, large temperature gradients and high cooling rates are present [12-13]. These unique thermal features dramatically affect as-built microstructures and lead to high residual stresses in

AM built products, which in turn govern their macroscopic performances [14-15]. Moreover, the inevitably formed defects during the AM processes will significantly deteriorate the products' mechanical and fatigue properties [16-18]. Residual stresses induced distortions, cracks and delamination becomes one of the crucial aspects to obtain the manufactured product with higher quality. These defects reduce the part dimensional accuracy and significantly affect the final mechanical performance of the end-use parts, leading to early fatigue failure [19-25]. As residual stresses originate from thermal gradients, ways to relieve them includes decreasing the thermal gradient by using a high temperature stress relief heat treatment [26-29] and chosen of propriate scan strategy [30].

Sequentially coupled thermo-mechanical model can be developed to analyze the effects of process parameters on the temperature history and stress field. The input data for simulating the laser melting process, include selection of manufacture parameters, such as laser power, scanning speed, layer thickness, hatch spacing, part geometry, scanning pattern, etc., controlled by the user subroutine. The output results of FEA approach includes temperature distribution, melt-pool sizes, thermal stress and distortion distribution. From this model, we can analyze the effects of process parameters on temperature and stress distributions during the additive manufacturing process. For example, by analyzing temperature distributions and melt pool configuration, over and insufficient melting can be avoided by choosing appropriate process parameters. By analyzing stress distributions and thermal distortion, defects (such as delamination, cracks, induced by residual stress) can be avoided by choosing appropriate process parameters. These defects reduce the part dimensional accuracy and significantly affect

the final mechanical performance of the end-use parts, leading to early fatigue failure. Experimental validation can provide confidence to the constructed processing approach. This approach is based on FEA simulation; it helps control microstructure morphology, residual stress and deformation in AM parts by optimize process parameters to obtain high final mechanical performance. Several sets of experiments are designed to reveal the processing parameters on properties of deposited components in the method of LMD process. The microstructure, Vickers hardness, phase identification, tensile properties of LMD parts are measured to investigate the fabricated qualities.

1.2. RESEARCH OBJECTIVES

The objective of this research work is to advance the knowledge of how to increase the fabrication properties made by LMD process, using combined approach involving experiments and thermo-mechanical FEA models. Thermal and stress history during LMD process are mainly analyzed. To achieve this goal, three research tasks are listed as follow:

To analyze the effect of temperature profile, cooling rate and temperature gradient on microstructure and resulting mechanical properties of build parts. 3D FEA models with different assumptions on the laser heat source and loading are established and validated with experimental temperature results from thermocouple data. The evolution of thermal history, residual stresses and deformations for a complex geometry are studied. Test coupon is designed and fabricated according to the optimized process parameters, and the microstructure and mechanical properties show certain correlation with cooling rate. This finding can shed light on large scale LMD process in industry.

Copper will be fabricated on AISI 304 stainless steel substrate by laser metal deposition. Crack has been found during the direct deposit interface, so a novel intermediate layer will be proposed to bridge the gap between the composition differences. With the intermediate layer, the phase structure and elemental composition change will be examined by Scanning Electron Microscope (SEM) and energy dispersive X-ray spectroscopy (EDS). For a good metallurgical bonding in LMD fabrications, including pores free and crack free bonding, material chosen with solid solution is necessary. From the residual stress standpoint from FEA model, mismatch of thermal expansion coefficient results in cracking at the bi-material interface. This can be solved by introducing buffer layers in terms of thermal expansion coefficient. This topic helps with the optimization of design and material chosen of LMD process.

To study the feasibility of repairing a complex geometry by laser metal deposition (LMD), laser additive manufacturing process containing tool path planning and experiment parameters were generated according to the extracted geometry. Then microstructure analysis, Vickers hardness and tensile testing were carried out to evaluate the repaired part quality of metallurgical bond in the interface. Predicted deformation and stress results from 3D finite element model provide guidance on evaluation of the repaired part quality.

1.3. ORGANIZATION OF DISSERTATION

In this dissertation, there are four major developments been presented and been organized in the way. Paper I focus on thermo-mechanical model and experimental validation to investigate the thermal and mechanical behavior of LMD technology for one

test coupon. The evolution of both temperature and residual stresses are analyzed. Test coupon was designed and fabricated according to the optimized process parameters. The microstructure and mechanical properties were evaluated to provide fundamental knowledge for large scale LMD process in industry. An efficient predicted simulation method was employed to reduce computational time for modeling of complex structure. This simplified strategy provides an efficient way to get a fast prediction the thermomechanical behavior in complex structure fabrication by LMD. Paper II focus on thermo-mechanical model and experimental validation toward two FGMs cases fabricated by DED process to reveal the residual stress and distortion distribution. This model can be used to predict the stress behavior of products fabricated by DED process and to help with the optimization of design and material chosen of FGMs process. Paper III and IV aim to study the feasibility of repairing a complex geometry by laser metal deposition (LMD). Laser additive manufacturing process containing tool path planning and experiment parameters were generated according to the extracted geometry. Then microstructure analysis, Vickers hardness and tensile testing were carried out to evaluate the repaired part quality of metallurgical bond in the interface. Predicted deformation and stress results from 3D finite element model provide guidance on evaluation of the repaired part quality.

PAPER

I. AN EFFICIENT PREDICTING MODELLING FOR SIMULATING PART-SCALE RESIDUAL STRESS IN LASER METAL DEPOSITION PROCESS

Lan Li[1], Lei Yan[1], Chao Zeng[2], Frank Liou[1]

[1]Department of Mechanical and Aerospace Engineering, Missouri University of Science and Technology, Rolla, MO 65409

[2]Department of Civil, Architectural and Environmental Engineering, Missouri University of Science and Technology, Rolla, MO 65409

ABSTRACT

Residual stress and deformation are common issues which prevent dimensional accuracy and lead early fatigue of products by laser metal deposition process. Finite element analysis is an efficient means to estimate the temperature history and thermal stress distribution. However, it is extremely challenging to predict thermal history and stress distribution of a practical large and complex geometry if each laser pulse is taken into account as by conventional laser pulse modeling. Therefore, in this study, an efficient predictive finite element model with assumptions on the laser heat source and loading is established to study the evolution of thermal history, residual stresses and deformations of a test coupon. The efficient predictive model, which is also called as the 2-layer by 2-layer model, simulates two layers at each laser pulse time. This model is compared with conventional laser pulse model in terms of the evolution of thermal history of selected points and residual stresses. Results show that the 2-layer by 2-layer

model considerably reduces the simulation time without much compromising the accuracy of the prediction of deformation and thermal stress. In addition, test coupon is designed and fabricated to capture temperature history and observe microstructure change. It is found that microstructure presents certain correlation with cooling rate. Microstructure and residual stress of the test coupon are evaluated and found to be consistent with the prediction by proposed model. This efficient predictive model can shed light on large scale part fabrication by laser metal deposition process in industry.

1. INTRODUCTION

Laser metal deposition (LMD) process, a typical Additive Manufacturing (AM) technology, is used for advanced free-form fabrication. It creates parts by directly melting materials and depositing them on the workpiece layer by layer. In this process, the metal powder or fiber is melted within the melting pool by laser beam or electron beam and quickly solidifies to the deposited layer. LMD technology shows great advantages over traditional manufacturing on complex structure fabrication, including high building rates, easy material replacement and reduced material waste. These merits make the wide application of this technology in industry, such as new components fabrication and parts repairing manufacturing. However, the localized moving heat source in LMD process is accompanied with rapid heating and cooling cycles which cause large thermal gradient, and it provokes the formation of high residual stresses and deformations during the laser melting process. The residual stress, if exceeding the yield strength of material, will reduce the part dimensional accuracy and significantly affect mechanical performance of

the end-use products. Residual stress and deformation are main issues that prevent wide applications of LMD. Therefore, it is important to investigate and quantify the temperature evolution and level of residual stresses during and after the additive manufacturing process for full scale components.

To address these issues, various experimental studies and numerical works are conducted based on the metal deposition during the AM process to study the deformations and residual stresses of the built. Experimental studies, by means of X-ray diffraction or neutron diffraction, have been conducted to understand the mechanism responsible for residual stress and deformation [1-3]. In comparison to experimental work, numerical analyses have advantage of monitoring the material stress evolution and optimizing structure design. Finite element (FE) analysis is generally identified as the preferred numerical method due to its ability to handle nonlinear problems, such as, prediction of the thermal history [4-6] and mechanical response including deformation and residual stress [7-11] during the metal deposition process [12-13]. For example, Li et al. [14] developed a 3D thermo-mechanical FE model to study the laser melting process of multi-material structures and validated their model by comparing the temperature history and residual stress with X-ray diffraction measurements. They found that evolution of residual stresses depended on the temperature history and coefficient of thermal expansion of the material component. Heigel et al. [15] developed a thermo-mechanical FE model to study plastic deformation and residual stress under different cooling conditions caused by shielding gas flowing during the deposition. Their results showed that cooling condition largely influenced temperature evolution and deflection as well as residual stress. Lu et al. [16] proposed a 3D thermo-mechanical FE model to take

sensitivity study of process parameters including laser power, scanning speed and powder mass flow rate on both distortion and residual stress induced by LMD. They draw the conclusion that laser power and laser moving speed are much more significant than later one on mitigation of both distortion and residual stress. Ali et al. [17] used 3D transient fully coupled thermomechanical FE model to study the effect of manufacturing temperature on residual stresses in AM to analyze the cylindrical heat source model. Zhang et al. [18] used thermomechanical FE models to study the scaling effects to simulate the residual stresses and residual distortions in the directed energy deposition additive manufacturing. Results indicated that components' sizes affect the final residual states in combination with different design parameters.

The aforementioned FE models have been developed at the microscale or mesoscale, which means simulating single laser pulse moving at each time step on few tracks or few layers simulation domain. Although simulating single laser pulse at each time step works well for simple structures as in above literature, it has limitation to apply on complex and large parts, because part-scale distortion and residual stress prediction for complex and large parts requires thousands of or millions of time steps. With very small laser spot size and small step time, simulation requires large number of finite elements and high computational cost. For complex 3D structures, this simulation scheme certainly becomes computationally time-consuming and intractable. Therefore, the main challenge for simulation of complex and large parts is high computational cost. So far, computational works on how to efficiently calculate thermal history, residual stresses and distortion of complex components for LMD process is scare due to the challenge mentioned above. In the case of powder-bed technologies, such as the Selective Laser

Melting (SLM), the volume-heat-source method [19-24] and flashing heating method [25] drastically reduces computational time for thermomechanical analysis in AM process. That is, a uniform body heat flux is applied to the entire volume in a specified span of time rather than simulating single laser pulse at each time. As one example, the uniform heat source can be applied layer by layer, rather than in localized pattern. Li et al. [20] employed this layer-by-layer heat source method to effectively predict residual stress and part distortion of two twin cantilevers with different support structures fabricated by SLM process. This method reduced the simulation time without much compromising the accuracy of the prediction of deformation and thermal stresses in the AM process. This layer-heat-source method in SLM process gives us the idea of simulating more layers in one laser pulse in LMD process to speed up the simulation. By virtue of this efficient computational method, thermal-mechanical numerical analysis of LMD process for complex geometry becomes amenable and computationally feasible. Therefore, the objective of this study is to propose an efficient predictive model for complex geometry simulation in the LMD process. The efficiency of this new model will be demonstrated by comparing with conventional laser pulse method in terms of thermal history, residual stress and deformation prediction.

Herein, in this study, 3D coupled thermo-mechanical FE analyses are conducted to predict the thermal and stress behavior of a Ti6Al4V part fabricated by LMD technology. Two separate models are developed. The one is conventional laser pulse model that simulates LMD process by single laser pulse at each time in terms of residual stress and deformation. The other is proposed rapid 2-layer by 2-layer model that activates single laser pulse each time at two layers while keeping high accuracy. This

paper is arranged as follows: In Section 2, experiment design and measurement were introduced. In Section 3, numerical model setup and modelling strategies for those two models are elaborated. In Section 4, simulation result is validated with designed experiments in terms of thermal cycles. Then, thermal distribution, residual stress and distortion results are studied and compared. Microstructure and residual stress of the test coupon are evaluated to further validate the proposed model. Finally, Conclusions are given in Section 5.

2. EXPERIMENTAL DESIGN AND MODEL SETUP

To investigate thermal history and mechanical properties of the large-scale LMD process, an experiment was first performed to define the coupon geometry for large scale fabrication. The coupon geometry and substrate geometry are shown in Figure 1(a) and 1(b) which includes thin wall structures of different geometric features. The coupon was fabricated by a DMG MORI 4300 manufacturing system with 1800 W laser power, 4 mm laser beam spot size, 29.7 g/min powder feed rate, and 240 mm/min travel speed. The LMD parameters are shown in Table 1. This coupon has ten layers in total and total height of 12.5 mm. Four thermocouples (TC0, TC1, TC2, and TC3) were attached on the substrate with thermally conductive paste and temperature was recorded with a data acquisition instrument. The dimension of the substrate and the locations of thermocouples are shown in Figure 1(d). The deposit is fabricated according to the path plan and the scanning sequence follows 1→3→2 in Figure 1(d). Figure 1(c) is an image of the substrate used in the experiment with four thermocouples before deposition, while the

final as-fabricated part is shown in Figure 1(e). Schematic diagram of the designed LMD is shown in Figure 1(f).

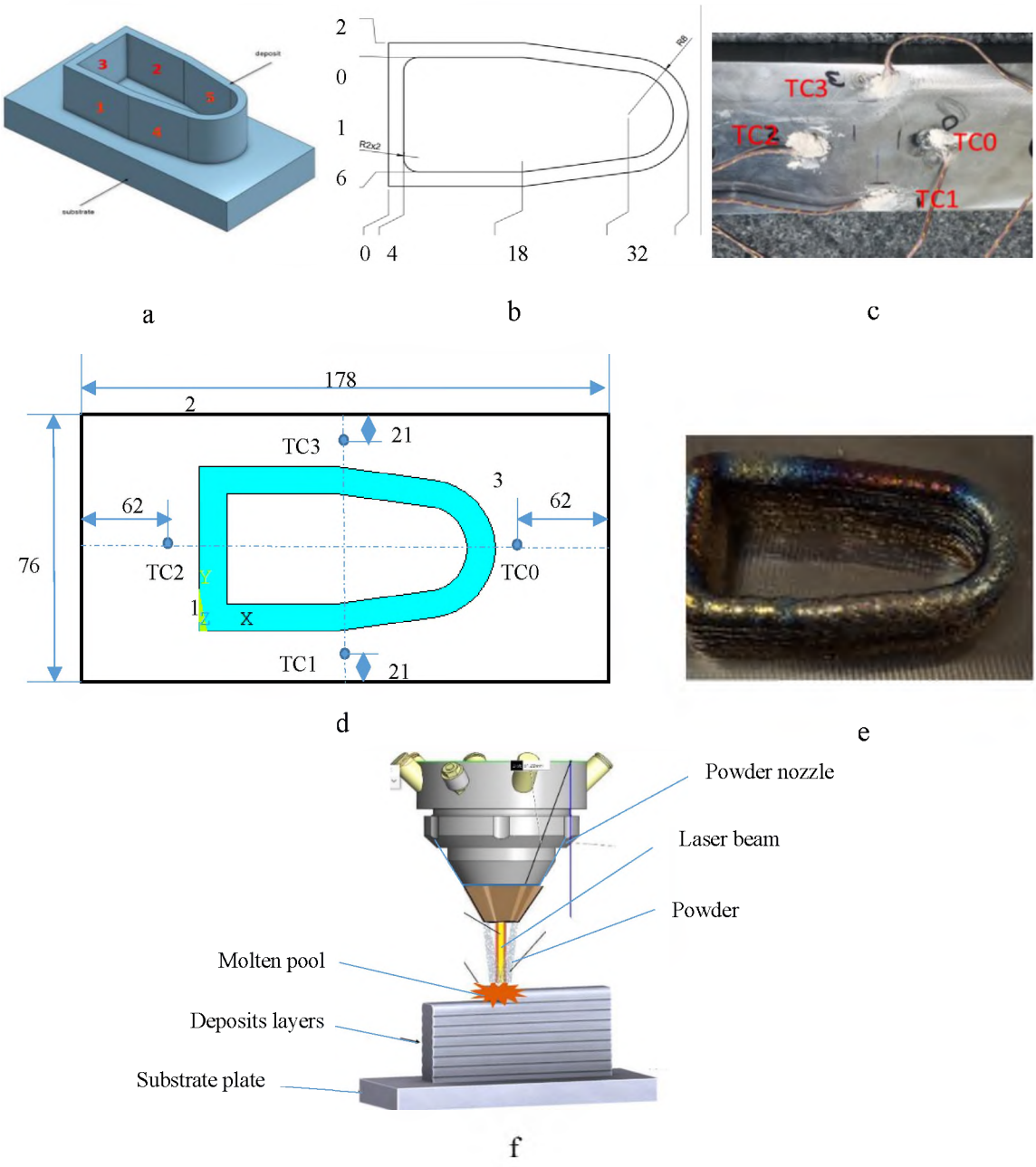

Figure 1. Images of the coupon: (a) Coupon geometry design; (b) 3D geometry with dimension details; (c) Thermocouples on the substrate before deposition; (d) Schematic diagram of the substrate and location of thermocouples for coupon validation; (e) As-built coupon; (f) Schematic diagram of the designed LMD.

Table 1. LMD parameters for coupon fabrication.

Parameter	Value
Laser power	1800 W
Laser beam size	4 mm
Laser scan speed	4 mm/s
Powder feed rate	32 g/min
Total layer thickness	12.5 mm
Total layer number	10

3. LMD MODELING

3.1. MODEL SETUP

Ansys® Mechanical APDL was employed to set up a 3D coupled thermo-mechanical model in which the temperature history and residual stress during LMD process can be instantly monitored. In the model, the transient heat transfer analysis was firstly performed to obtain temperature distribution. Then, the structural analysis was implemented to calculate thermal stress and distortion. Figure 2(a) presents the FE meshes of deposited geometry. Hexahedral element with 8 nodes is used for deposit material and tetrahedral element with 4 nodes is used for substrate material. Z-axis direction specifies building up orientation in the cartesian coordinate system. In material deposition process, the continuously adding elements is implemented by birth-and-death function in Ansys® to activate an element. This element activation method is widely used in modeling material deposition in AM process. Eight hexahedral elements were used to

build coupon width and two hexahedral elements were used along Z-axis direction to build each layer thickness at each time step. At initial state, just the substrate elements were all activated. New adding elements were activated sequentially to simulate material addition process, as shown in Figure 2(b). The deposition coupon consists of 176,405 elements and 358,681 nodes.

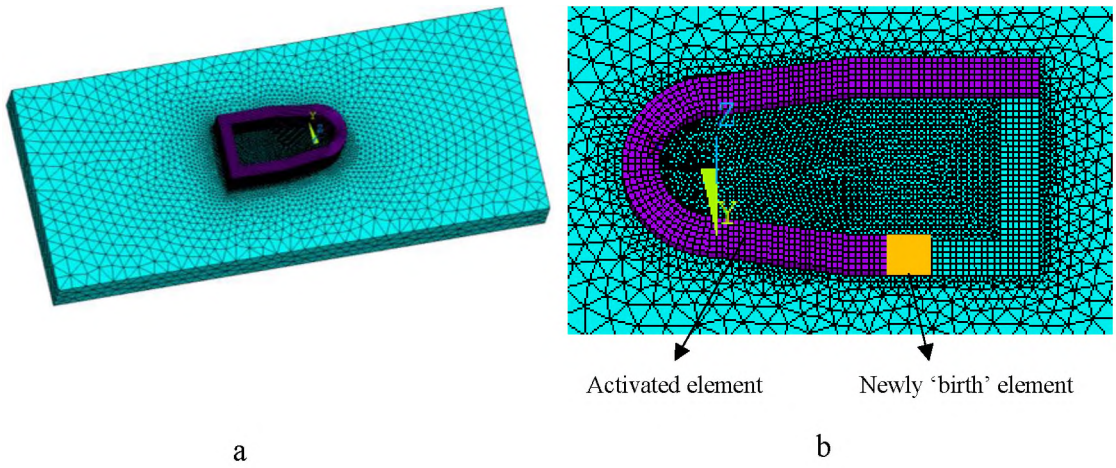

Figure 2. (a) Overall mesh configuration of FEM model and (b) enlarged mesh configuration on deposit coupon.

3.2. GOVERNING EQUATION FOR THERMO-MECHANICAL ANALYSIS

Transient heat conduction equation is used as the governing equation for heat transfer in the entire volume of the material, given as

$$\rho c_p(T)\frac{\partial T}{\partial t} = \frac{\partial}{\partial x}\left[k(T)\frac{\partial T}{\partial x}\right] + \frac{\partial}{\partial y}\left[k(T)\frac{\partial T}{\partial y}\right] + \frac{\partial}{\partial z}\left[k(T)\frac{\partial T}{\partial z}\right] + \dot{q} \quad (1)$$

where T is the current temperature, $k(T)$ is the temperature-dependent thermal conductivity, $c_p(T)$ is the temperature-dependent specific heat, ρ is the constant density, $\dot{q}$

represents heat sink or source in the volume, t is the time, x, y and z are the coordinates in the reference system as the same as X, Y, Z in graphs.

Stress equilibrium equation is used as the governing equation for mechanical analysis [26-27]:

$$\nabla \cdot \sigma = 0 \tag{2}$$

where σ is the second-order stress tensor associated with the material behavior law.

The isotropic Hooke's law is used to relate stress and elastic strain as

$$\sigma = C\varepsilon^{e} \tag{3}$$

where ε^{e} is the second-order elastic strain tensor and C is the fourth-order material stiffness tensor.

Thermo-elasto-plasticity is considered in the deposition process. Therefore, the total strain ε has three components [28]:

$$\varepsilon = \varepsilon^{th} + \varepsilon^{p} + \varepsilon^{e} \tag{4}$$

$$\varepsilon^{th} = \alpha \cdot \triangle T \tag{5}$$

where ε^{th}, ε^{p} and ε^{e} are the thermal strain, plastic strain, and elastic strain, respectively, α is the coefficient of thermal expansion and ΔT is the temperature difference with respect to reference temperature. The thermal strain is calculated by equation (5). Elastic and plastic stain in our study is calculated by bilinear isotropic hardening model which is defined by elastic modulus E, Poisson's ratio v, yield strength σ_Y, and tangent modulus G [29-30].

In experiments, the laser beam heats up the layered material in circular influencing region. In the simulation, this heating process is represented as volume heat flux on active element of powder. Because of the small size in powder depth direction,

the power density in depth direction was considered constant. The heat flux obeys Gaussian distribution on the *x*-*y* plane which follows as:

$$\dot{q} = \frac{2\phi P}{\pi r_0^2} \exp\left[-2\frac{r^2}{r_0^2}\right] \tag{6}$$

where ϕ is the laser absorptivity, $\phi = 0.3$ in this work. r_0 is the radius of laser beam and P is the laser power, Eq. (6) shows that heat flux exponentially decays away from the laser beam center in *x*-*y* plane.

3.3. BOUNDARY CONDITIONS

Before the laser heating, atmospheric temperature works as the initial temperature condition. The substrate follows the uniform temperature distribution:

$$T(x, y, z, t)_{t=0} = T_0 = T_a \tag{7}$$

where T_a is the ambient temperature equals to the initial temperature T_0, set as 25 ℃.

All external surfaces of deposited layer are exposed to atmosphere and are subjected to heat convection with air and heat radiation. These two factors dissipate thermal energy into atmosphere and are necessarily considered in this study. The corresponding boundary conditions for external surfaces are:

$$q_c = h\left(T - T_a\right) \tag{8}$$

$$q_r = \varepsilon_r \sigma_r \left(T^4 - T_a^4\right) \tag{9}$$

where h is the heat transfer coefficient of natural thermal convection, which is assumed to depend on temperature and is presented in Table 2, σ_r is the Stefan–Boltzmann constant setting as 5.67×10^{-8} W/m^2·K^4 and ε_r is the material emissivity setting as 0.3. Base plate underneath the substrate can absorb heat rapidly in the laser deposition process and

maintain at ambient temperature. Therefore, in the simulation, flux boundary is set for the substrate base surface as Eq. (8). By fitting simulated and experimental results, the heat transfer coefficient used for Newton's model is set to 100 [W/m^2·°C]. In the structural analysis, the substrate base surface is set to fixed boundary condition.

Table 2. The convection heat transfer coefficient used in the simulation.

Temperature (°C)	25	200	400	600	800	1000	1500	2000
h, (W/(m^2·°C)	6	12	20	36	40	50	80	80

3.4. THERMO-PHYSICAL AND MECHANICAL PROPERTIES

The laser-induced high temperature can melt the deposit material Ti6A14V. The Ti6A14V undergoes phase change in the LMD process. To reduce computational complexity, the liquid phase is also described by the same model with compensated properties. For example, the effective thermal conductivity is significantly enhanced as temperature above the melting temperature because liquid flow can also convert heat besides conduction. The elastic modulus is significantly reduced since liquid has much higher compressibility. The detailed thermo-physical and mechanical properties of Ti6Al4V is shown in Table 3, used from paper [31].

3.5. SIMULATION STRATEGY

Layer-based approach [32-33] was used to drastically reduce computational time in Selective Laser Melting (SLM). Compared to conventional single laser pulse

Table 3. Thermo-mechanical properties of the Ti6Al4V.

Temperature (°C)	Density (kg/m3)	Thermal conductivity (W/(m·K))	Specific heat (J/(kg·K))	Poisson's ratio	Thermal expansion coefficient (10^{-6}/K)	Elastic modulus (GPa)	Yield strength (MPa)
25	420	7.2	545	0.35	8.5	112	950
200	395	8.7	580	0.35	10	110	650
500	350	12.5	650	0.37	11	80	480
1000	282	22	750	0.42	12	20	20
1100	267	19.5	640	0.42	12.2	5	10
1200	250	21.2	661	0.42	12.2	4	1
1600	190	26	730	0.42	12.2	1	0.6
1650	885	84	830	0.42	12.2	0.1	0.1
2000	810	84	830	0.42	12.5	0.01	0.01

simulation method, these strategies activate one layer or entire volume in layer-by-layer sequence. Specifically, a uniform body heat flux is applied to an entire layer for a representative span of time. This volume-heat-source method in SLM process gives ideas to reduce the simulation time by simulating larger zone in one laser pulse in LMD process.

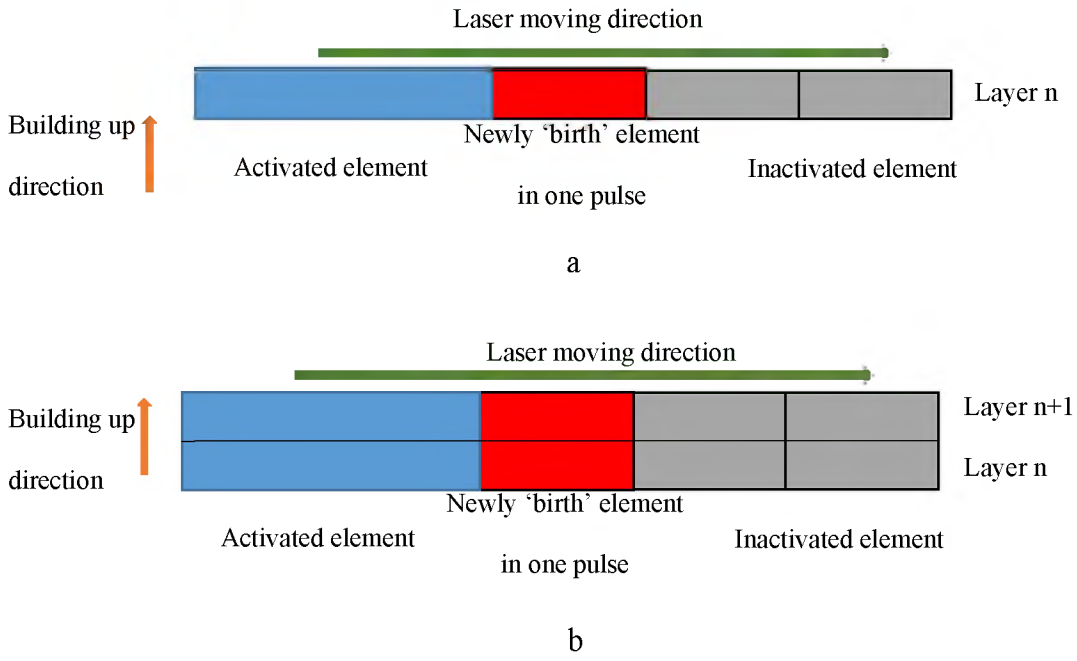

Figure 3. (a) Conventional single laser pulse method; (b) 2-layer by 2-layer based heat input method.

Therefore, a 2-layer-by-2-layer activation strategy has been selected to further reduce simulation time while maintaining the overall accuracy of the simulation. Hence, in each time step, all elements in 2 consecutive layers in thickness (along Z direction) are activated with half of original scanning rate, shown in Figure 3(b). In order to verify and

compare this, a conventional laser pulse model was conducted (as shown in Figure 3(a)). The laser scanning rate of the laser pulse simulation is 4 mm/s, thus an equivalent scanning rate of 2 mm/s is adopted in 2-layer-by-2-layer simulation.

4. RESULTS AND DISCUSSION

4.1. VALIDATION OF TEMPERATURE EVOLUTION

The FE model is firstly validated with temperature measurement in four thermocouples. As a first step, the numerical model employed conventional single laser pulse simulation method which applies the heat source spot by spot. The efficient method will be discussed in later section. Figures 4 show the comparison between the measured temperature at four thermocouples (TC0, TC1, TC2, and TC3) and the simulation result. For each graph, the solid red line and black dot indicate the simulation result and experimental results, respectively. The overall agreement can be observed except some discrepancies. The mismatch is probably due to the approximate material properties used in simulation. Each thermocouple experiences ten temperature peaks due to cyclic heating pulse in each layer deposition. When heating pulse approaches nearest to the thermocouples in each layer deposition, temperature sharply increases. The temperature peak becomes higher at successive layers. This trend is attributed to the high heating injection by laser but relatively slow thermal dissipation at the substrate. The thermal energy accumulates in short time and increases the temperature in successive layers. This statement can be confirmed by the temperature evolution at different times during 10 layers deposition of Ti6Al4V, shown in Figures 5. The highest temperature is located at

the laser pulse center and the temperature becomes smaller away from the laser pulse. There is a heat affected zone where the temperature is relatively high than remote zone. This heat affected zone moves with the laser pulse. When this heat affected zone is closest to the neighboring thermocouples, measured temperature experiences a peak. Absorbed thermal energy increases substrate temperature gradually.

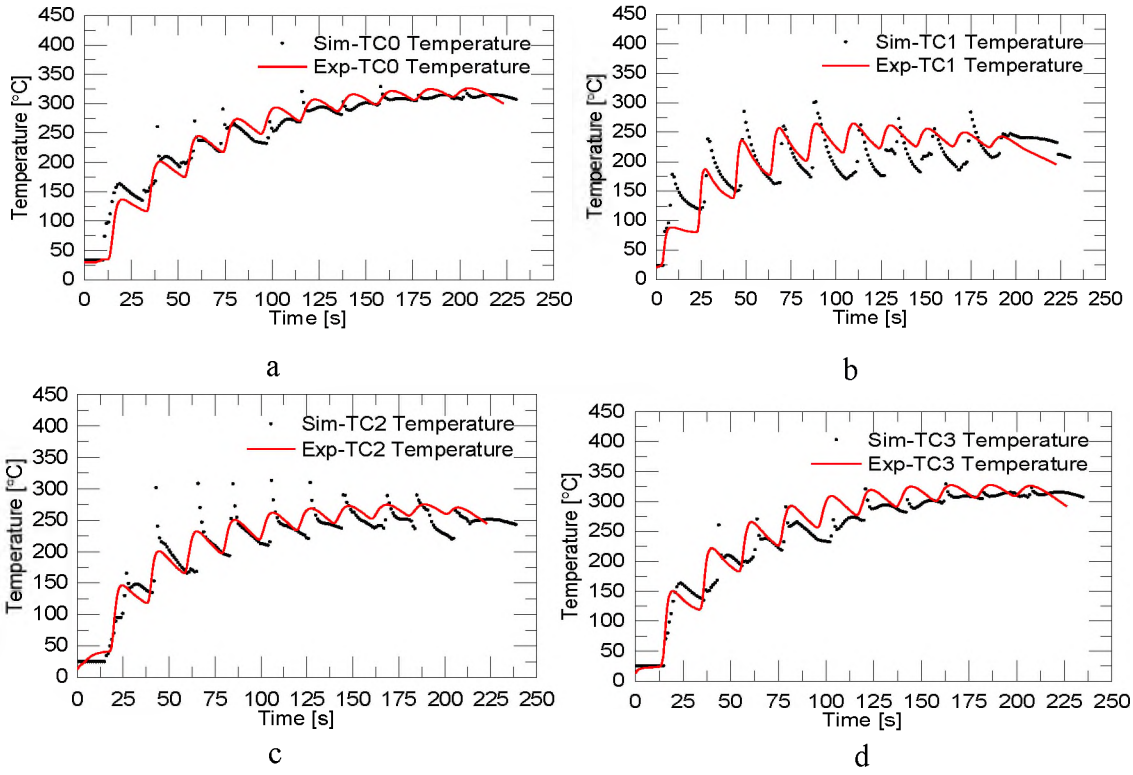

Figure 4. Temperature evolution from numerical and experimental results at four thermocouples: (a) TC0; (b) TC1; (c) TC2; (d) TC3.

Figure 6(a) shows the temperature evolution in 1st to 10th layers at the center of the left straight wall. The sharp temperature peaks indicate that during the depositing process, heating is very fast. Each monitoring location experiences several temperature peaks due to heating from subsequent deposited layers. At one monitoring location, the

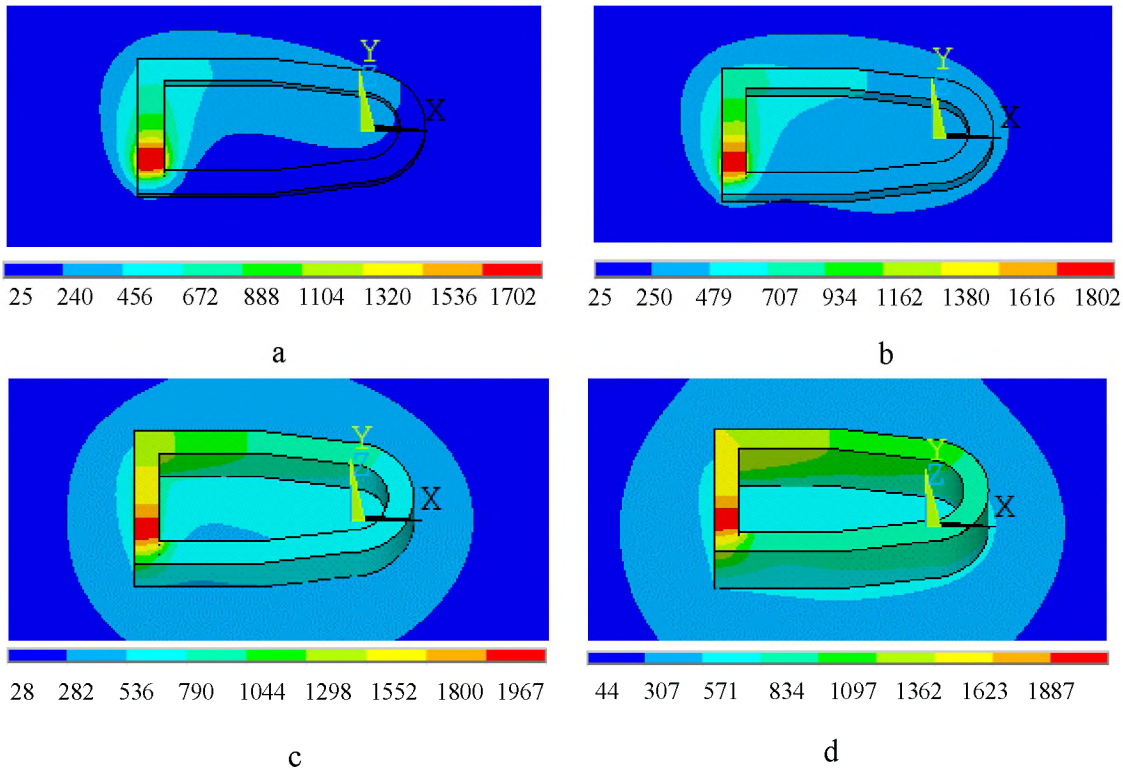

Figure 5. Temperature distribution during the deposition of (a) 1st; (b) 2nd; (c) 6th and (d)10th layer deposition.

first temperature peak is highest since laser scans at that position and following temperature peaks become smaller due to increasing distance to the laser pulse locus. For example, there are ten temperature peaks in 1st layer, just first and secondary peak temperature are higher than the melting point of Ti6Al4V (i.e., 1650 ℃), third to tenth peak temperature are lower than the melting temperature. This means, the first layer is affected by ten thermal cycles, but can only be re-melted by the second track. For the only temperature peak of last layer deposition, highest temperature peak of 2250 ℃ was obtained. In addition, the temperature contours present elongated shape behind the heating beam and compressed shape ahead of heating beam, which is caused by the rapid scanning motion of laser beam. The highly transient and spatially non-uniform

temperature distribution, shown in Figures 5 and Figure 6(a), are responsible for the generation of the stress and strain fields. Figure 6(b) represents the cooling rate of four distinct locations (1st, 2nd, 6th, and 10th layer) and shows that the maximum cooling rate for each monitoring point occurs exactly as laser scans on that layer. As deposited layers increase, the maximum cooling rate for each individual layer gradually reduces due to the increased temperature of previous layers and the substrate. The temperature gradient (especially Z direction component) between two consecutive monitoring points maximizes at 1st ~ 2nd layer and gradually reduces with more layer deposited. This decreasing trend of maximum temperature gradient is consistent with the finding from paper [7,34]. The maximum temperature gradient near 1st layer is more likely to cause substantial thermal stress near the substrate, rather than the free top end of deposit.

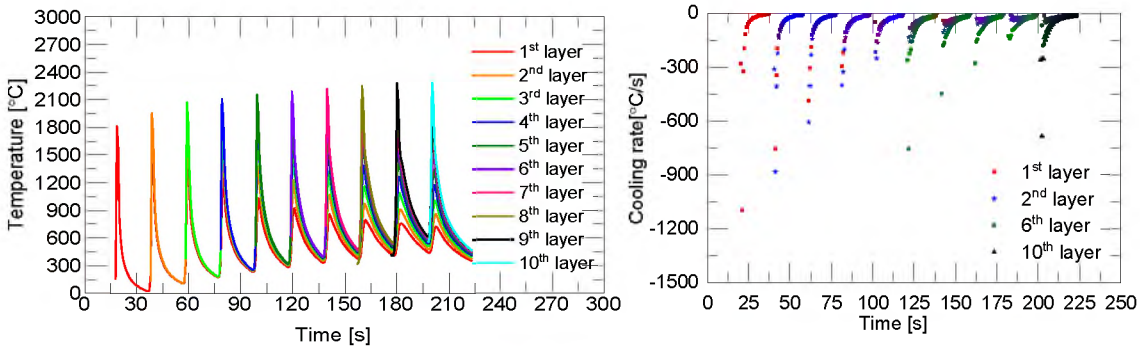

a b

Figure 6. (a) Temperature history of monitored points at the center of the cross-section at the 1st to 10th layers at plane of y=0; (b) Cooling rate values with thermal cycles at different locations.

The cooling rate for each individual layer gradually reduces as deposited layers increase, which is attributable to microstructure growth of the formed parts and can further validate the thermal history. To identify the size of microstructure in the

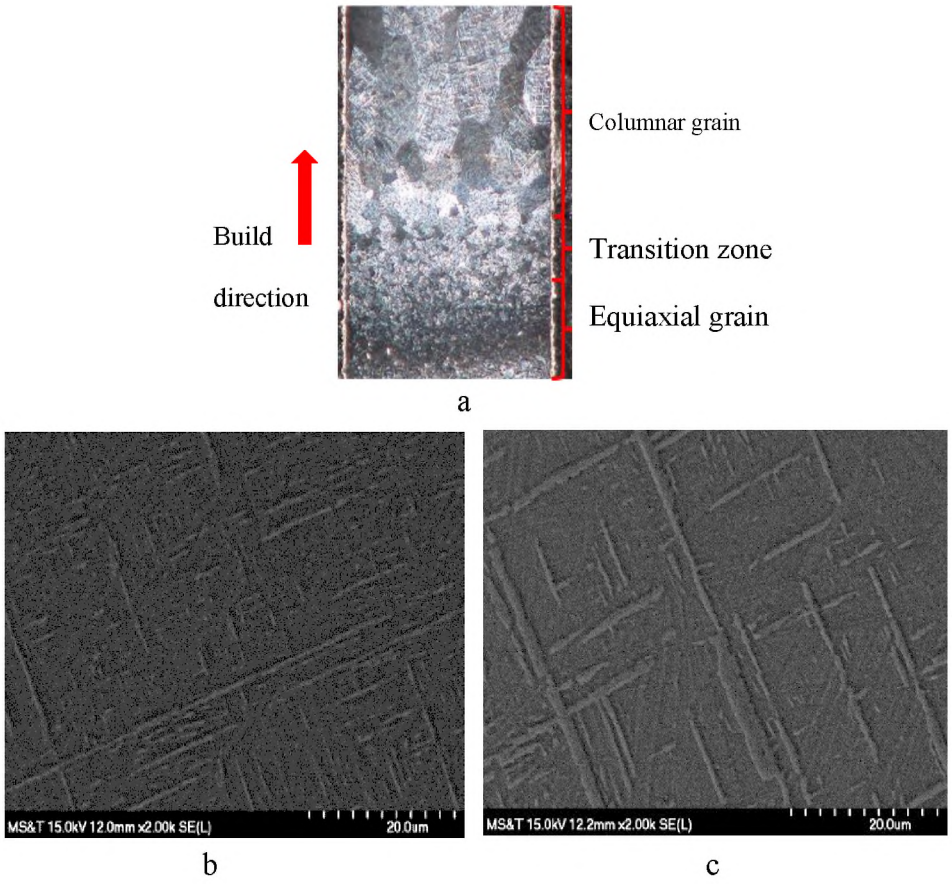

Figure 7. (a) The microstructure of the single wall structure with different zones; (b) SEM image of α-lath at the 1st layer; (c) SEM image of α-lath at the 10th layer.

deposition height, optical microscopy and scanning electron microscopy (SEM) were applied. Figure 7(a), a low magnification representation, shows that the microstructure changes from fine equiaxed grains at the substrate to coarse columnar grains at the deposited zone along Z direction. The middle region is a transition zone where microstructure has smooth change. Figure 7(b) and 7(c) show the higher magnification microstructure at bottom of the deposition (the 1st layer) and top of the deposition (the 10th layer). Needle-like α-lath structure with 90° angle can be clearly seen in both images. The mean α-lath width appears much thicker (1~2 um) at the top layer than that at the

bottom layer (0.5 um). It implies the higher cooling rate at bottom layer than at top layer since cooling rate directly relates to α-lath width. This is consistent with numerical result in Figure 6(b) that 1st layer has maximum cooling rate in deposition. The cooling rate decreases and causes coarser microstructure along Z direction which is consistent with the results in paper [39]. The variation of microstructure size further validates accurate prediction of thermal history by the FE model.

4.2. DISPLACEMENT AND RESIDUAL STRESS FROM CONVENTIONAL METHOD

Figures 8 show the longitudinal stress and displacement distribution in x-direction after deposition of 1st, 2nd, 6th, 10th layers and cooling to room temperature. The initial temperature of the entire model was 25°C. In the deposition of 1st layer, the deposit is heated to high temperature and the temperature difference between deposit and substrate is high. The larger thermal expansion of deposit than substrate induces large compressive stress near the substrate-deposit interface, shown in Figure. 8(a). It also leads to bending and plastic deformation. This can be observed by the displacement in x-direction at the upper deposition region of the building part, with values of 0.019 mm in Figure 8(b). With more deposited layers, the substrate temperature gradually increases, and hence the maximum thermal gradient gradually reduces until after the deposition of the 10th layer. The back and-forth laser traveling and longitudinal displacement (Ux) at different process times in (b), (d), (f), (h), (j). strategies impose cyclic thermal heating and resulted in cyclic thermal stress. At the end of the deposition process (10th layer in Figure 8(g)), tensile stress accumulates near the top free end and large compressive stress builds up

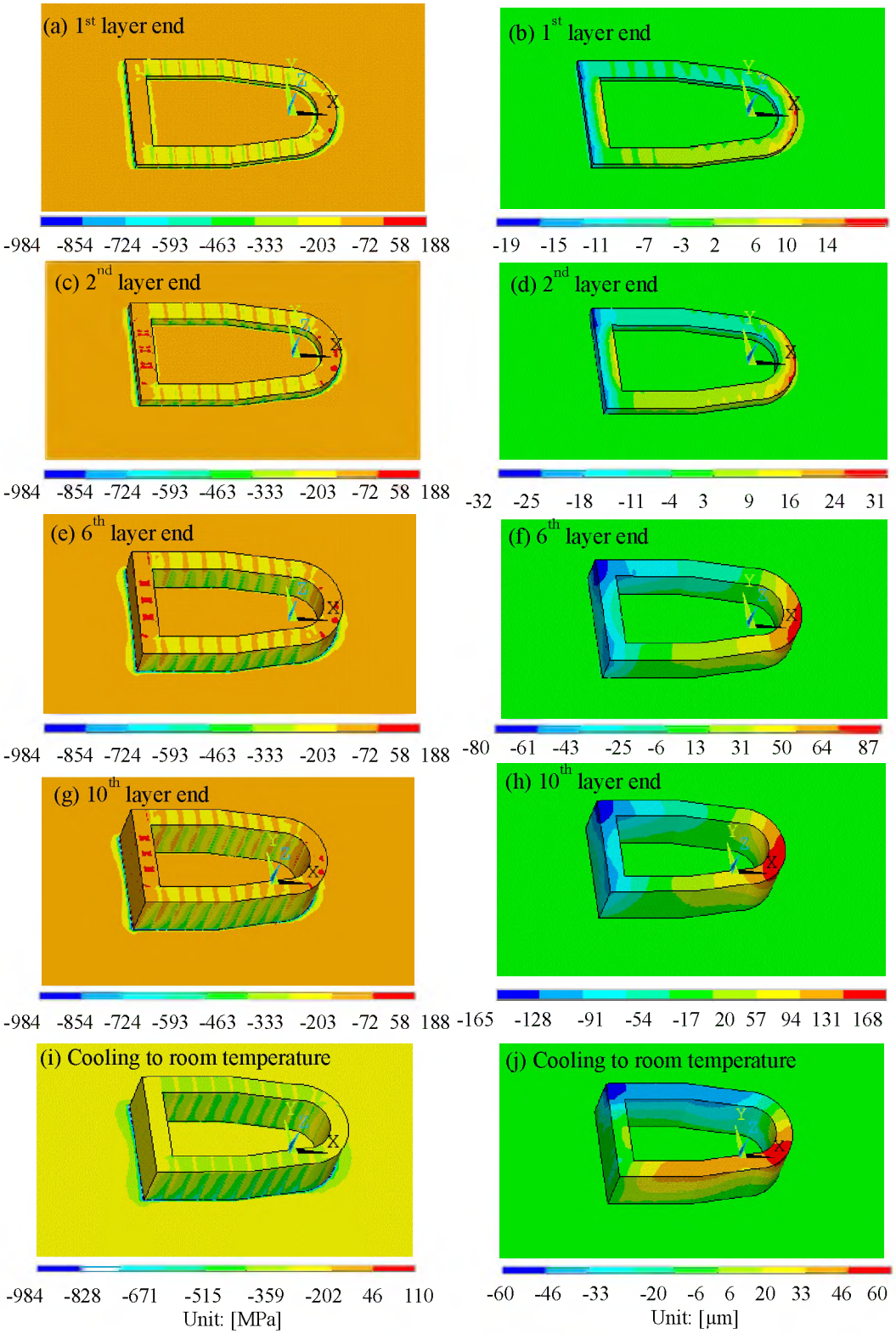

Figure 8. The evolution of the longitudinal stress (σ_{XX}) at different process times in (a), (c), (e), (g), (i).

near the substrate-deposit interface. During the period when the 2nd to 10th layers is deposited, the displacement gradually increases due to the cooling and shrinking of these deposited layers. The displacement increases from 0.019 mm, to 2nd layer of 0.031 mm in Figure 8(d), to 10th layer of 0.168 mm in Fig 8(h). After deposition heating and subsequent solidification of all layers, the structure cooled down to the ambient temperature. Due to the cooling and shrinking of these deposited layers, compressive stress quickly transitions into tensile stress. Hence, tensile stress increases to 400 MPa in Figure 8(i). During this cooling process, displacement gradually reduces and stabilizes to the end at the value of 0.06 mm in Figure 8(j).

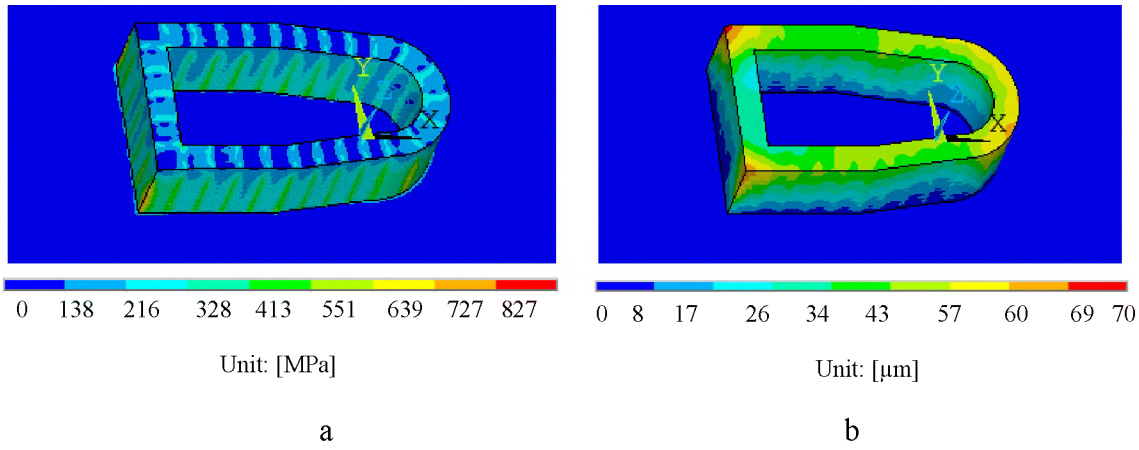

Figure 9. Predicted results of residual von Mises stresses, Seqv and total displacement, Us under conventional pulse method.

When the coupon cools down to the room temperature, the von Mises residual stress and total displacement are shown in Figures 9. It can be seen that the largest stress occurs at the interface between the substate and the deposition. Especially at the corners of the walls, the largest residual stress with the value of 845 MPa was observed due to the

high thermal gradient at these points. The residual stress gradually reduces along building up direction. This trend is similar to the predicted results reported in [35-38]. Free boundary of top end releases thermal stress by excessive displacement. The total displacement of 0.077 mm can be observed at the top corners of the walls in Figure 9(b).

4.3. TEMPERATURE, DISPLACEMENT AND RESIDUAL STRESS OF THE EFFICIENT MODELLING AND COMPARISON

Figures 10 show the comparison of temperature evolution at four monitoring locations (same locations as thermocouples TC0, TC1, TC2, and TC3 in experiments) by two simulation methods: conventional single laser pulse method and 2-layer by 2-layer method. For each graph, the black line and red line indicate the simulation results of the laser pulse simulation method and 2-layer by 2-layer method, respectively. In LMD process, the laser beam moves according to the path plan and the cyclic scanning sequence causes cyclic temperature change at each monitoring location. It shows ten temperature peaks for conventional method and five temperature peaks for simplified method. The conventional method shows temperature evolution with higher resolution in each individual deposited layer. Except that, the overall trend of temperature evolution, i.e., increasing temperature peaks and temperature difference between two consecutive cycles, are maintained for both simulation methods.

Figures 11 show the longitudinal stress and displacement distribution in x-direction at process times of all deposition done and cools to room temperature in 2-layer by 2-layer method. At the end of the deposition process in Figures 11(a), tensile stress accumulates near the top free end and large compressive stress builds up near the

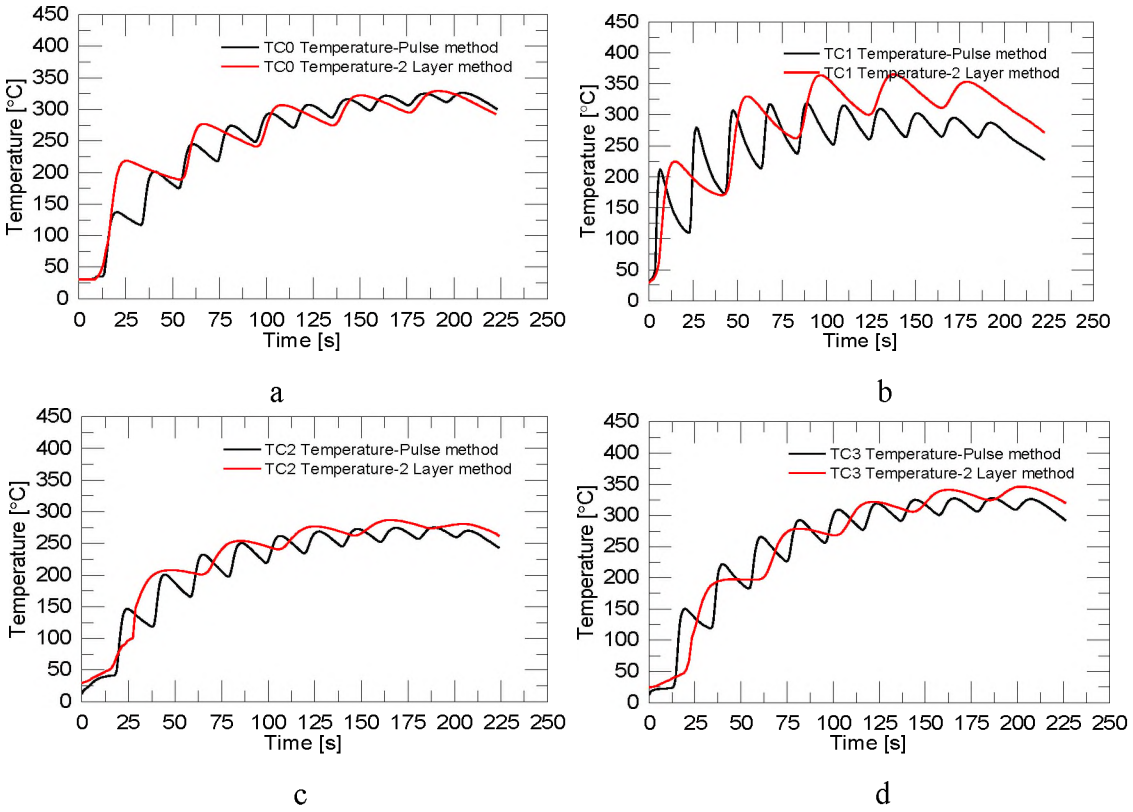

Figure 10. Temperature validation result for the designed coupon fabrication with conventional simulation method and with 2-layer-based heat source method for four thermocouples: (a) TC0; (b) TC1; (c) TC2; (d) TC3.

substrate-deposit interface, reach the values of 188 MPa and 984 MPa, respectively. This trend is similar to the predicted results by conventional method reported in Figures 8 and have the same magnitude level. When the coupon cools down to the room temperature, the largest residual stress with the value of 473 MPa was observed in Figures 11(c), which is a little bit higher than that in Figures 8(i) due to the assumption of activating two layers each time. The tensile stress within the top deposited layer is caused by the contraction of the molten material after cooling. For layers underneath the top layer, tensile stress is reduced and gradually changes into compressive stress because of the annealing effect by subsequent deposition layers. The longitudinal displacement profile

(along x direction) in Figures 11(b) and 11(d) consist of large values near the top and two ends of the as-built part, while smaller displacement occurs in the center of the part. Same level of displacement compared with conventional model can be found here. In addition, residual stress field and total displacement field from simplified method is presented in Figure 12, as a comparison to the conventional method in Figure 9. Similarly, even if the difference exists for simplified method, the overall average stiffness of the structure doesn't show much change. The difference is attributed to the different

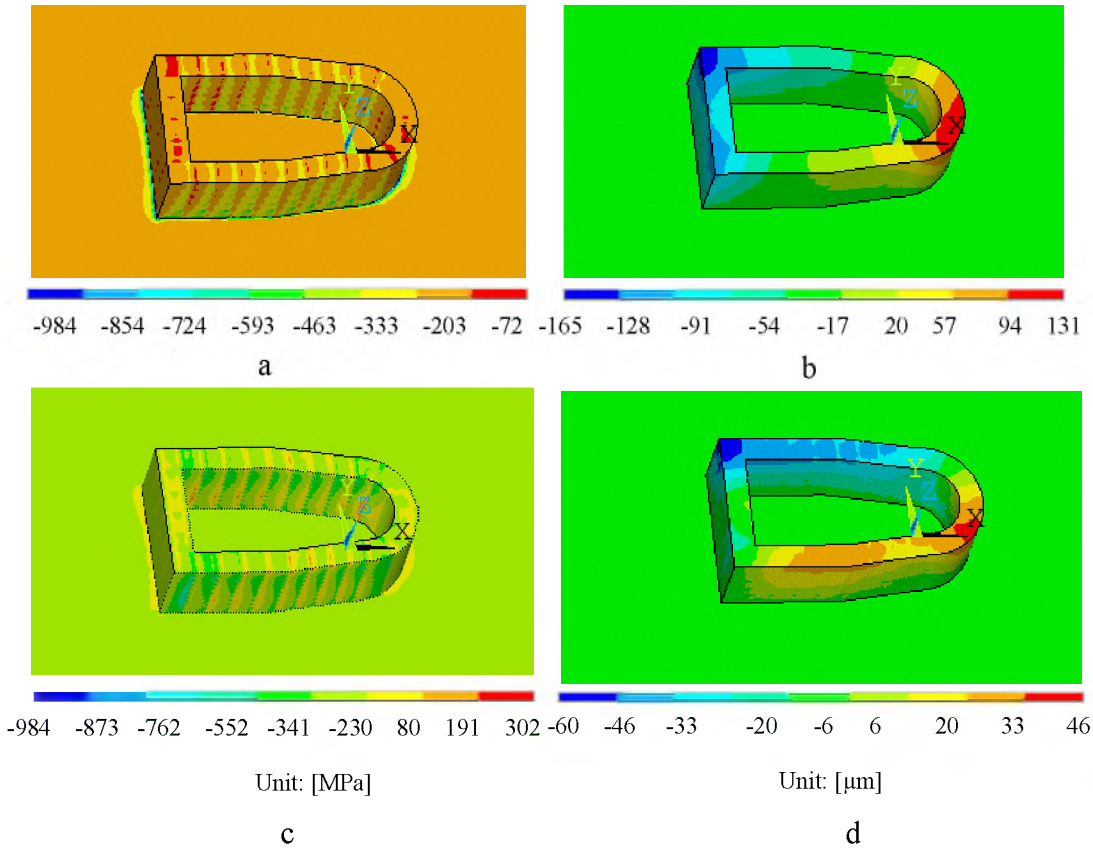

Figure 11. Predicted results of the longitudinal stress (σxx) at different process times in (a), (c) and longitudinal displacement (Ux) at different process times in (b), (d).

local thermal conditions i.e., temperature cycles and temperature gradients. This simplified strategy provides an efficient way to quickly predict thermomechanical behavior of LMD process. In terms of the computational time, the laser pulse simulation method took about 48 hours and the 2-layer by 2-layer method took about 19 hours on a computer with a Xeon Processor 3.4 GHz and 128.0 GB RAM hardware. More than half computational time is saved with some compromising details in coupon fabrication. Therefore, for complex geometry modeling, this work demonstrates a simplified strategy to quickly assess temperature evolution and stress distribution in LMD process. The balance between simulation time and accuracy needs further investigation.

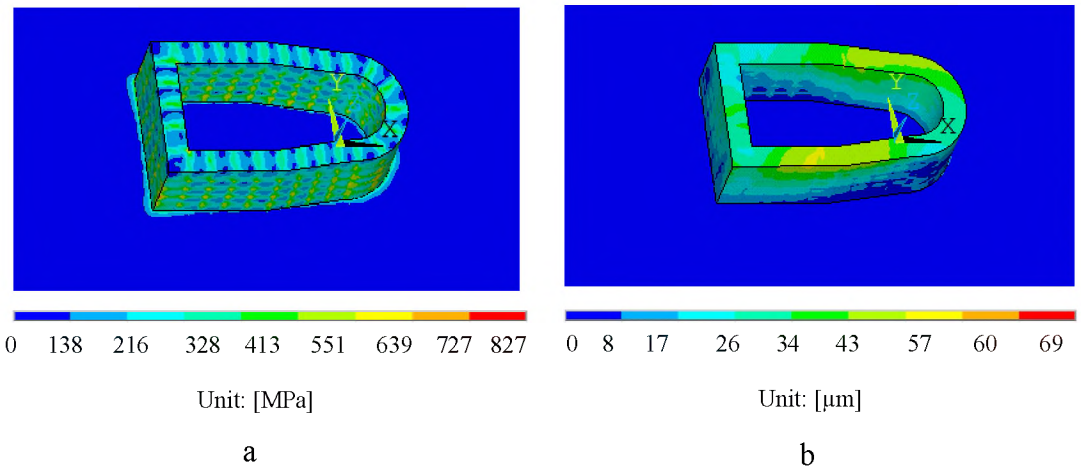

Figure 12. Predicted results of residual von Mises stresses, Seqv and total displacement, Us by 2-layer-by-2-layer method.

4.4. STRESS VALIDATION

The predicted von Mises stresses (σeqv) along the building up direction of the deposition at the cross-section for the two models are shown in Figure 13. In this figure,

it can be seen that at the deposition of the 1st layer, a maximum residual stress of 400 MPa is generated at the interface between the base plate and the metal-deposition. This is due to the large thermal gradient and the rapid cooling and shrinkage of the built. According to the reduction of the thermal gradient during the deposition of the 10 layers, the stresses along the deposition direction reduce significantly. Note that most layers far away from the base plate show smaller residual stress. Numerically predicted von Mises stresses (two solid lines) are compared with experimental measurement (individual spots), as shown in Figure 13. In the FE simulation, the stress curve can be readily extracted. Measured stresses were obtained using XRD with sin2ψ technique. Experimental and calculated curves have a satisfactory agreement, except a little bit mismatch. One error comes from the cutting of the samples which leads to a relaxation of the residual stresses. This would lead to a relaxation of accumulated thermal stress and reduce it compared to an actual part.

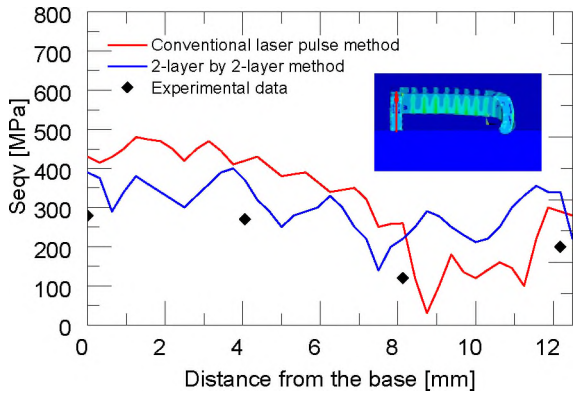

Figure 13. Comparison of experimentally measured and numerically computed von Mises stress.

5. CONCLUSION

This work proposes an efficient predictive model for fast predicting the part scale residual stress and displacement for a complex geometry by LMD process. The efficient predictive model, which is also called as the 2-layer by 2-layer model, with assumptions on the laser heat source and loading which simulating two layers at each laser pulse time. This model is compared with conventional laser pulse model in terms of the evolution of thermal history, residual stresses and computational cost. The accuracy of the model has been determined via experimental measurement in terms of temperature history, microstructure and stress validation. The main conclusions are structured as:

1) The numerical prediction of temperature history was in good agreement with the experimental measurements at four thermocouples. The variation of microstructure size along the building up direction further validates accurate prediction of thermal history by the model with thermal gradient and cooling rate.

2) The residual stress profile simulated by the proposed method correlates well with experimental data.

3) The evolution of residual stress and displacement in 2-layer by 2-layer method was studied and compared with conventional single laser pulse method. Results show that the simplified method reduces the simulation time more than half without much compromising deformation and thermal stress.

This efficient predictive model provides an efficient way to get a fast prediction on thermal and stress behavior in complex structure fabrication by LMD. This simplified strategy made the assumption on laser loading which simulating two layers at each laser

pulse. For future work, the balance between varying part for simulating layers, simulation time and accuracy should be taken into account to improve part-scale prediction accuracy. Since the layers for a large AM part may experience varying thermal history due to difference in layer geometry and heat accumulation by previous layers.

REFERENCE

[1] A.S. Wu, D.W. Brown, M. Kumar, G.F. Gallegos, W.E. King, An experimental investigation into additive manufacturing-induced residual stresses in 316L stainless steel, Metall. Mater. Trans. A 45 (2014) 6260–6270.

[2] L. Sochalski-Kolbus, E.A. Payzant, P.A. Cornwell, T.R. Watkins, S.S. Babu, R.R. Dehoff, M. Lorenz, O. Ovchinnikova, C. Duty, Comparison of residual stresses in Inconel 718 simple parts made by electron beam melting and direct laser metal sintering, Metall. Mater. Trans. A 46 (2015) 1419–1432.

[3] K. An, L. Yuan, L. Dial, I. Spinelli, A.D. Stoica, Y. Gao, Neutron residual stress measurement and numerical modeling in a curved thin-walled structure by laser powder bed fusion additive manufacturing, Mater. Des. 135 (2017) 122–132.

[4] M. Chiumenti, X. Lin, M. Cervera, et al., Numerical simulation and experimental calibration of Additive Manufacturing by blown powder technology. Part I: thermal analysis, Rapid Prototyp. J. 23 (2) (2017) 448–463.

[5] P. Peyre, P. Aubry, R. Fabbro, et al., Analytical and numerical modelling of the direct metal deposition laser process, J. Phys. D 41 (2) (2008).

[6] P.M. Sammons, D.A. Bristow, R.G. Landers, Height dependent laser metal deposition process modeling, J. Manuf. Sci. Eng. 135 (5) (2013) 054501.

[7] X. Lu, X. Lin, M. Chiumenti, et al., Finite element analysis and experimental validation of the thermomechanical behavior in laser solid forming of Ti-6Al-4V, Addit. Manuf. 21 (2018) 30–40.

[8] M. Chiumenti, M. Cervera, A. Salmi, et al., Finite element modeling of multi-pass welding and shaped metal deposition processes, Comput. Methods Appl. Mech. Eng. 199 (37–40) (2010) 2343–2359.

[9] S. Marimuthu, D. Clark, J. Allen, et al., Finite element modelling of substrate thermal distortion in direct laser additive manufacture of an aero-engine component, Proc. Inst. Mech. Eng. Part. C J. Mech. Eng. Sci. 227 (9) (2013) 1987–1999.

[10] Q. Yang, P. Zhang, L. Cheng, et al., Finite element modeling and validation of thermomechanical behavior of Ti-6Al-4V in directed energy deposition additive manufacturing, Addit. Manuf. 12 (2016) 169–177.

[11] E.R. Denlinger, J.C. Heigel, P. Michaleris, Residual stress and distortion modeling of electron beam direct manufacturing Ti-6Al-4V, Proc. Inst. Mech. Eng., Part. B: J. Eng. Manuf. 229 (10) (2015) 1803–1810.

[12] Z. Wang, E. Denlinger, P. Michaleris, et al., Residual stress mapping in Inconel 625 fabricated through additive manufacturing: method for neutron diffraction measurements to validate thermomechanical model predictions, Mater. Des. 113 (2017) 169–177.

[13] Z. Wang, A.D. Stoica, D. Ma, et al., Diffraction and single-crystal elastic constants of Inconel 625 at room and elevated temperatures determined by neutron diffraction, Mater. Sci. Eng.: A 674 (2016) 406–412.

[14] Li, L., Zhang, X., Cui, W. et al. Temperature and residual stress distribution of FGM parts by DED process: modeling and experimental validation. Int J Adv Manuf Technol 109, 451–462.

[15] J.C. Heigel, P. Michaleris, E.W. Reutzel, Thermo-mechanical model development and validation of directed energy deposition additive manufacturing of Ti–6Al–4V, Addit. Manuf. 5 (2015) 9–19.

[16] Lu, Xufei, Xin Lin, Michele Chiumenti, Miguel Cervera, Yunlong Hu, Xianglin Ji, Liang Ma, Haiou Yang, and Weidong Huang. "Residual stress and distortion of rectangular and S-shaped Ti-6Al-4V parts by Directed Energy Deposition: modelling and experimental calibration." Additive Manufacturing 26 (2019): 166-179.

[17] Ali H, Ghadbeigi H, MumtazK (2018) Residual stress development in selective laser-melted Ti6Al4V: a parametric thermal modelling approach. Int J Adv Manuf Technol 97:2621–2633.

[18] Zhang, Z., P. Ge, X. X. Yao, T. Li, and W. W. Liu. "Numerical studies of residual states and scaling effects in laser-directed energy deposition additive manufacturing." The International Journal of Advanced Manufacturing Technology 108, no. 4 (2020): 1233-1247.

[19] Li, C., J. F. Liu, X. Y. Fang, and Y. B. Guo. "Efficient predictive model of part distortion and residual stress in selective laser melting." Additive Manufacturing 17 (2017): 157-168.

[20] Li, L., Pan, T., Zhang, X., Chen, Y., Cui, W., Yan, L. and Liou, F., 2021. Deformations and stresses prediction of cantilever structures fabricated by selective laser melting process. Rapid Prototyping Journal.

[21] Keller, N., et al. "Thermo-mechanical Simulation of Additive Layer Manufacturing of Titanium Aerospace structures." LightMAT Conference. Vol. 3. No. 5. 2013.

[22] Neugebauer, Fabian, et al. "Simulation of selective laser melting using process specific layer based meshing." Proc. Fraunhofer Direct Digital Manufacturing Conf.(DDMC 2014), Axel Demmer, Aachen, Germany. 2014.

[23] Lei Yan, Tan Pan, Joseph W. Newkirk, Frank Liou, Eric E. Thomas, Andrew H. Bake, James B. Castle, Fast Prediction of Thermal History in Large-Scale Parts Fabricated Via a Laser Metal Deposition Process, Solid Freeform Fabrication 2018: Proceedings of the 29th Annual International.

[24] Michael F. Zaeh, Gregor Branner, Investigations on residual stresses and deformations in selective laser melting, Prod. Eng. Res. Devel. (2010) 4:35–45.

[25] Bayat, Mohamad, Christopher G. Klingaa, Sankhya Mohanty, David De Baere, Jesper Thorborg, Niels S. Tiedje, and Jesper H. Hattel. "Part-scale thermo-mechanical modelling of distortions in Laser Powder Bed Fusion–Analysis of the sequential flash heating method with experimental validation." Additive Manufacturing 36 (2020): 101508.

[26] M. Megahed, H.-W. Mindt, N. N'Dri, H. Duan, O. Desmaison, Metal additive manufacturing process and residual stress modeling, Integrat. Mater. Manuf. Innov. 5 (2016) 1–33.

[27] P. Peyre, P. Aubry, R. Fabbro, R. Neveu, A. Longuet, Analytical and numerical modelling of the direct metal deposition laser process, J. Phys. D Appl. Phys. 41(2018)025403.

[28] Jeff Irwin, P. Michaleris, A Line Heat Input Model for Additive Manufacturing, J. Manuf. Sci. Eng 138(11), 111004 (Jun 23, 2016).

[29] ANSYS Theory Manual, Release 8.1, ANSYS Inc., USA, 2004.

[30] Ole Sigmund, Notes and Exercises for the Course:FEM-Heavy (41525), Technical University of Denmark, 2011.

[31] Cao, Jun, Michael A. Gharghouri, and Philip Nash. "Finite-element analysis and experimental validation of thermal residual stress and distortion in electron beam additive manufactured Ti-6Al-4V build plates." Journal of Materials Processing Technology 237 (2016): 409-419.

[32] I. Setien, M. Chiumenti, S.V.D. Veen, et al., Empirical methodology to determine inherent strains in additive manufacturing, Comput. Math. Appl. (2018).

[33] P. Michaleris, L. Zhang, S.R. Bhide, et al., Evaluation of 2D, 3D and applied plastic strain methods for predicting buckling welding distortion and residual stress, Sci.Technol. Weld. Join. 11 (6) (2006) 707–716. X. Lu et al. Additive Manufacturing 26 (2019) 166–179.

[34] Xiong, J., Li, R., Lei, Y., Chen, H., 2018. Heat propagation of circular thin-walled parts fabricated in additive manufacturing using gas metal arc welding. J. Mater. Proc.Technol. 251, 12–19.

[35] J. Ding, P. Colegrove, J. Mehnen, et al., A computationally efficient finite element model of wire and arc additive manufacture, Int. J. Adv. Manuf. Technol. 70 (1-4) (2014) 227–236.

[36] B.A. Szost, S. Terzi, F. Martina, et al., A comparative study of additive manufacturing techniques: residual stress and microstructural analysis of CLAD and WAAM printed Ti–6Al–4V components, Mater. Des. 89 (2016) 559–567.

[37] J. Cao, M.A. Gharghouri, P. Nash, Finite-element analysis and experimental validation of thermal residual stress and distortion in electron beam additive manufactured Ti-6Al-4V build plates, J. Mater. Process. Technol. 237 (2016) 409–419.

[38] N. Hoye, H.J. Li, D. Cuiuri, et al., Measurement of residual stresses in titanium aerospace components formed via additive manufacturing, Mater. Sci. Forum 777 (2014) 124–129. Trans Tech Publications.

[39] Yan, Lei, Wenyuan Cui, Joseph W. Newkirk, Frank Liou, Eric E. Thomas, Andrew H. Baker, and James B. Castle. "Build Strategy Investigation of Ti-6Al-4V Produced Via a Hybrid Manufacturing Process." JOM 70, no. 9 (2018): 1706-1713.

II. TEMPERATURE AND RESIDUAL STRESS DISTRIBUTION OF FGM PARTS BY DED PROCESS: MODELLING AND EXPERIMENTAL VALIDATION

Lan Li[1], Xinchang Zhang[1], Wenyuan Cui[1], Frank Liou[1], Wen Deng[2], Wei Li[3]

[1]Department of Mechanical and Aerospace Engineering, Missouri University of Science and Technology, Rolla, MO 65409

[2]Department of Civil, Architectural, and Environmental Engineering, Missouri University of Science and Technology, Rolla, MO 65409

[3]Department of Mechanical Engineering, The University of Texas at Dallas, Richardson, TX 75080

ABSTRACT

Laser direct energy deposition (DED) is an advanced additive manufacturing technology, which can produce fully dense and functionally graded materials (FGMs) metal parts. Residual stress and distortion are crucial issues in DED process reducing the mechanical strength and the geometrical accuracy of the fabricated components. This work provided a combined approach involving thermo-mechanical model and experimental validation toward two FGMs cases fabricated by DED process to reveal the residual stress and distortion distribution. Two fabrication approaches were used: a direct deposition of Cu on SS304L and a structure graded from iron alloy SS316L to nickel alloy In718 to pure Cu based on SS304L substrate. Thermal histories of the substrate and the residual stress on cross section of the FGM part were measured to calibrate the 3D coupled thermo-mechanical model. The predicted temperature and stress results showed a good agreement with the experimental measurements. The distortion results of both

fabricated walls showed an upwards bent trend. Because of the high-temperature gradient induced by the mismatch in the thermal expansion coefficient of different materials, very high distortion was observed at two edge regions of the second printing material of FGM part. From the residual stress standpoint, direct joining Cu on SS304L resulted in extremely high residual stress at the bi-material interface due to mismatch in the thermal expansion coefficient of different materials. By introducing SS316L and In718 buffer layers, defect-free Cu can be successfully deposited on SS304L. This model can be used to predict the stress behavior of products fabricated by DED process and to help with the optimization of design and material chosen of FGMs process.

1. INTRODUCTION

The laser direct energy deposition (DED) technique, also known as the laser engineered net shaping (LENS), directed metal deposition (DMD), is a layer by layer additive manufacturing (AM) process that can build fully dense complex parts following CAD data by layered deposition [1]. In this process, the deposited material is melted by the high-power laser with a very small concentration area to create a melt pool. Irradiating by the laser energy, the newly adding material undergoes melting and cooling cycles, and then solidifies to form a deposition, thereby forming a good bond between two materials. The next layer is then built upon the previous one, resulting in a 3D part. Because of the layer after layer building manner, DED technique has the possibility to design internal features and does not require special tooling, thus it has many benefits compared with traditional manufacturing techniques, such as casting or powder

metallurgy [2]. Because of the highly concentrated laser beam, distortions and residual stresses generate due to the high thermal gradient during rapid heating and cooling cycles during the part forming process. Process defects, such as warping, crack and delamination, induced by residual stress, will reduce the mechanical strength and the geometrical accuracy of the fabricated components. Moreover, distortions and residual stresses are associated with experimental parameters, component features and thermophysical properties of the deposited material and the interlayer dwell time [3-5].

A number of previous studies focused on experimental and/or modeled thermal and residual stresses distribution for DED process were developed [6-12]. Lu et al. [13] studied the evolution of residual stresses and distortions for Ti6Al4V parts fabricated by DED technology. In their work, they concluded that the stresses and distortion were much more strongly affected by heat input rather than by powder feeding rate. What is more, they found that substrate preheating can reduce the residual stresses but may increase the final distortion. Liu et al. [14] presented a 3D sequentially coupled thermo-mechanical finite element model in ABAQUS to predict residual stresses and distortions for a DED process built. A laser displacement sensor was conducted to track the displacement of the substrate. The comparisons between the simulated and experimental results showed good agreement. Yang et al. [15] proposed a 3D thermo-elastic-plastic model to predict the thermomechanical behavior when printing Ti6Al4V. It was shown that the computed thermal history and mechanical distortions were in good agreement with the experimental measurements. In Heigel's work [16], a thermo-mechanical model was developed. Three depositions with different geometries and dwell times were used to analyze the influence on the temperature and distortion as well as residual stress.

Labudovic et al. [17] developed a 3D sequential thermo-mechanical model to study the thermal and stress development during the fabrication of a thin wall. They also analyzed the effect of preheating strategies and heat treatment on the development of residual stresses.

DED machine usually equips with two or more powder feeders with dissimilar materials. This capability allows DED to produce directly joining structures and compositionally graded structures using disparate materials. Direct joining of dissimilar materials may have cracking, delamination and high level of residual stress at the sharp interface due to lack of solubility and mismatch in thermal expansion coefficient. Inserting intermediate layers between dissimilar metals to make functionally graded materials (FGMs) has been developed to mitigate such issues [18-24]. FGMs parts give the possibility of selecting material distribution to achieve the desired functions gradually into the requires [25]. Many studies have been conducted to demonstrate FGMs are very suitable for applications which require different material properties according to locations to accomplish better functions and properties. For example, Titanium alloys can be used in the process of fabricating FMGs structures to avoid the formation of undesirable intermetallic phases [26-32]. By combining Inconel with the properties of high strength and good corrosion and stainless steel with the properties of low cost, fabrications of joining steel and Inconel alloy have been studied to learn the impacts of phases and microstructure evolution on mechanical properties [33-36]. Because of the extremely high laser reflectance and excellent thermal conductivity, very limited amount of laser radiation can be absorbed by Cu in DED process. When directly joining Cu with SS304L, there are several issues associated poor bonding at the bi-material interface because very

few amounts of copper can be dissolved with iron [37]. Nickel can form a solid solution with copper and iron [38], thus nickel alloy like In718 was used as intermediate materials to combine copper and steel. Therefore, it is crucial to reveal the mechanical properties of joining copper on SS304L with intermediate layers. Besides the difference in thermal expansion coefficient between dissimilar graded materials can affect residual stress distribution.

This work provided a combined approach involving thermo-mechanical model and experimental validation toward two FGMs parts fabricated by DED process to reveal the residual stress and distortion distribution. Two fabrication approaches were used: direct deposition of Cu on SS304L and via SS316 and In718 multi-interlayers. In case 1, Cu was directly joined to SS304L. In case 2, a single wall multi-layer graded part was fabricated from iron alloy SS316L to nickel alloy In718 to pure Cu based on an SS304L substrate. Section 2 was dedicated to the detailed description of the thermo-mechanical FEA model in software Ansys to predict distortion and residual stress fields. The actual parameters and graded strategy were discussed in detail. The material properties during the process were temperature dependent. Section 3 gathered all the experimental work carrying out printing and post-machining of the graded structures to develop the validation. Then the discussion on thermal, distortion and stress distribution were described in Section 4. The predicted temperature and residual stress distributions were compared with the corresponding experimental results. Studying their sensitivity to mechanical properties of both distortions and residual stresses could reveal the graded transition of the graded materials along the building up direction. Then conclusions drawn about the benefits of introducing buffer FGM interlayers were followed.

2. FINITE ELEMENT MODEL

2.1. MODEL SETUP

Two fabrication approaches were used: direct deposition of Cu on SS304L and via SS316 and In718 multi-interlayers. As for the direct joint of Cu/SS304L sample, single track-16 layer with the dimension of 3 mm wide and 4.8 mm tall, was built on SS304L substrate with the dimension of 60 mm × 12 mm × 5 mm. The single-track multi-layer graded part, with a transition composition route: SS316→ In718→Cu, with the dimension of 3 mm wide and 14.2 mm tall, was built on the same SS304L substrate. Sixteen layers of SS316L were deposited as the first graded material. Followed by In718 with ten layers and Cu with sixteen layers. The schematic and photograph of two specimens after deposition are shown in Figure 1. The laser scanning is following a traditional zig-zag deposition strategy as it scans back and forth shown in Figure 2 (a). To reduce computational time, the elements of deposited materials were finely meshed with hexahedral element size of one layer thickness whereas the substrate away from the laser irradiation region was meshed sparsely of 1 mm. The final model contained total 45,168 elements for the case 2 in Figure 2(b).

For 3D thermal and structural analyses, an 8-noded brick element has been chosen in Software Ansys, including the element type Solid70. The meshes stay the same during thermal and structural simulations. In the coordinate system, x-direction is defined as deposition direction as the laser moves along, y-direction is normal to the deposition direction, and z-direction is the building up direction.

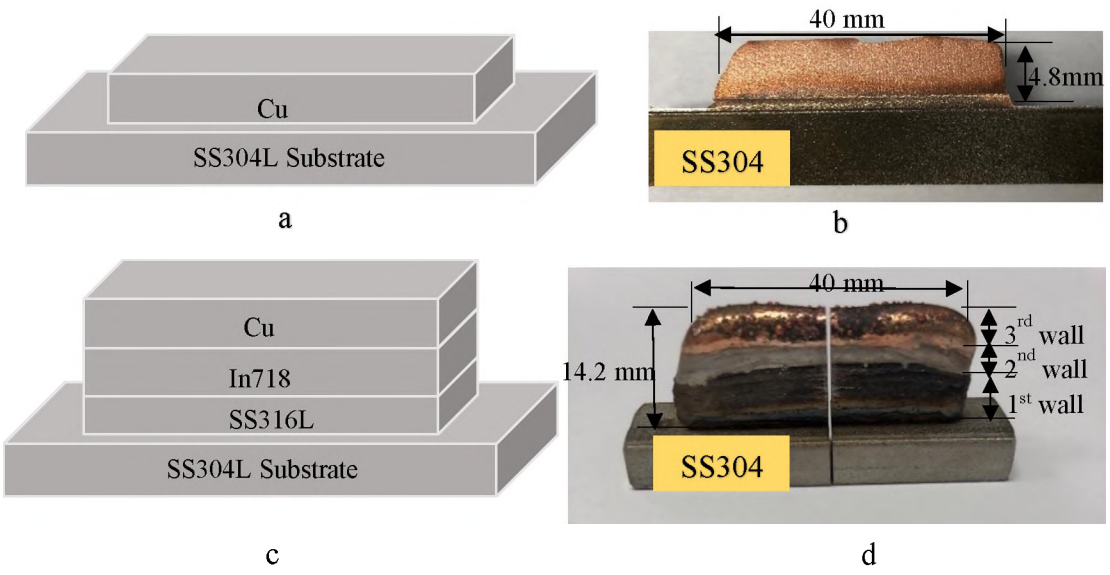

Figure 1. (a) Schematic of direct joining specimen; (b) Photograph of direct joining specimen after cutting; (c) Schematic of gradient alloy specimen; (d) Photograph of gradient alloy specimen after cutting.

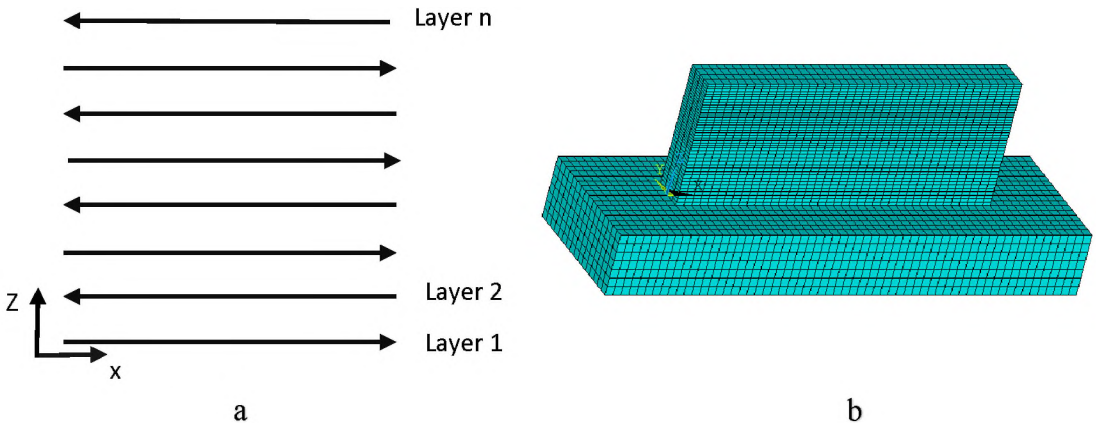

Figure 2. (a) Track path for laser deposition; (b) Mesh used for the FEA simulation of the FGM part.

The 3D coupled thermo-mechanical analysis was conducted to predict the temperature and residual stress history during DED process [39]. First, the transient

thermal analysis was calculated. Then the computed temperature results were used as the thermal load to calculate the thermal stress and distortion. The element birth-and-death function was used to activate or deactivate an element to simulate the deposition action. There were 6 elements placed across the laser beam diameter and 1 element per layer thickness active every time step. At the start of the simulation, the substrate elements were all activated. The elements of the new added were activated sequentially to simulate material addition process.

2.2. GOVERNING EQUATION FOR HEAT TRANSFER AND THERMAL STRESS

The governing transient heat conduction transfer equation in the entire volume of the material is given as

$$\rho c_p \frac{\partial T}{\partial t} = \frac{\partial}{\partial x}(k\frac{\partial T}{\partial x}) + \frac{\partial}{\partial y}(k\frac{\partial T}{\partial y}) + \frac{\partial}{\partial z}(k\frac{\partial T}{\partial z}) + Q \tag{1}$$

where k is the thermal conductivity, ρ is the density, c_p is the specific heat, both of the thermal conductivity and thermal diffusivity are temperature dependent, T is the current temperature, Q is the volumetric heat generation rate, t is the time, x, y and z are the coordinates in the reference system.

The governing mechanical equilibrium equation is written as [40-41]:

$$\nabla \cdot \sigma = 0 \tag{2}$$

where σ is the second-order stress tensor associated with the material behavior law.

Considering the elastoplastic behavior of the material, strain, and stress can be written as

$$\sigma = C\varepsilon^e \tag{3}$$

where C is the fourth order material stiffness tensor and ε^e is the second-order elastic strain tensor.

Total strain ε, assuming small deformation thermo-elasto-plasticity, is decomposed as [42]:

$$\boldsymbol{\varepsilon} = \boldsymbol{\varepsilon}^e + \boldsymbol{\varepsilon}^p + \boldsymbol{\varepsilon}^{th} \tag{4}$$

where ε^e, ε^p, and ε^{th} are the elastic strain, plastic strain, and thermal strain, respectively. Both of them contribute to total displacement. The isotropic Hooke's law was used to model the elastic strain in Equation (3). The thermal expansion coefficient was adopted to calculate the thermal strain.

To match the circular-shaped laser beam with a constant and uniform power density in experiment setup, the heat source parameter was considered a constant and uniformly distributed body heat flux defined as:

$$Q = \frac{\alpha P}{\pi r^2 t} \tag{5}$$

where α is the absorption coefficient, P is the power of the continuous laser, r is the radius of the laser beam and t is the layer thickness.

2.3. BOUNDARY CONDITIONS

The initial condition throughout the whole deposited material and substrate is considered as uniform temperature distribution:

$$T(x, y, z, t)_{t=0} = T_0 = T_a \tag{6}$$

where T_a is the ambient temperature equals to the initial temperature T_0, set as 25 °C.

Both heat radiation and heat convection conditions applied to all the external surfaces of metal deposition layer. Boundary conditions are expressed as:

$$q_c = h\left(T - T_a\right) \tag{7}$$

$$q_r = \varepsilon\sigma\left(T^4 - T_a^4\right) \tag{8}$$

$$h = 2.27 \times \Delta T^{0.45} \tag{9}$$

where h is the heat transfer coefficient of natural thermal convection, which is assumed to be temperature dependent expressed in Equation (9), ΔT is the temperature difference between room temperature, σ is the Stefan–Boltzmann constant of 5.67×10^{-8} W/m^2·K^4 and ε is the material emissivity of 0.38.

Body motion of the substrate is rigid by the clamp on two side surfaces, thus it is necessary to define freedom of side surface to be zero as the boundary conditions in the structural analysis.

2.4. THERMO-PHYSICAL AND MECHANICAL PROPERTIES

The thermo-physical and mechanical properties of SS304L, SS316L, In718 and Cu powders used in this model were temperature-dependent and identified in several papers [13, 43-47], as shown from Table 1-4. For temperatures above the melting point, effective thermal conductivity was considered to compensate for the fluid flow in the molten pool. In thermo-physical model, the latent heat effects of the phase transformations were accounted by the calculation of heat capacity. The mechanical behavior was described by a bilinear stress-strain curve starting at the origin with positive stress and strain values [48], which was defined by elastic modulus E, Poisson's ratio v,

Table 1. Thermo-mechanical properties of the stainless steel 304L substrate.

Temperature (°C)	25	100	200	300	400	600	800	1200	1300	1500
Density (kg/m3)	790	788	783	779	775	766	756	737	732	732
Thermal conductivity (W/(mK))	14.6	15.1	16.1	17.9	18	20.8	23.9	32.2	33.7	120
Specific heat (J/(kgK))	462	496	512	525	540	577	604	676	692	720
Thermal expansion coefficient (10^{-6}/K)	17	17.4	18	18.6	19	19.6	20	20.7	21.1	21.6
Poisson's ratio	0.29	0.295	0.3	0.31	0.32	0.33	0.34	0.34	0.35	0.39
Elastic modulus (GPa)	198	193	185	176	167	159	151	60	20	10
Yield strength (MPa)	265	218	186	170	155	149	91	25	21	10

Table 2. Thermo-mechanical properties of the stainless steel 316L.

Temperature (°C)	25	200	400	600	800	1000	1200	1400	1600
Density (kg/m3)	7957	7876	7783	7687	7588	7485	7361	7270	6880
Thermal conductivity (W/(mK))	13.9	16.7	19.8	23	26.1	29.3	31	32	150
Specific heat (J/(kgK))	501	525	552	579	606	633	700	720	830
Thermal expansion coefficient (10^{-6}/K)	14.8	15.3	16.2	16.9	17.6	17	20	20	20
Poisson's ratio	0.26	0.31	0.33	0.34	0.28	0.21	0.24	0.24	0.24
Elastic modulus (GPa)	201	186	168	151	134	117	51	20	20
Yield strength (MPa)	235	163	131	108	75	52	15	10	1

Table 3. Thermo-mechanical properties of In718.

Temperature (°C)	25	227	427	727	927	1127	1260	1344	1450
Density (kg/m3)	8220	8120	8040	7961	7875	7787	7733	7579	7488
Thermal conductivity (W/(mK))	12	14	17	22	26	23	20	100	100
Specific heat (J/(kgK))	421	453	481	562	636	650	652	652	652
Thermal expansion coefficient (10^{-6}/K)	10	13	14	15	17	18	18	18	18
Poisson's ratio	0.3	0.3	0.32	0.33	0.35	0.4	0.4	0.4	0.4
Elastic modulus (GPa)	165	160	152	110	55	34	10	1	1
Yield strength (MPa)	648	602	558	356	90	34	10	1	1

Table 4. Thermo-mechanical properties of pure Cu.

Temperature (°C)	25	100	200	300	400	500	600	900	1085
Density (kg/m3)	8930	8890	8850	8800	8740	8700	8630	8430	8000
Thermal conductivity (W/(mK))	400	395	388	382	376	370	363	343	340
Specific heat (J/(kgK))	385	397	408	419	427	434	441	460	495
Thermal expansion coefficient (10^{-6}/K)	15	15.5	16	16.5	17	17	17	17	17
Poisson's ratio	0.35	0.35	0.35	0.35	0.35	0.35	0.35	0.35	0.35
Elastic modulus (GPa)	120	120	118	115	108	103	80	30	20
Yield strength (MPa)	210	200	180	125	85	35	10	8	8

yield strength σ_Y, and tangent modulus *Ep*. This is called bilinear isotropic hardening (BISO) model in ANSYS software, as shown in Figure 3 [49]. When temperature was above the melting point, the situation of melt pool did not hold stress was considerate in this model by setting very small values of mechanical properties.

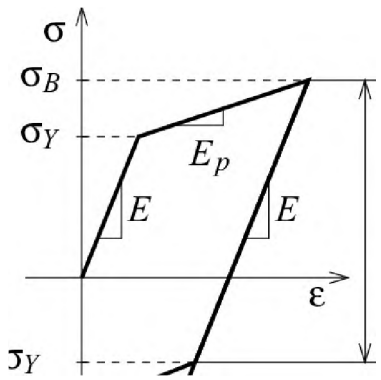

Figure 3. Bilinear stress-strain curve at a given temperature [49].

3. EXPERIMENTAL PROCEDURE

The fabrication samples were built on the DED system with varied process parameters. The DED system consists of a laser, gas feeding components, powder feeders, 3-axis computer numerical control (CNC) platform and enclosure. The CNC platform can move the substrate in XYZ three-dimensional space according to the toolpath while the laser components were stationary. The laser beam has a 1000 W maximum laser power with a 2-5 mm diameter. Particles are delivered into the melt pool through blown powder feeder carried by argon gas. Argon gas atmosphere is inserted as the shielding gas for preventing materials from oxidization. The laser processing

parameters are given in Table 5. The experimental setup and cross section of the graded sample after cutting preparation are depicted in Figure 4.

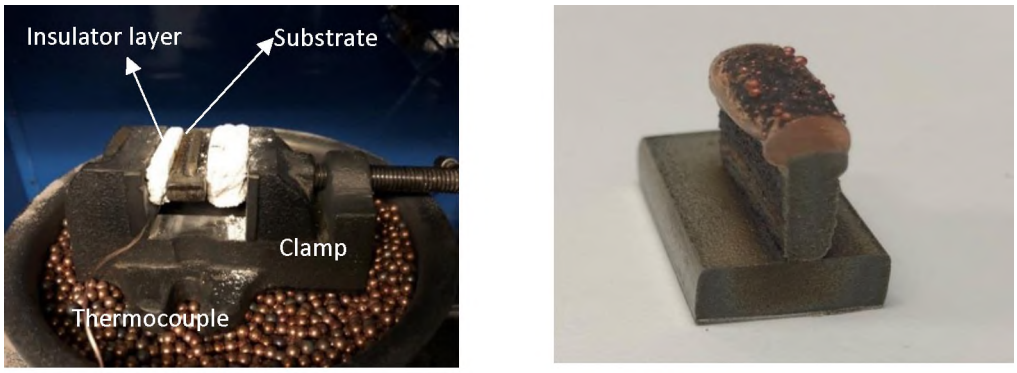

a b

Figure 4. (a) Experimental setup to measure the temperatures of the base-plate during the DED process; (b) Final prepared graded specimen.

Table 5. Laser processing parameters in DED process.

Parameters	Case 1	Case 2		
	Cu	SS316	In718	Cu
Laser power, W	850	600	600	850
Laser diameter, mm	3	3	3	3
Scan speed, mm/min	240	240	240	240
Deposite height, mm	0.3	0.4	0.3	0.3
Deposite length, mm	40	40	40	40
Number of layers	16	16	10	16
Total thickness of this material, mm	4.8	6.4	3	4.8
Total thickness of this sample, mm	4.8	14.2		

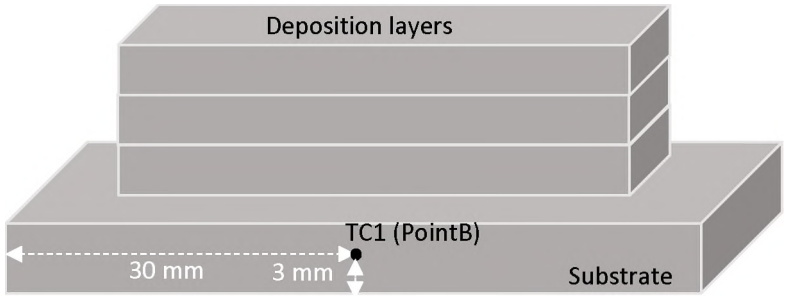

Figure 5. Location of the thermocouple on the side of the substrate.

In order to validate the thermal simulation, a type K thermocouple with the measurement uncertainty of 0.096 °C was attached to the substrate at one side, 3 mm above the bottom surface. The type K thermocouple was connected to DI-245 USB thermocouple data acquisition system to collect temperature data. Its locations relative to the deposition are geometrically shown in Figure 5.

4. RESULTS AND DISCUSSION

4.1. THERMAL RESULT AND VALIDATION

Figure 6(a) shows the simulated temperature history of the graded specimen during the deposition at two selected positions, Point A and B. Point A is located at the middle of first track of the first printing material on the substrate. Point B is located at side surface of the substrate, same location with the thermocouple of TC1. It is noted that the temperature evolution of Point A experiences three heating process. Each heating process represents the deposition of three different materials. It can be seen that between each heating process, a long cooling process is observed corresponding to the material

transaction. The cooling processes are marked on the graph. The maximum temperature of each heating process exceeds 1599 °C, 532 °C and 443 °C when depositing three different materials, respectively. As we zoom in the heating process during the built of each material in Figure 6(b), we can clearly see that 16,10 and 16 heating circles in each heating process. That's because there is 16 deposited layers for the first FGM material, followed by 10 deposited layers for the second FGM material and 16 deposited layers for the third FGM material when fabricating FGM part. Thus in the first heating process, the selected location of Point A experiences 16 circles corresponding to 16 deposited layers. The number of 16 cycles is marked on the graph. The first temperature peak is caused by heating up first layer, while the second temperature peak is because of the heating of the subsequent layer. The second peak temperature is a little higher than the melting point of SS316L (1385 °C), which means the solidified layer is remelted during heating of the subsequent second track. After laser deposition starts, the temperature begins to increase subsequent second track. After laser deposition starts, the temperature begins to increase gradually due to the heat accumulation of the previous printing layers. The predicted temperature history and the experimental measurements of the thermocouple location (Point B) are compared in Figure 6(c). The solid and dashed line indicates predicted temperature and the experimental measurement, respectively. It is observed that both simulation and experimental observations follow the same trends. A good agreement is achieved to validate the model.

Figure 7 presents the simulated temperature distribution of the melt pool and surrounding heat affected areas from the front view at nth deposition layer, n=1, 16, 17 and 27. It is noted that in Figure. 7(a), the temperature was not widely spread along the

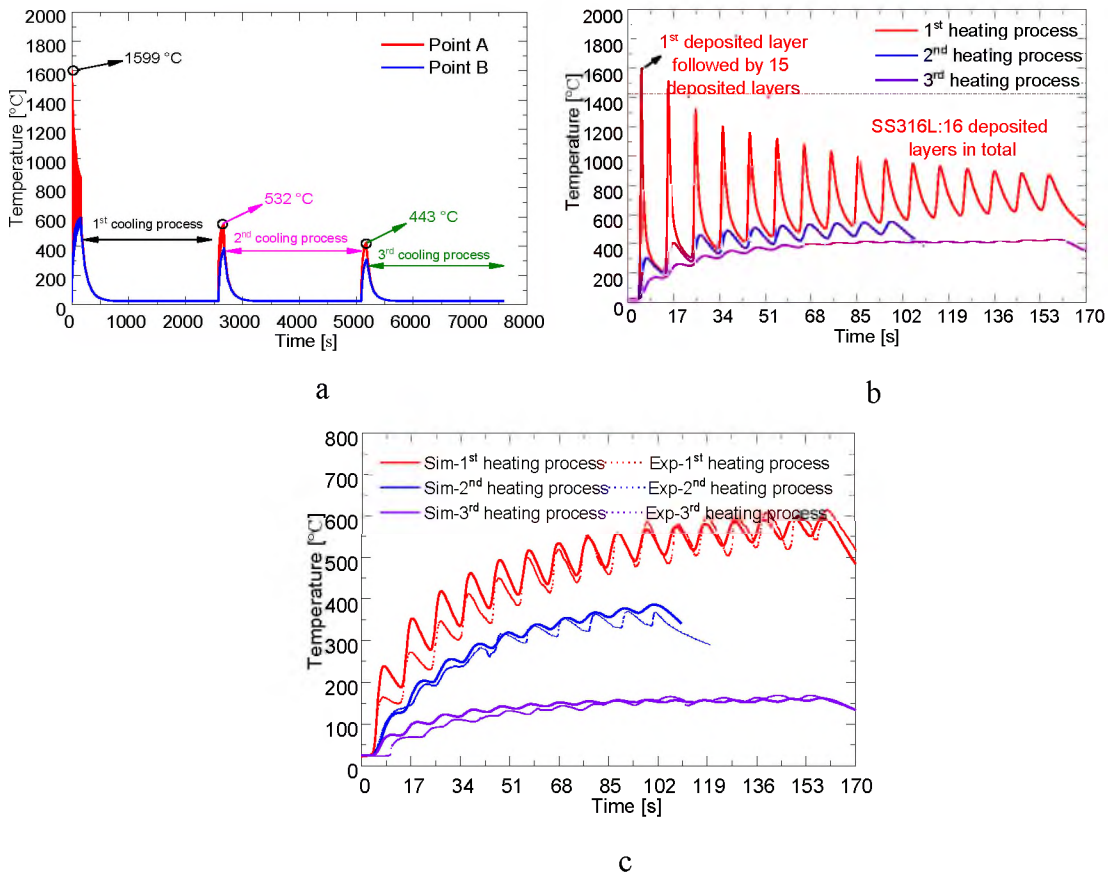

Figure 6. (a) The simulated temperature history of graded specimen during the deposition at each selected position, Point A and B; (b) Zoom in temperature history in each heating process; (c) The predicted temperature history and measurement results of Point B.

substrate because of the low thermal conductivity of the first deposited material SS316L. The maximum temperature reaches from ambient temperature of 25 °C to 1621 °C in track-1, in which the scanning direction is in x-direction. For it is just the first track of the deposition, the lowest temperature of the substrate still remains at room temperature. The overall shape of heat affected area looks like a comet, instead of a circle, which indicates the laser beam movement direction. The area in orange and red color represents the shape of the molten pool. Measured from the temperature contours, the depth of the area where

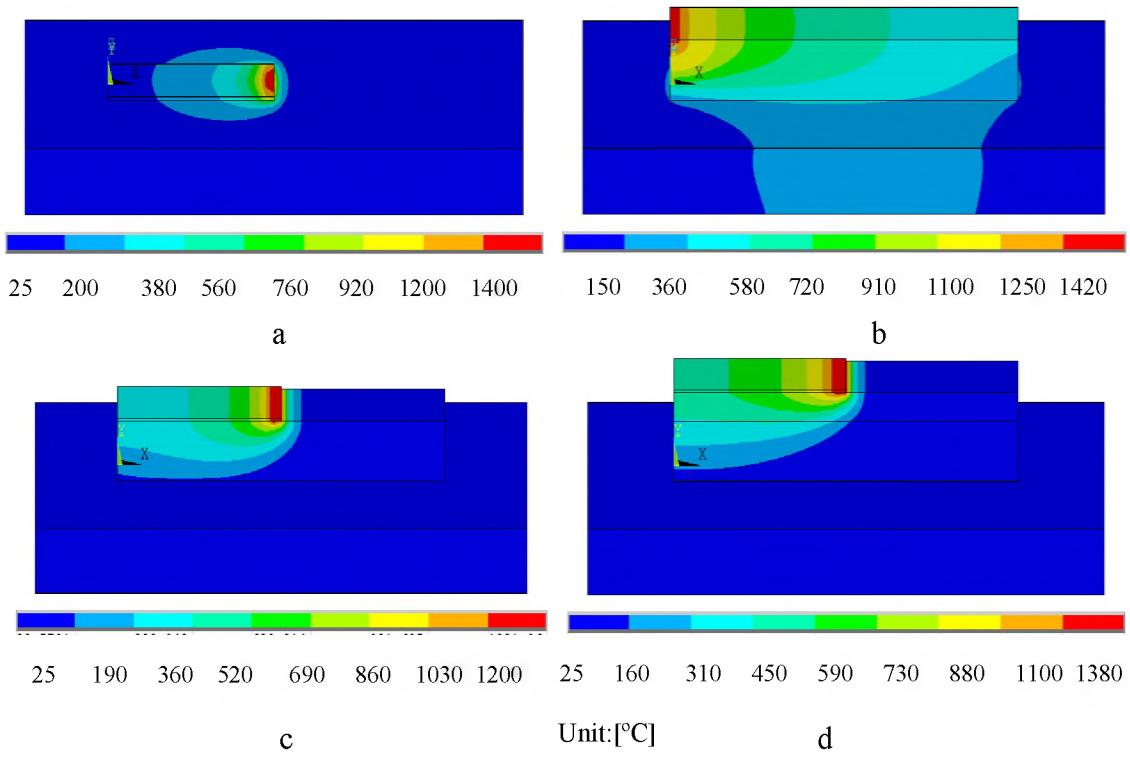

Figure 7. The simulated temperature distribution of graded specimen resulting from n^{th} deposition layers: (a) n=2; (b) n=16; (c) n=17 and (d) n=27.

the temperature is higher than 1385 °C is 0.57 mm. The melting depth is deep enough to make fully metallurgical bonding between SS316L and substrate. Because of the thermal accumulation of the previous deposition, the highest temperature increases to 1770 °C at the end of 16th track in Figure 7(b), which is the last deposited track of first FGM material SS316L. Again, the melting depth of 0.51 mm makes fully metallurgical bonding between In718 and SS316L in Figure 7(c). This is the 17^{th} deposition layer, the first deposited track of second FGM material In718. Among the thermal profiles in the entire passes, material SS316L experienced highest temperature compared to In718 and Cu. In deposition of track-27, the first track of third FGM material Cu, an extremely high

temperature gradient around interface of In718 and Cu is obviously noticed because the thermal conductivity of Cu much higher than In718.

4.2. DISTORTION AND RESIDUAL STRESS EVOLUTION

Figure 8 represents the distortion distributions in different directions within the graded specimen cooling to the ambient temperature of 25 °C. The vector along x, y and z-directions are referred as the longitudinal (scanning direction), transverse and normal displacement (which is the building up direction) respectively. Important observations

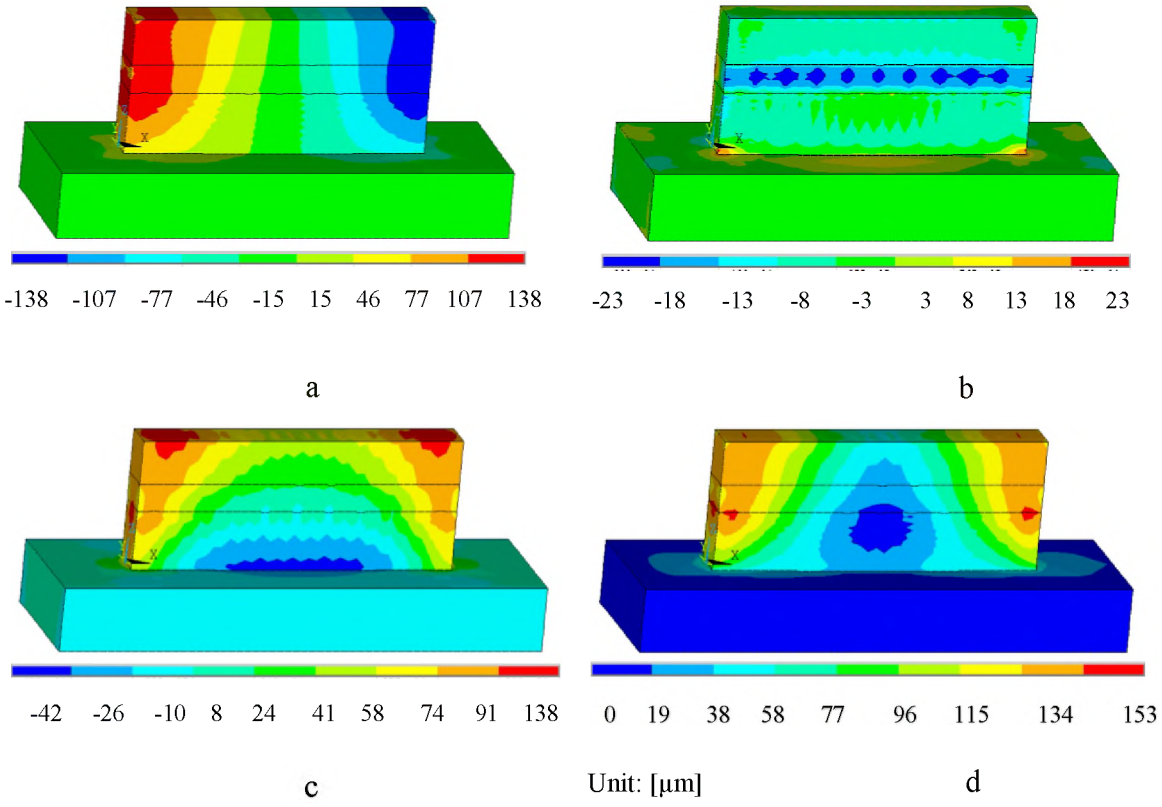

Figure 8. Calculated displacement in (a) longitudinal direction Ux; (b) transversal direction Uy, (c) normal direction Uz, and (d) total displacement Usum, for the graded specimen when the model cooling reaches 25°C.

can be made from these figures. The maximum and minimum displacement in the x-direction is formed at the tip region of the building part, with values of -0.14 mm and 0.14 mm. Due to the thermal contraction of underneath material, areas close to the center of the wall would be deformed downward and the areas far from the center would bend upward. That can be validated by Figure 8(c), -0.04 mm displacement is observed at the center area close to the interface between substrate. The maximum upward is formed at the tip region on top of the building part, with the value of 0.14 mm. Since both side surface of the substrate are clamped, y-direction bending deformation is constrained. Thus it can be seen that this graded fabricated single wall is bent upwards. Another phenomenon worth notice in Figure 8(d) of total displacement is that very high displacement is observed at two tip regions of the second deposited material. That can be explained by the high temperature gradient induced by different thermal conductivity of three graded materials. A sharp change in composition occurs at the interface of the dissimilar joints. For this reason, a very high von Mises stress is observed at In718, which is shown in Figure 9(d).

When depositing the first few layers, thermal gradient is considerably higher because of the cold substrate. The expansion of the newly deposited layer is restricted by its surrounding material, and tensile residual stress is induced on substrate near the interface area. When more layers are deposited, more heat accumulates in the substrate. For the upper top surface, heat transfer to lower layers decreases. The deposition process and local material properties highly affect residual stress distributions. From material properties side, SS316L has similar thermal conductivity with SS304L substrate, but shows dissimilar with In718 and Cu. Therefore, in SS316L to Cu joint, a high thermal

gradient induces through the deposition interface between every two materials, especially in interface area between In718 and Cu. Large residual stresses accumulate near the deposit interface caused by the steep temperature gradient.

Figure 9 represents the residual stress distributions at three different directions within the graded specimen cooling to ambient temperature of 25 °C. The longitudinal stress, transversal stress, normal stress, and von Mises stress are observed, respectively. The residual stress field is almost symmetrical with respect to the central xz-plane at y = 0 mm, therefore residual stresses are shown on this plane. The maximum longitudinal stress is acquired on the second printing layer of In 718 with a value of 315 MPa, which is in a tensile state. In addition, it can be seen that there is compressive stress near the interface between In718 and Cu with a magnitude of 529 MPa. It can be explained by the following. During the deposition of third material of Cu, the narrow interface area, including the deposited metal and heat affected zone, tends to increase its volume due to the thermal expansion. While the beneath cold metal of In 718 with high rigidity, prevents the expansion of the heating area, thus transient compressive stress appears in this area. Also, an area of increased tensile stresses is observed at the lower part of the build, shown in Figure 9(b) and Figure 9(c). For von Mises stress in Figure 9(d), a very high value of 600 MPa is also observed at this interface, which is still smaller than the yield stress of In718 at room temperature (σy= 625 MPa).

When compared with the calculated total displacement and von Mises stress for the direct joining part of Cu to SS304L in Figure 10. The maximum displacement is for med at the tip region of the building part, with values of 0.04 mm, making an upward

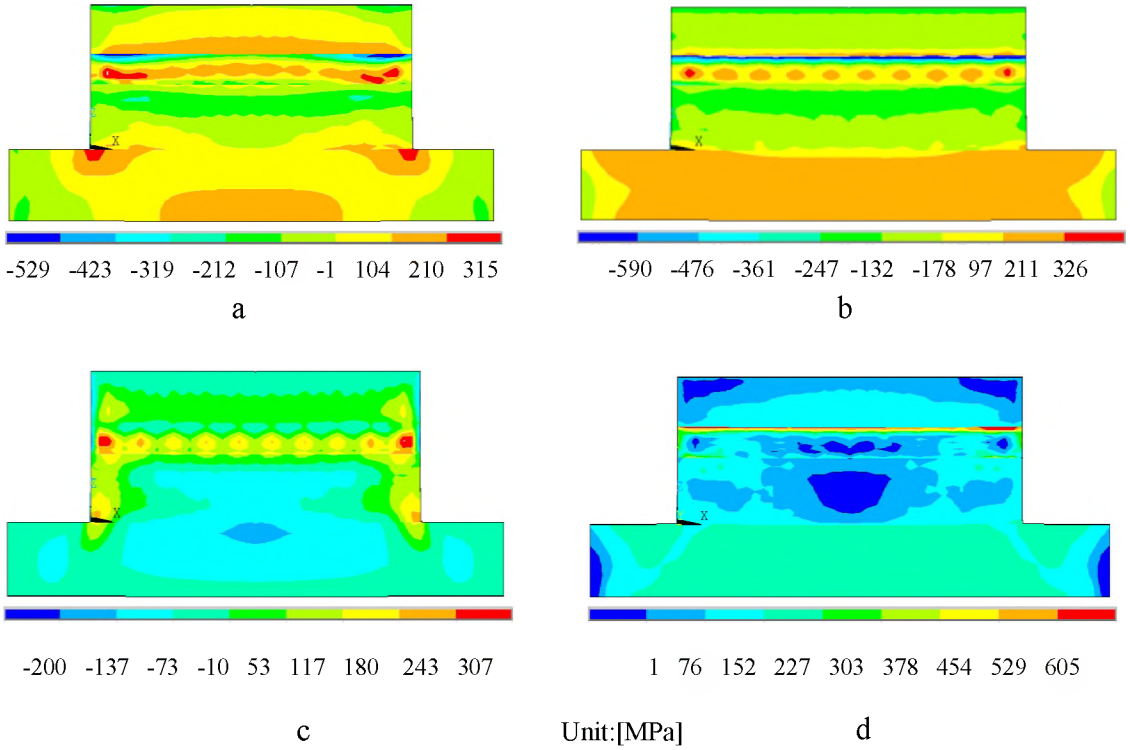

Figure 9. Calculated residual stresses in (a) longitudinal direction Sxx; (b) transversal direction Syy, (c) normal direction Szz, and (d) von Mises stress Seqv, for the graded specimen when the model cooling reaches 25 °C.

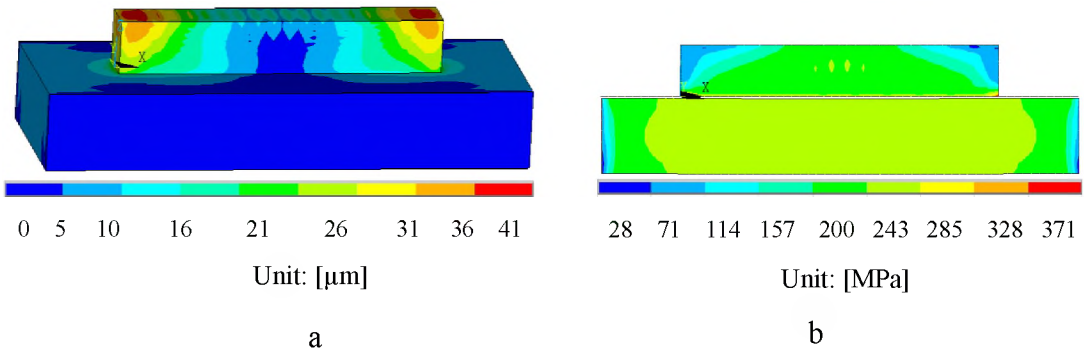

Figure 10. The calculated (a) total displacement Usum, and (b) von Mises stress Seqv, for the direct joining when the model cooling reaches 25 °C.

bending. In the heating process, thermal expansion of Cu was restricted by the cooler substrate thus resulting in tensile stress in the substrate and compressive stress in Cu. While in the cooling process, shrinkage of Cu was restricted by the substrate, resulting in compressive stress in substrate and tensile stress in Cu. Therefore, the substrate and Cu experienced cyclic tensile and compressive stresses. Because of the different thermal expansion coefficient of SS304L (3.8×10^{-6}/°C) and Cu (17×10^{-6}/°C), the maximum stress was observed at the bonding area, with the value of 371 MPa, which surpassed the yield stress of Cu and SS304L at room temperature (σy= 210 MPa and 225 MPa). Thus from residual stress standpoint, direct joining Cu on SS304L may induce delamination or crack at the bi-material interface. From the SEM micrographs of Cu direct joining to steel structure at the interfacial area, it was observed that Cu was able to adhere to stainless steel but micro-cracks were presented, as shown in Figure 11 [50-52]. Thus by introducing SS316L and In718 buffer layers, defect-free copper can be successfully deposited on SS304L.

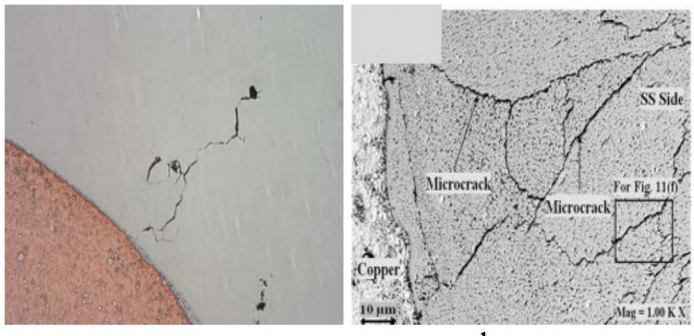

Figure 11. SEM image of (a) Cu-stainless steel and (b) Cu-Stainless steel 304 at the bi-material interfacial zone [50-51].

4.3. EXPERIMENTALLY MEASURED RESIDUAL STRESS DISTRIBUTION AND STRESS RESULT VALIDATION

Distribution of predicted von Mises stresses along line L (which is at xz-plane at y = 0 mm and x=20 mm) as well as experimental values for the graded specimen are shown in Figure 12. Measured residual stresses were obtained using X-ray diffraction (XRD) with sin2ψ technique [53]. The basic principle of measuring the residual stress by XRD technique is to measure the diffraction line displacement as the original data. When there is residual stress in the sample, the spacing between the lattice planes will change. When Bragg diffraction occurs, the diffraction peak will move, and the moving distance is

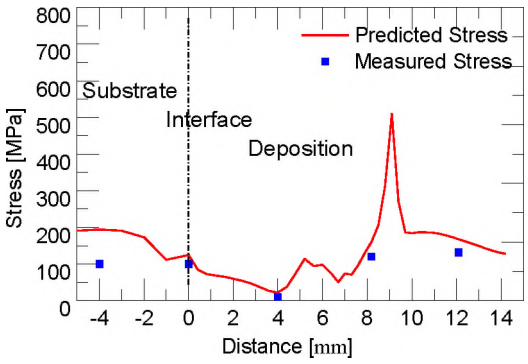

Figure 12. Comparison of experimentally measured and numerically computed von Mises stress along Path L.

related to the magnitude of the stress. With X-rays, the sample is irradiated with different incidence angles several times, then the corresponding diffraction angle 2θ is measured. The angle ψ, defining the orientation of the sample surface, is the angle between the normal to the diffracting lattice planes and the sample surface. The slope M of 2θ to sin2ψ is obtained, and then stress can be calculated.

The individual spots represent the experimental data in Figure 12. The solid line represents predicted data obtained from simulation. The interface between the substrate is indicated by the dashed vertical lines. The measured and simulation data exhibit a trend where the greatest stress occurs near the interface between In718 and Cu. Experimental and calculated curves have a satisfactory agreement, except a bit mismatch farther away from the substrate (where z=-4mm on the substrate). Several factors contributed to the prediction accuracy. One error comes from the cutting of the sample which leads to a relaxation of some residual stresses. This would lead to a relaxation of accumulated thermal stress and reduce it compared to an actual part. The lack of material properties at high temperature can also lead to some assumption in this model. It can be concluded that the developed simulation procedure can be a successful and efficient validation in the parts fabricated by the DED process.

5. CONCLUSION

This work provided a combined approach involving experiments and thermo-mechanical FEA models toward two fabrications made by DED process to reveal the residual stress and distortion. Two fabrication approaches were used: a direct deposition of Cu on SS304L and a structure graded from iron alloy SS316L to nickel alloy In718 to Cu based on an SS304L substrate. Thermal histories of the substrate were measured first to calibrate the 3D coupled thermo-mechanical model. Once validated, the model has been used to explore residual stresses and distortions. The main conclusions of this work are provided as follows:

1) The predicted temperature history was in good agreement with the experimental results. The graded structure experienced three stages in total, corresponding three heating and cooling processes of depositing three FGM materials.

2) It can be seen that both fabricated walls were bent upwards. High-temperature gradient induced by mismatch in thermal expansion coefficient of different material lead to high displacement at interface region. For the graded structure, very high displacement with the value of 0.15 mm was observed at two tip regions of the second printing material of In718.

3) High thermal gradient was observed at the interface between every two different materials, especially interface area between In718 and Cu. Thus large residual stresses accumulated at the deposit interface caused by steep temperature gradient. The maximum longitudinal stress was acquired in the same area with a value of 315 MPa, which was less than the yield stress. Note that the maximum residual stress in von Mises stress was also found here. While the maximum stress of the direct joining sample was observed at the bonding area, with the value of 371 MPa, which was higher than the yield stress of Cu and SS304L, thus delamination or crack would easily happen here.

From the residual stress standpoint, direct joining Cu on SS304L results in cracking at the bi-material interface due to mismatch of thermal expansion coefficient. By introducing SS316L and In718 buffer layers, defect-free Cu can be successfully deposited on SS304L. This model can be used to predict the stress behavior of products fabricated by DED process and to help with the optimization of design and material chosen of FGM process.

REFERENCES

[1] Zhang K, Liu W, Shang X (2007) Research on the processing experiments of laser metal deposition shaping. Opt Laser Technol 39(3):549–557.

[2] I. Gibson, D.W. Rosen, B. Stucker, Additive Manufacturing Technologies, Springer, 2010.

[3] T. Debroy, H. L. Wei, J. S. Zuback, T. Mukherjee, J. W. Elmer, J. O. Milewski, Allison Michelle Beese, A. Wilson-Heid, A. De, W. Zhang, Additive manufacturing of metallic components – process, structure and properties, Progress in Materials Science, 92 (2018) 112-224.

[4] D.D. Gu, W. Meiners, K. Wissenbach, R. Poprawe, Laser additive manufacturing of metallic components: materials, processes and mechanisms, International materials reviews 57, 3 (2012) 133-164.

[5] T. Mukherjee, W. Zhang, T. DebRoy, An improved prediction of residual stresses and distortion in additive manufacturing, Computational Materials Science, 126 (2017) 360-372.

[6] V.T. Em, S.Y. Ivanov, I.D. Karpov, S.A. Rylov, E.V. Zemlyakov, K.D. Babkin, Residual stress measurements of laser metal deposited Ti- 6Al-4V parts using neutron diffraction, Journal of Physics: Conference Series, 1109 (1) (2018) 012049.

[7] Z. Wang, E. Denlinger, P. Michaleris, A.D. Stoica, D. Ma, M. Beese, Residual stress mapping in Inconel 625 fabricated through additive manufacturing: Method for neutron diffraction measurements to validate thermomechanical model predictions, Materials & Design, 113 (2017) 169-177.

[8] L. Sochalski-Kolbus, E.A. Payzant, P.A. Cornwell, T.R.Watkins, S.S. Babu, R.R. Dehoff, M. Lorenz, O. Ovchinnikova, C. Duty, Comparison of residual stresses in Inconel 718 simple parts made by electron beam melting and direct laser metal sintering, Metall Mater Trans A 46 (3) (2015) 1419-1432.

[9] V. Luzin, N. Hoye, Stress in thin wall structures made by layer additive manufacturing, Materials Research Proceedings, 2 (2016) 497–502.

[10] J.C. Heigel, P. Michaleris, E.W. Reutzel, Thermo-mechanical model development and validation of directed energy deposition additive manufacturing of Ti–6Al–4V, Addit. Manuf. 5 (2015) 9–19.

[11] R. Ye, J.E. Smugeresky, B. Zheng, Y. Zhou, E.J. Lavernia, Numerical modeling of the thermal behavior during the LENS® process, Mater. Sci. Eng. A 428 (1–2) (2006)47–53.

[12] S. Ghosh, J. Choi, Three-dimensional transient finite element analysis for residual stresses in the laser aided direct metal/material deposition process, J. Laser Appl.17 (2005) 144.

[13] Xufei Lu, Xin Lin , Michele Chiumenti, Miguel Cervera, Yunlong Hu, Xianglin Ji, Liang Ma, Haiou Yang, Weidong Huang, Residual stress and distortion of rectangular and S-shaped Ti-6Al-4V parts by Directed Energy Deposition: Modelling and experimental calibration, Additive Manufacturing, Volume 26, March 2019, Pages 166-179.

[14] H Liu, TE Sparks, FW Liou, DM Dietrich. Numerical Analysis of thermal stress and deformation in Multi-Layer Laser Metal Deposition Process, 2013.

[15] Q. Yang, P. Zhang, L. Cheng, Z. Min, M. Chyu, and A. C. To, "Finite element modeling and validation of thermomechanical behavior of Ti-6Al-4V in directed energy deposition additive manufacturing," Addit. Manuf. 12, 169–177 (2016).

[16] J. C. Heigel, P. Michaleris, and E. W. Reutzel, "Thermo-mechanical model development and validation of directed energy deposition additive manufacturing of Ti–6Al–4V," Addit. Manuf. 5, 9–19 (2015).

[17] Labudovic, M., Hu, D., and Kovacevic, R., A three dimensional model for direct laser metal powder deposition and rapid prototyping, Journal of Material Science, Vol.38, 2003, pp.35-49.

[18] W. Li, X. Chen, L. Yan, J. Zhang, X. Zhang, and F. Liou, "Additive manufacturing of a new Fe-Cr-Ni alloy with gradually changing compositions with elemental powder mixes and thermodynamic calculation," Int. J. Adv. Manuf. Technol., vol. 95, no. 1, pp. 1013–1023, Mar. 2018.

[19] W. Li, L. Yan, X. Chen, J. Zhang, X. Zhang, and F. Liou, "Directed energy depositing a new Fe-Cr-Ni alloy with gradually changing composition with elemental powder mixes and particle size' effect in fabrication process," J. Mater. Process. Technol., vol. 255, pp. 96–104, 2018.

[20] X. Zhang, T. Pan, W. Li, and F. Liou, "Experimental Characterization of a Direct Metal Deposited Cobalt-Based Alloy on Tool Steel for Component Repair," JOM, vol. 71, no. 3, pp. 946–955, Mar. 2019.

[21] W. Cui, S. Karnati, X. Zhang, E. Burns, and F. Liou, "Fabrication of AlCoCrFeNi High-Entropy Alloy Coating on an AISI 304 Substrate via a CoFe2Ni Intermediate Layer," Entropy, vol. 21, no. 1, 2018.

[22] R. M. Mahamood and E. T. Akinlabi, "Laser metal deposition of functionally graded Ti6Al4V/TiC," Mater. Des., vol. 84, pp. 402–410, 2015.

[23] X. Lin, T.M. Yue, Phase formation and microstructure evolution in laser rapid forming of graded SS316L/Rene88DT alloy, Mat. Sci. Eng. A 402 (1e2) (2005) 294e306.

[24] R.W. Messler, Principles of Welding: Processes, Physics, Chemistry, and Metallurgy, John Wiley & Sons, Inc., New York, 1999.

[25] Pierre Muller, Pascal Mognol, Jean-YvesHascoet, Modeling and control of a direct laser powder deposition process for Functionally Graded Materials (FGM) parts manufacturing, Journal of Materials Processing Technology, Volume 213, Issue 5, May 2013, Pages 685-692.

[26] R. Banerjee, P.C. Collins, D. Bhattacharyya, S. Banerjee, H.L. Fraser, Microstructural evolution in laser deposited compositionally graded alpha/beta titanium-vanadium alloys, Acta Mat. 51 (11) (2003) 3277e3292.

[27] P.C. Collins, R. Banerjee, S. Banerjee, H.L. Fraser, Laser deposition of compositionally graded titanium-vanadium and titanium-molybdenum alloys, Mat. Sci. Eng. A 352 (1e2) (Jul. 2003) 118e128.

[28] T. Qian, D. Liu, X. Tian, C. Liu, H. Wang, Microstructure of TA2/TA15 graded structural material by laser additive manufacturing process, Trans. Nonferrous Met. Soc. China 24 (9) (2014) 2729e2736.

[29] H.S. Ren, D. Liu, H.B. Tang, X.J. Tian, Y.Y. Zhu, H.M. Wang, Microstructure and mechanical properties of a graded structural material, Mat. Sci. Eng. A 611 (2014) 362e369.

[30] W Li, S Karnati, C Kriewall, F Liou, J Newkirk, KMB Taminger, WJ Seufzer, Fabrication and characterization of a functionally graded material from Ti-6Al-4V to SS316 by laser metal deposition, Additive Manufacturing 14, 95-104.

[31] W Li, F Liou, J Newkirk, KMB Taminger, WJ Seufzer, Investigation on Ti6Al4V-V-Cr-Fe-SS316 multi-layers metallic structure fabricated by laser 3D printing, Scientific reports 7 (1), 7977.

[32] Zhang, J., Zhang, Y.,Li, W., Karnati, S., Liou, F.and Newkirk, J. (2018), "Microstructure and properties of functionally graded materials Ti6Al4V/TiC fabricated by direct laser deposition", Rapid Prototyping Journal, Vol. 24 No. 4, pp. 677-687.

[33] Li, W., Liou, F., Newkirk, J. et al. Ti6Al4V/SS316 multi-metallic structure fabricated by laser 3D printing and thermodynamic modeling prediction. Int J Adv Manuf Technol 92, 4511–4523 (2017).

[34] M. Rombouts, G. Maes, M. Mertens, W. Hendrix, Laser metal deposition of inconel 625: microstructure and mechanical properties, J. Laser Appl. 24 (5) (2012) 052007.

[35] G.P. Dinda, A.K. Dasgupta, J. Mazumder, Laser aided direct metal deposition of inconel 625 superalloy: microstructural evolution and thermal stability, Mat. Sci. Eng. A 509 (1e2) (2009) 98e104.

[36] K. Shah, A. Khan, S. Ali, M. Khan, A.J. Pinkerton, Parametric study of development of inconel-steel functionally graded materials by laser direct metal deposition, Mat. Des. 54 (2014) 531e538.

[37] Xinchang Zhang, Yitao Chen, Tan Pan, Wenyuan Cui, Lan Li, Frank Liou. (2019), Joining of copper and stainless steel 304L using direct metal deposition. Solid Freeform Fabrication, Vol. 6061, pp. 1068-1081.

[38] Imran MK, Masood SH, Brandt M, et al (2011) Direct metal deposition (DMD) of H13 tool steel on copper alloy substrate: Evaluation of mechanical properties. Mater Sci Eng A 528:3342–3349.

[39] Z. Sun, R. Karppi, The application of electron beam welding for the joining of dissimilar metals: an overview, J. Mat. Process. Technol. 59 (3) (1996) 257e267. SPEC. ISS.

[40] M. Megahed, H.-W. Mindt, N. N'Dri, H. Duan, O. Desmaison, Metal additive manufacturing process and residual stress modeling, Integrat. Mater. Manuf. Innov. 5 (2016) 1–33.

[41] P. Peyre, P. Aubry, R. Fabbro, R. Neveu, A. Longuet, Analytical and numerical modelling of the direct metal deposition laser process, J. Phys. D Appl. Phys. 41(2018)025403.

[42] Jeff Irwin, P. Michaleris, A Line Heat Input Model for Additive Manufacturing, J. Manuf. Sci. Eng 138(11), 111004 (Jun 23, 2016).

[43] L. Papadakis, A. Loizou, J. Risse, S. Bremen, J. Schrage, a computational reduction model for appraising structural effects in selective laser melting manufacturing: a methodical model reduction proposed for time-efficient finite element analysis of larger components in selective laser melting, Virtual Phys. Prototype. 9 (2014)17-25.

[44] Mills, K. C., 2002, Recommended Values of Thermophysical Properties for Selected Commercial Alloys, Woodhead Publishing.

[45] Dean Deng, Hidekazu Murakawa, Numerical simulation of temperature field and residual stress in multi-pass welds in stainless steel pipe and comparison with experimental measurements, Computational Materials Science, Volume 37, Issue 3, September 2006, Pages 269-277.

[46] Ladani, L., Romano, J., Brindley, W., and Burlatsky, S., 2017, "Effective liquid conductivity for improved simulation of thermal transport in laser beam melting powder bed technology," Add. Man., 14, pp. 13–23.

[47] Li, L., Lough, C., Replogle, A., Bristow, D., Landers, R., & Kinzel, E. (2017), Thermal Modeling of 304L Stainless Steel Selective Laser Melting. Solid Freeform Fabrication, Vol. 6061, pp. 1068-1081.

[48] ANSYS Theory Manual, Release 8.1, ANSYS Inc., USA, 2004.

[49] Ole Sigmund, Notes and Exercises for the Course:FEM-Heavy (41525), Technical University of Denmark, 2011.

[50] https://www.metallographic.com/Metallographic-Preparation-Procedures/Stainless-Copper-Weld.html

[51] Kar, Jyotirmaya, Sanat Kumar Roy, and Gour Gopal Roy. "Effect of beam oscillation on electron beam welding of copper with AISI-304 stainless steel." Journal of Materials Processing Technology 233 (2016): 174-185.

[52] C. Wallis, B. Buchmayr, M. Kitzmantel, E. Brandstätter, ADDITIVE MANUFACTURING OF MARAGING STEEL ON A COPPER SUBSTRATE USING SELECTIVE LASER MELTING, 2016.

[53] Prevey, Paul S. "X-ray diffraction residual stress techniques." ASM International, ASM Handbook. 10 (1986): 380-392.

III. RECONSTRUCTION ALGORITHM IN LASER-AIDED DIRECT METAL DEPOSITION REPAIR OF DAMAGED GEAR

Lan Li, Xinchang Zhang, Tan Pan, Frank Liou

Department of Mechanical and Aerospace Engineering, Missouri University of Science and Technology, Rolla, MO 65409

ABSTRACT

The objective of this work is to propose an advanced automated damage detection and damage reconstruction algorithm for a damaged gear tooth repair. It can automate tool path design and provides precise repair volume detection for more complex repair volume. First, models of the damaged part and nominal part were obtained. Next, the damaged model was aligned with the nominal model. After that, both models were sliced into layers, and a set of parallel and equidistant casting rays were used to intersect with these layers to extract the repair volume. Then the repair tool path was generated and used to guide the laser additive manufacturing process for repair. SS304L powder particles were deposited on the damaged region using the laser-aided direct metal deposition (LDMD) process. Microstructure analysis and Vickers hardness test were carried out to evaluate the repaired part quality. The repair experiment confirmed strong efficiency for this repair algorithm. A 3D finite element model was also developed to simulate the repair process and provide critical deformation and residual stress of the repaired parts. The predicted temperature and residual stress results were compared and showed a good agreement with the experimental measurements. These results further

validated that the proposed repair algorithm is suitable and efficient for the automated repair of the damaged components.

1. INTRODUCTION

Metallic components are critical elements in all mechanical systems. For instance, aero-engines consist of compressors, combustors, turbines, nozzles, etc., which are all made of metallic materials such as Ti-6Al-4V and nickel-based alloys [1]. Transmissions contain a complex series of gears, clutches, etc. that are made of high-strength steel or nickel alloys [2]. These metallic parts form the most important section in mechanical systems and their life directly affect the reliability of these systems. However, many metallic components usually work in a harsh environment. For example, aero-engine turbine blades often work at an elevated temperature and pressure environment and have a high likelihood of impact with foreign objects such as rocks [3]. Gears are generally subjected to heavy loading, high temperature, and wear. The harsh working environment can easily damage these parts prematurely, resulting in many types of defects such as creep damage, erosion, and fracture [4]. Unfortunately, most critical metallic parts are made of high-performance materials such as Ti- or Ni-alloys, and they are costly due to the difficult and complex manufacturing processes. Therefore, when they are damaged, discarding them and replacing them with new parts will cost significantly. A cost-efficient alternative is to repair them and put them back to service after complete inspection [5][6][7]. Repair damaged components can considerably extend their life and

also avoids interruption in the production process, especially for the parts that the replacement is no longer available.

Among the additive techniques, the laser-aided direct metal deposition (LDMD) process has emerged recently and has shown great applications in the field of repair [8][9]. The advantages of LDMD make it suitable for repair. For example, LDMD introduces low heat and can cause less distortion of the base part, which is perfect for dimensional-delicate thin-wall structures. In addition, LDMD can realize the fabrication of full-dense parts with high strength. In the LDMD process, a concentrated high-energy laser is used to create a melt pool on the damaged zone, and in the meantime, incoming metal powders are delivered into the melt pool and undergo melting and solidification to form a layer. Because the substrate material was melted and mixed with the incoming material, an excellent bond can be achieved [10][11].

Reconstructing the repair volume following tool path is essential for remanufacturing since it provides the geometry that needs to be precisely recreated on the damaged region. Several researchers have studied the LDMD process for component repair. Pinkerton et al. [12] made two different geometries on H13 hot-work tool steel substrates and restored the damaged area with H13 powders with high-quality. Wilson et al. [13] employed the LDMD process to restore a damaged turbine blade and then validate the strength of the repair by tensile tests. LDMD processes can also process other materials to repair missing volumes including Ti-6Al-4V [14][15][16] and stainless steel [17]. However, the repair objects in the aforementioned studies were very simple and geometric regular since the repair volumes were very easy to predict. In this scenario, it is able to generate a tool path manually. However, in most real situations, the repair volume

is very complex and unique, which requires numerous amounts of time to manually define the tool path. In addition, operator's experience-based damage reconstruction cannot guarantee consistent and repeatable repair quality. Both factors dramatically increase the risk of failure during service. Therefore, an automated damage reconstruction strategy is required, which guarantees time saving and precise part repair. In previous studies [18][19][20], we proposed a reverse engineering algorithm to reconstruct fracture surface on the damaged model and cut the nominal model to restore the missing volume on compressor blade or a damaged die. These experiments were on good evaluation for the automated repair process. However, this process limits fast repair due to inefficient scanning points on damaged surfaces, especially for complicated gear geometry and tooth fracture surface. Therefore, developing a high-efficient damage reconstruction strategy by assuring good deposits is urgently needed in modern repair workshops. Here gives the objective of this study. The advanced automated damage detection and reconstruction algorithm for much more scanning points was proposed in this study for component repair of complicated gear with one tooth fracture.

In this work, a reconstruction algorithm was proposed to automatically restore the missing geometry with SS304L powder on a damaged gear that was made of iron. In Section 2, three steps are elucidated to design the tool path. Firstly, the damaged gear model was compared with the nominal model. Secondly, missing geometry was obtained by slicing the required volume into several layers. Finally, the tool path was generated. In Section 3, laser scanning tracks in eight layers were generated according to the extracted geometry and appropriate LDMD process parameters. SS304L powder particles were deposited on the damaged region performed with the LDMD process. Microstructure

analysis and Vickers hardness test were carried out to evaluate the repaired part quality. In Section 4 and 5, based on the repair volume and scanning layers, thermo-mechanical numerical model was developed to accurately predict the deformation and stress behavior of the repair process. Finally, conclusions were drawn about this advanced automated damage detection and reconstruction method.

2. MODEL ALIGNMENT AND REPAIR VOLUME RECONSTRUCTION STRATEGIES

A Module M=2 with 20 teeth gear was used to exemplify the damage reconstruction process. The nominal part is firstly scanned to construct the nominal model. After that, a defect was created on one tooth using Hansvedt wire electric discharge machining (EDM) system. Figure 1 depicts the nominal and damaged models of the gear part. For the damaged gear, damage generated in one tooth area. For repairing the damaged gear, it is crucial to reobtain the geometry of the missing tooth since the tool path in the DMD process is generated according to the missing geometry. In the real repairing process, the model of the damaged part was generally obtained using reverse engineering-based tools such as coordinate measuring machines (CMM) or 3D scanner. Laser scanner or structured-light scanner can reconstruct the 3D model of an existing object very rapidly and with high accuracy, and therefore, are widely used in repair applications. Researchers reported that 3D scanned damaged models were skewed from the nominal models. It is because the separate scanning process of nominal and damaged models disarranges the position of both models. It is of considerable importance to align the damaged model with the nominal model for the purpose of reconstructing the missing

volume. For mimicking the disorder of both models, the damaged model shown in Figure 1(b) was rotated around x, y, and z axis with random angles. This results in the arbitrary position of both models as illustrated in Figure 1(c). An algorithm was proposed to generate the transformation matrix to align both models together.

The model alignment was carried out in the following sequence. The first step, called surface alignment, was to align the side surfaces of both models. The normal vectors of the side surfaces of both models were searched and then the transformation matrix was calculated to ensure coincidence of both normal vectors. As an example, the normal vector of the target surface of the nominal model is $n_n = (x_n, y_n, z_n)$ and the normal vector of the damaged model is $n_d = (x_d, y_d, z_d)$, shown in Figure 1(c). The objective was to obtain the transformation matrix T so that $n_d \cdot T = n_n$. The transformation matrix T was obtained through Rodrigues' rotation formula. After this step, the relative position and orientation of both models are shown in Figure 1(d). It is obvious from Figure 1(d) that although the two side surfaces were aligned, both models were not fully aligned. In the second step, called convex-hull centroid alignment, both nominal and damaged models were sliced into a number of layers as shown in Figure 1(e). It should be noted that, because a broken tooth was on the damaged model, the convex-hull centroids of the outer profile of the damaged model cannot be used for alignment purposes. This is because the damaged tooth will shift the convex-hull centroids. However, since the inner hole on the damaged model is intact, the convex-hull centroids of the inner hole can be used for alignment. Based on the coordinates of the convex-hull centroids, a translation vector can be obtained to translate the damaged model to the position as shown in Figure 1(f). Figure 1(g) shows a cross-section from the

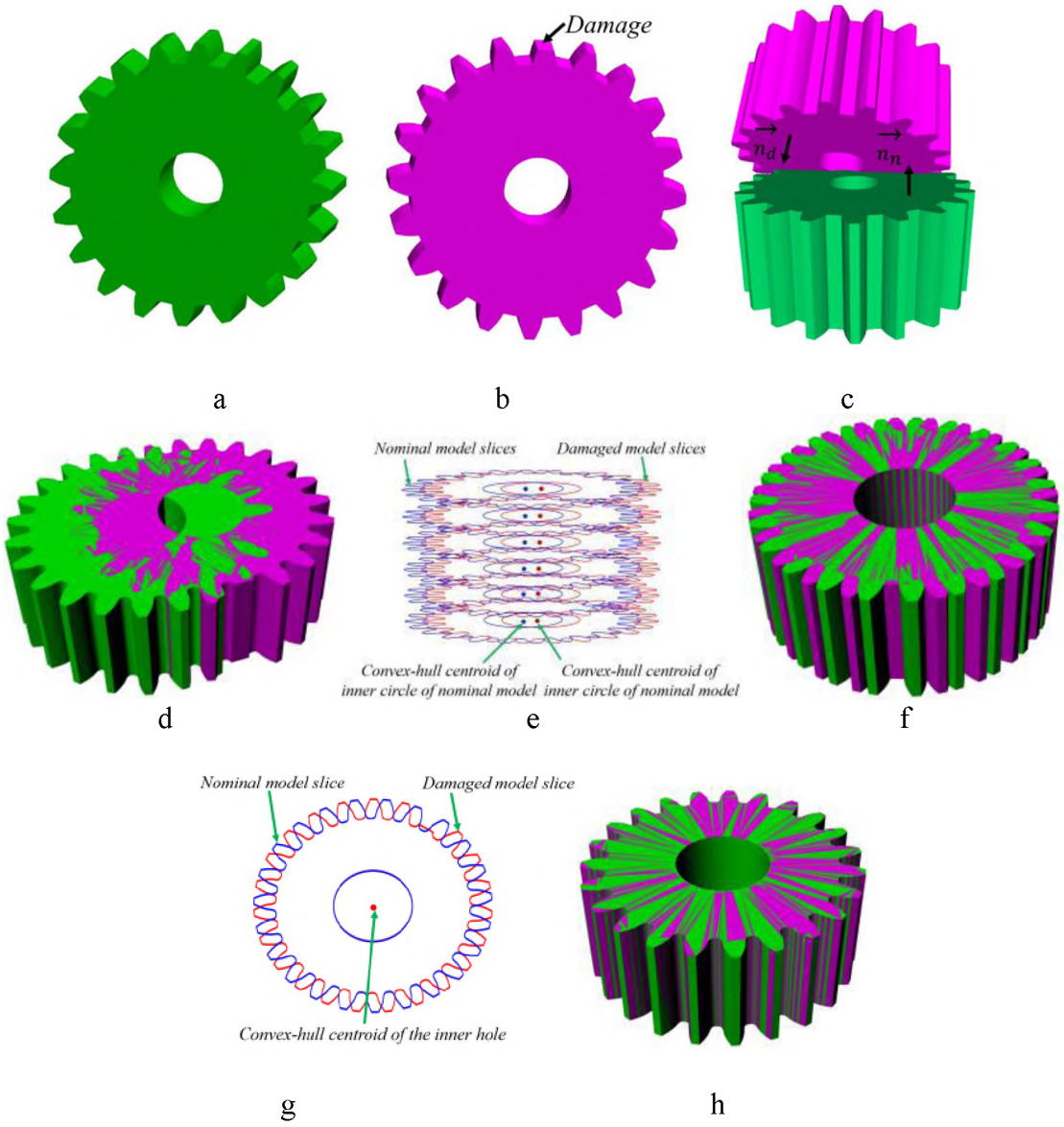

Figure 1. Nominal (a) and damaged (b) model of the gear; (c) Nominal and damaged models in unaligned condition; (d) Models after surface alignment; (e) Cross-sections and convex-hull centroid of inner hole for nominal and damaged models; (f) Models after convex-hull centroid alignment; (g) A slice from nominal and damaged models; (h) Fully aligned model.

nominal and damaged models after convex-hull centroid alignment. It shows the damaged model is still not aligned with the nominal model. By rotating the damaged model around the convex-hull centroid, the damaged model can be eventually aligned

with the nominal model. The target is to obtain the rotary angle that the damaged model should perform. The optimal rotary angle was obtained by maximizing the overlapping area of the two cross-sections as shown in Figure 1(g). Figure 1(h) illustrates the finally aligned models.

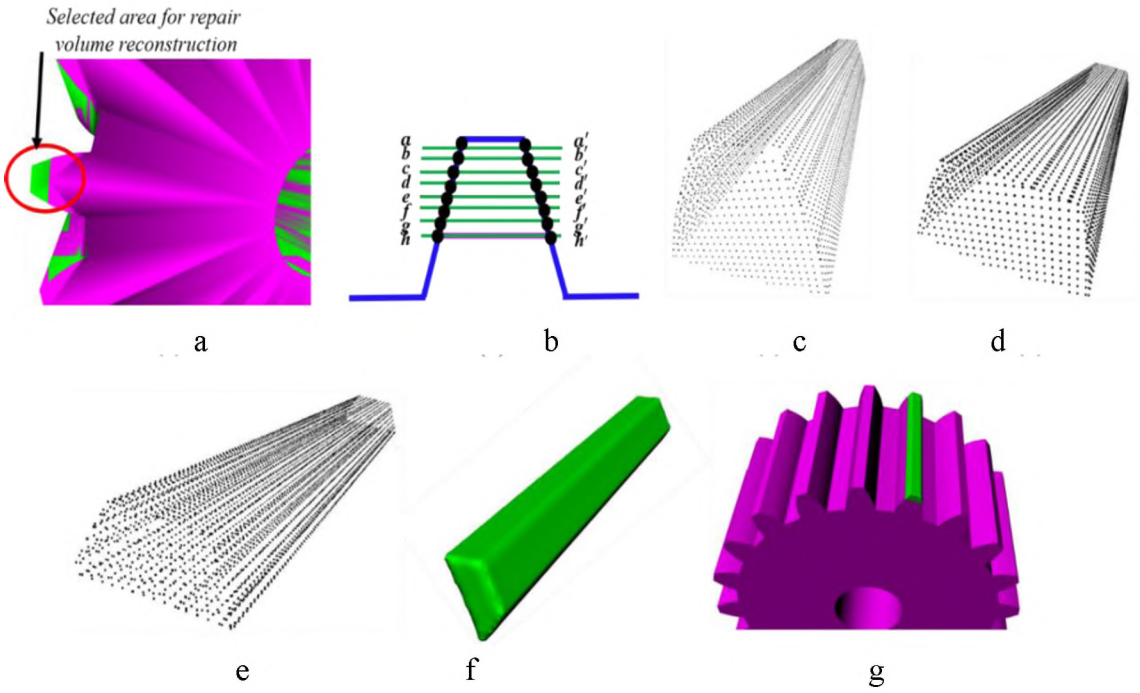

Figure 2. Repair volume reconstruction. (a) Selected area for repair volume reconstruction; (b) Schematic diagram showing the repair volume reconstruction strategy; (c) Intersections of casting rays with nominal model; (d) Intersections of casting rays with damaged model; (e) Extract point set forming repair volume; (f) Reconstructed STL model of the repair volume; (g) Repair volume positioned on damaged model.

After model alignment, repair volume reconstruction was conducted to reobtain the missing geometry. For such purpose, an area covering the damage was selected as shown in Figure 2(a). After that, casting rays in three directions (x, y, and z) were injected to intersect both models. Such casting rays intersected with the selected area of

the nominal model and the damaged model and the intersections are shown in Figure 2(c) and 2(d), respectively. The intersections forming the repair volume were obtained as follows. As shown in Figure 2(b), the intersections of casting rays with the nominal model cross-section are $[a, a', b, b', c, c', d, d', e, e', f, f', g, g', h, h']$. For the damaged model, since there is a missing geometry, the intersections are $[h, h']$. Therefore, it can be seen that $[a, a', b, b', c, c', d, d', e, e', f, f', g, g']$ are missing from the damaged model and should be reconstructed. Using this strategy, the missing points were obtained as shown in Figure 2(e). Such point data were further processed to generate the STL model as shown in Figure 2(f). The reconstructed repair volume was positioned on the damaged model to test the accuracy as shown in Figure 2(g), which confirms that the missing geometry has been successfully restored.

3. GEAR REPAIR EXPERIMENT AND RESULTS

3.1. EXPERIMENT PROCEDURE AND MATERIALS PREPARATION

In this study, the LDMD system (Figure 3a-d) consists of a laser nozzle system with a maximum power of 1000 W, a blown powder feeding system, and a 3-axis CNC work table to realize the relative movement between the substrate and the laser beam. The maximum laser beam diameter is 2 mm. Argon shielding gas is inserted to preclude material oxidization.

Recall that automated damage detection and reconstruction algorithms were completed for the damaged gear in Section 2. In this step, the missing geometry in the damaged gear was separated into eight layers. Considering a total thickness of 2 mm,

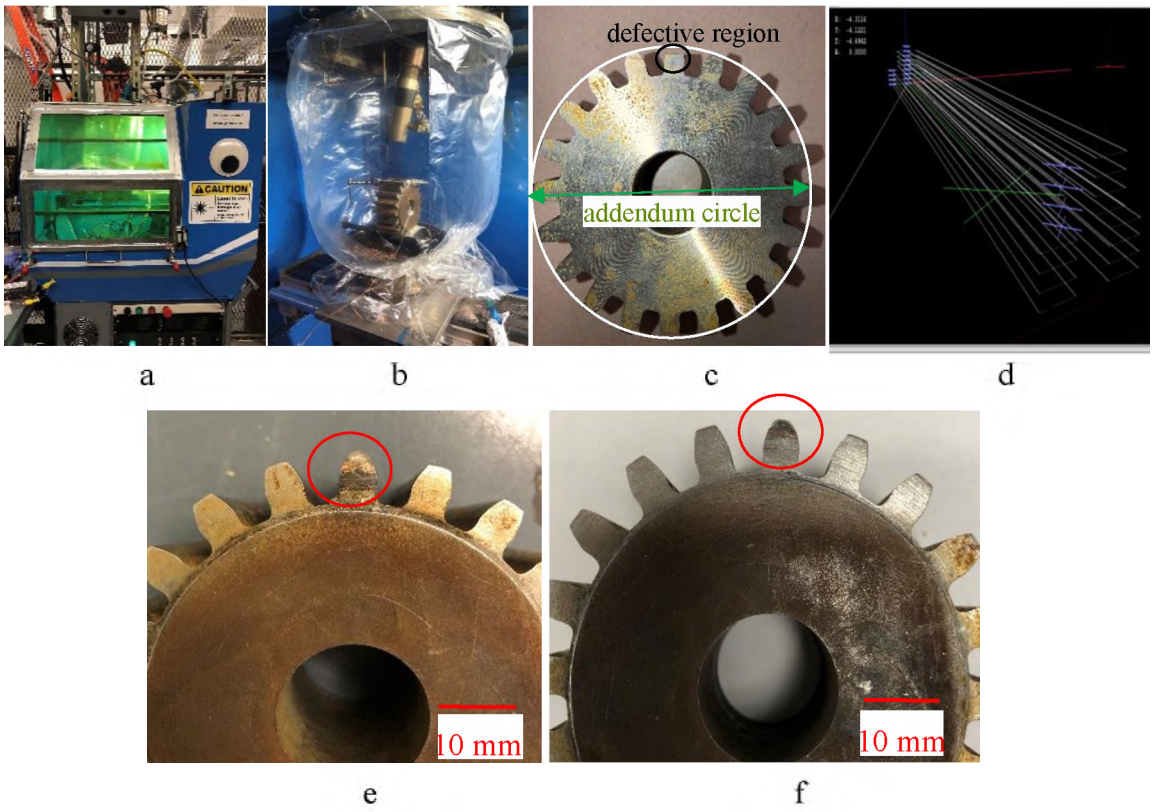

Figure 3. DMD equipment to perform repair experiment. (a) DMD system chamber; (b) DMD experimental set-up; (c) Damaged gear; (d) Tool path generation for material deposition; (e) Gear after DMD process; (f) Gear after machining.

Table 1. Processing parameters for repair experiment.

Experiment parameters	Values
Power, P [W]	850
Powder flow rate, [g/min]	2.8
Scan speed, [mm/min]	210
Laser diameter, d [mm]	1.3
Layer thickness, [mm]	0.25
Number of laser tracks, N	28

each layer was planned for a thickness of 0.25 mm. An outline contour with a zigzag infill pattern was used in this study. That is, laser scans along the z-axis and then follows a zigzag pattern. The tool path was referred to by the extracted points in Figure 3d. The processing parameters were listed in Table 1. The damaged area was firstly cleaned with acetone and then deposited by SS304L powder particles. The experimental powder of SS304L alloy had a spherical shape and the particle diameter is in the range of 25 ~ 100 μm.

3.2. SAMPLE PREPARATION

Figure 3e and 3f show the gear after metal deposition and post-machining. Even for this complex repair volume, post-machining amount of time from this automated define tool path is much less than paper [20]. It can guarantee consistent and repeatable damage reconstruction. Thus, dramatically decrease the risk of failure during service. Therefore, this automated damage reconstruction strategy is time saving. The microstructure analysis of the as-deposited SS304L around the bounding area was conducted to assess the repair quality. After fabrication, the specimen was cut, polished, and then etched with 60/40 Nitric Acid, and finally captured using HIRO KH-8700 digital optical microscope and a scanning electron microscopy (SEM, FEI Quanta 250 FEG).

3.3. MICROSTRUCTURE EVALUATION

Micrographs were taken at three different cross-sections of the repaired samples: near the bonding area (Figure 4a), the deposits near the bonding area (Figure 4b), and the

deposits on the as-deposited top site (Figure 4c). It was noticed that the bonding interface between the deposited material and the substrate was very clear. Fabrication defects such as delamination, pores, and cracks were not detected on the bonding interface. Good metallurgical bonding at the interface was further confirmed by microstructure analysis. It was noticed that columnar dendrites arrange normal to the layer band interface since this is towards the maximum temperature gradient. As can be seen from Figure 4b and 4c, a large columnar microstructure was observed right above the interface and in the heat-affected zone (HAZ). This is due to the deposit process that the substrate material near the interface was melted with the delivered SS304L and then subsequently re-solidified by the successive depositing layers. Some cellular structures were also noticed in such regions. The result of cellular grain structure in this sample was consistent throughout the built samples. The cellular grain structure seen in these micrographs and further identified by Figure 4c confirmed the fast cooling rate of a cellular solidification structure. The microstructure of the top zone mainly consists of clusters of cells, as shown in Figure 4c.

3.4. VICKERS HARDNESS ANALYSIS

The hardness measurement was performed on the cross-section of the repaired sample from deposits to substrate using a Struers Duramin 5 microhardness tester. Figure 4d plotted the hardness distribution at different locations of three samples. Indentions started at the substrate region and continued at various spacing into the SS304L region. the interval between two indentations was set to 0.5 mm. It was found that all VHN gradients were slight instead of steep changes. The hardness on the deposit side is higher

than that of annealed iron substrate sides, which had relatively constant hardness values between 180 HV and 230 HV. It was also found that the hardness of deposits decreased slightly as the deposition layer increased. This was attributable to the high cooling rate during the deposition and fine microstructure on deposits. Thus, the hardness at as- deposited material near the interface was slightly higher than that away from the interface.

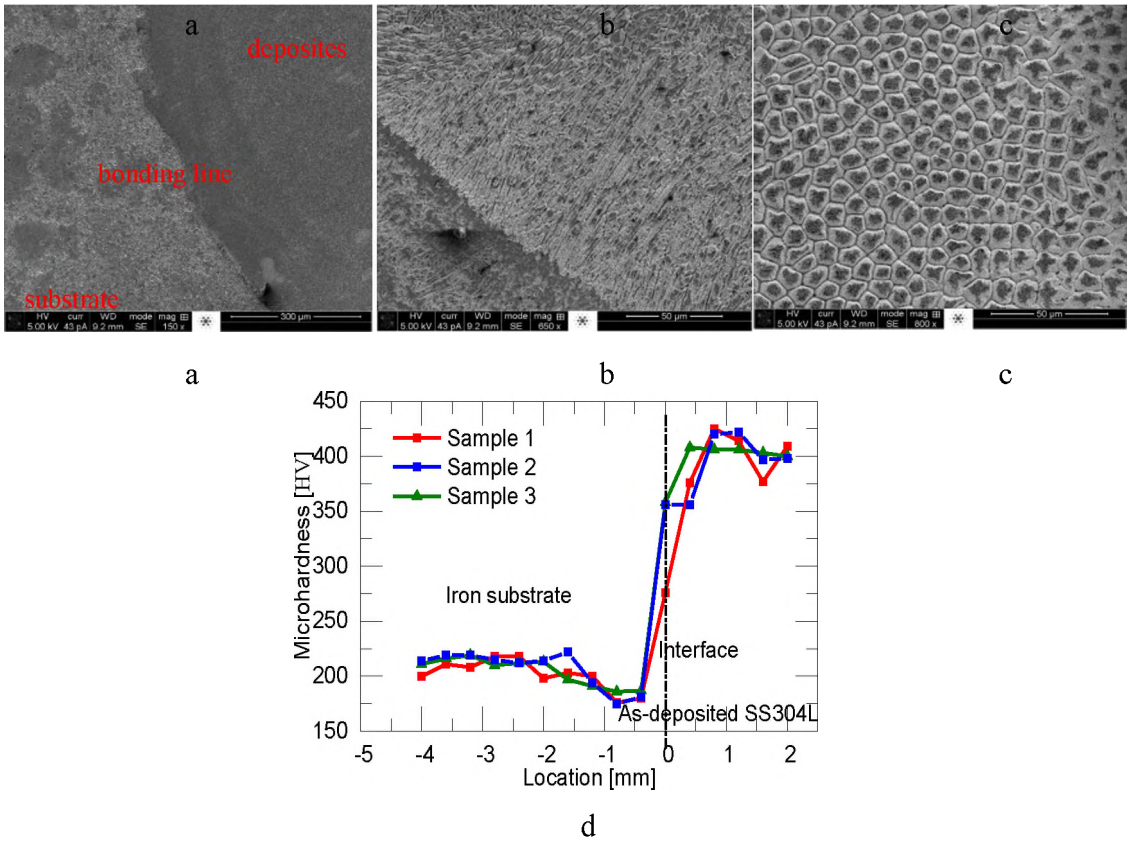

Figure 4. (a) Optical micrographs on cross-section of materials on the bonding area; (b) Microstructure on deposites near the bonding area; (c) Microstructure on deposites faw away the bonding area; (d) Vickers hardness distribution.

4. NUMERICAL ANALYSIS OF THE LASER REPAIR PROCESS

During the additive manufacturing process, significant thermal residual stresses and distortion can be induced by moving high-intensity laser. High thermal residual stress is a critical issue since it is likely to cause distortion, cracking, and fatigue failure, and hence impacts the quality of the repaired product. The deformation and stress distribution in the additive manufacturing process can be simulated by finite element method (FEA) with specified material properties and boundary conditions. Commercial FEA softwares like ABAQUS®, COMSOL Multiphysics® and ANSYS® can be used to optimize design parameters to meet specific performance [21-28]. Therefore, it is necessary to track the residual stress evolution during and after the repair in order to achieve successful part printing for complex 3D components.

4.1. MODEL SETUP

The aim of FEA modeling in this section is to calculate residual stress and deformation distribution in the repaired sample. A 3D coupled thermo-mechanical model was developed by ANSYS® Mechanical APDL to simulate the LDMD process of the gear repair in which the temperature history and residual stress can be instantly monitored. In this commercial software, the energy input, material deposition, deposition rate, substrate preheating, and tool paths during the deposition process are implemented by user subroutine in APDL. In the model, the transient heat transfer analysis was firstly run to obtain temperature distribution. Then, the structural analysis was implemented to calculate thermal stress and distortion.

Figure 5a shows the geometry of damaged gear as modeling domain. The intact section with the damaged tooth is shown in Figure 5b and 5c. 28 tracks were planned for the total LDMD process. The laser traversed at a speed of 210 mm/min. In material deposition process, the continuously adding elements is implemented by birth- and-death function in ANSYS® to activate an element. This element activation method is widely used in modeling material deposition in AM process. Figure 5d and 5e show

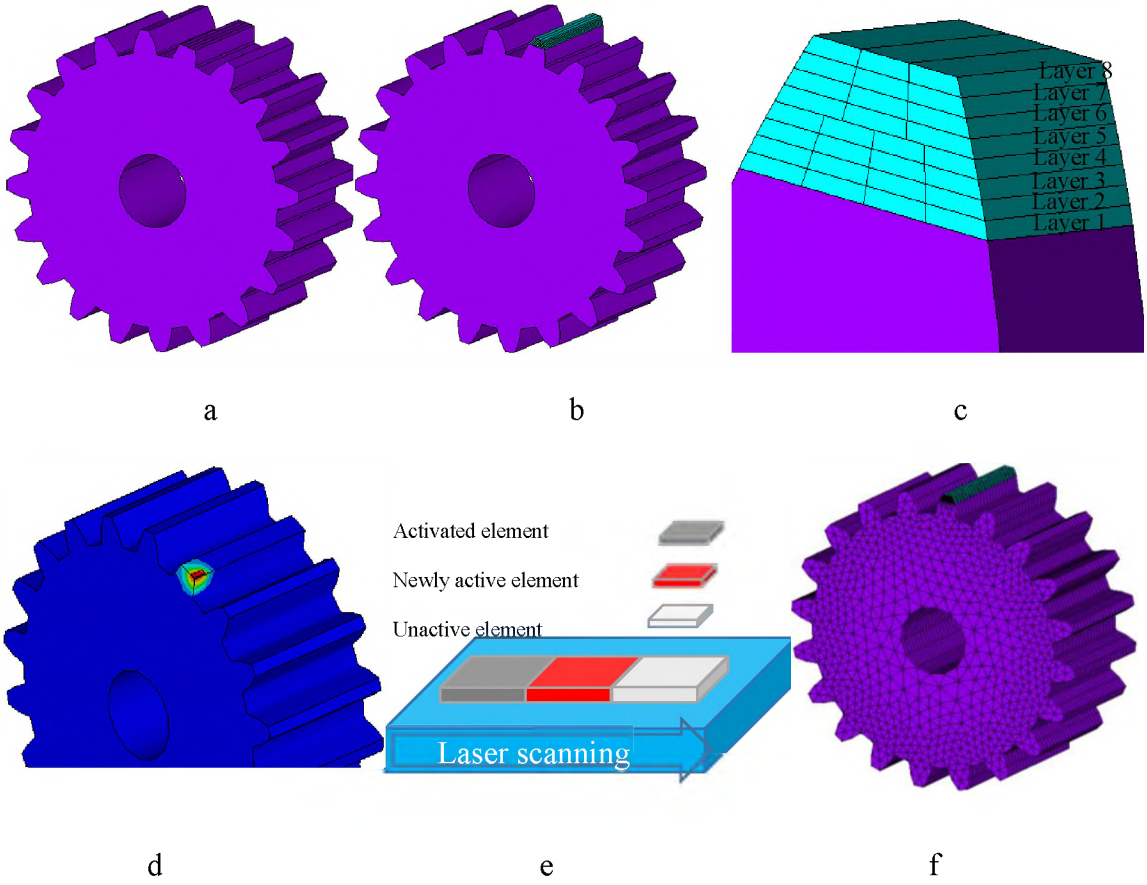

Figure 5. (a) FEA model geometry of the damaged gear; (b) Laser scan strategy of 4 tracks of repair volume; (c) A zoomed-in view of the repair with deposit track; (d) FEA model of the first deposition of the damaged gear; (e) Schematic of element birth and death function; (f) Finite element mesh for DMD process simulation.

material addition during the LDMD process by the element birth and death function. At initial state, just the substrate elements were all activated. The element with 0.25 mm thickness for new material addition was activated sequentially in the laser scanning direction to simulate the material addition process. Other processing parameters are the same as the lase repair experiment. To reduce the computational cost, the deposited elements use hexahedral mesh with 0.5 mm, and the gear base part was coarsely meshed. The final model contained a total of 56650 elements and 43993 nodes. The finite element mesh for the LDMD process simulation is shown in Figure 5f.

4.2. GOVERNING EQUATION FOR THERMO-MECHANICAL ANALYSIS

Transient energy equation is used as the governing equation for heat transfer in the entire volume of the material, given as

$$\rho c_p(T)\frac{\partial T}{\partial t} = \frac{\partial}{\partial x}\left[k(T)\frac{\partial T}{\partial x}\right] + \frac{\partial}{\partial y}\left[k(T)\frac{\partial T}{\partial y}\right] + \frac{\partial}{\partial z}\left[k(T)\frac{\partial T}{\partial z}\right] + \dot{q} \tag{1}$$

where T is the current temperature, $k(T)$ is the temperature-dependent thermal conductivity, $c_p(T)$ is the temperature-dependent specific heat, ρ is the constant density, $\dot{q}$ represents heat sink or source in the volume, t is the time, x, y and z are the coordinates in the reference system as the same as X, Y, Z in graphs.

Stress equilibrium equation is used as the governing equation for mechanical analysis [29][30]:

$$\nabla \cdot \sigma = 0 \tag{2}$$

where σ is the second-order stress tensor associated with the material behavior law.

The isotropic Hooke's law is used to relate stress and elastic strain as:

$$\sigma = C\varepsilon^{e} \tag{3}$$

where ε^{e} is the second-order elastic strain tensor and C is the fourth-order material stiffness tensor.

Thermo-elasto-plasticity is considered in the deposition process. Therefore, the total strain ε has three components [31]:

$$\varepsilon = \varepsilon^{th} + \varepsilon^{p} + \varepsilon^{e} \tag{4}$$

$$\varepsilon^{th} = \alpha \cdot \triangle T \tag{5}$$

where ε^{th}, ε^{p} and ε^{e} are the thermal strain, plastic strain, and elastic strain, respectively, α is the coefficient of thermal expansion and ΔT is the temperature difference with respect to reference temperature. The thermal strain is calculated by equation (5). Elastic and plastic stain in our study is calculated by bilinear isotropic hardening model, which is defined by elastic modulus E, Poisson's ratio v, yield strength σ_Y, and tangent modulus G [32][33].

4.3. MODELING OF THE HEAT SOURCE

In experiments, the laser beam heats up the layered material in circular influencing region. In the simulation, this heating process is represented as volume heat flux on active element of powder. Because of the small dimension in powder depth direction, the power density in depth direction was considered constant. The heat flux obeys Gaussian distribution on the *x*-*y* plane which follows as:

$$\dot{q} = \frac{2\phi P}{\pi r_0^2} \exp\left[-2\frac{r^2}{r_0^2}\right] \tag{6}$$

where ϕ is the laser absorptivity, $\phi = 0.3$ in this work. r_0 is the radius of laser beam and

P is the laser power, Eq. (6) shows that heat flux exponentially decays away from the laser beam center in x-y plane.

4.4. BOUNDARY CONDITIONS

Before the laser heating, atmospheric temperature is set as the initial temperature condition. The substrate follows the uniform temperature distribution:

$$T(x, y, z, t)_{t=0} = T_0 = T_a \tag{7}$$

where T_a is the ambient temperature equals to the initial temperature T_0, set as 25 ℃.

All external surfaces of deposited layer are exposed to atmosphere and are subjected to heat convection with air and heat radiation. These two factors dissipate thermal energy into atmosphere and are necessarily considered in this study. The corresponding boundary conditions for external surfaces are:

$$q_c = h\left(T - T_a\right) \tag{8}$$

$$q_r = \varepsilon_r \sigma_r \left(T^4 - T_a^4\right) \tag{9}$$

where h is the heat transfer coefficient of natural thermal convection, which is assumed to 50 W/m^2·℃, σ_r is the Stefan–Boltzmann constant setting as 5.67 × 10^{-8} W/m^2·K^4 and ε_r is the material emissivity setting as 0.3. Base plate underneath the substrate can absorb heat rapidly in the laser deposition process and maintain at ambient temperature. Therefore, in the simulation, flux boundary is set for the substrate base surface as Eq. (8). By fitting simulated and experimental results, the heat transfer coefficient used for Newton's model is set to 100 W/m^2·℃. In the structural analysis, the internal surface of the gear is set to

Table 2. Thermo-mechanical properties of the stainless steel 304L substrate.

Temperature (°C)	25	100	200	300	400	600	800	1200	1300	1500
Density, (kg/m3)	7900	7880	7830	7790	7750	7660	7560	7370	7320	7320
Thermal conductivity, (W/(mK))	14.6	15.1	16.1	17.9	18	20.8	23.9	32.2	33.7	120
Specific heat, (J/(kgK))	462	496	512	525	540	577	604	676	692	720
Thermal expansion coefficient, (10^{-6}/K)	17	17.4	18	18.6	19	19.6	20	20.7	21.1	21.6
Poisson's ratio	0.29	0.295	0.3	0.31	0.32	0.33	0.34	0.34	0.35	0.39
Elastic modulus, (GPa)	198	193	185	176	167	159	151	60	20	10
Yield strength, (MPa)	265	218	186	170	155	149	91	25	21	10

Table 3. Thermo-mechanical properties of the iron substrate.

Temperature (°C)	25	100	200	300	400	600	800	1200	1300	1500
Density, (kg/m3)	7874	7849	7815	7781	7747	7679	7612	7503	7452	7366
Thermal conductivity (W/(mK))	73	68	61	55	49	39	30	35	37	36
Specific heat, (J/(kgK))	450	496	512	525	540	577	604	676	692	720
Thermal expansion coefficient, (10^{-6}/K)	15	15	15	15	15	15	15	15	15	15
Poisson's ratio	0.3	0.3	0.3	0.3	0.3	0.3	0.3	0.3	0.3	0.3
Elastic modulus, (GPa)	199	194	185	174	161	127	84	2	1	1
Yield strength, (MPa)	265	218	186	170	155	149	91	25	21	10

fixed boundary condition, i.e., the displacement of all nodes of the surface along the x, y, and z directions are zero.

4.5. THERMO-PHYSICAL AND MECHANICAL PROPERTIES

The thermo-physical properties and mechanical properties of SS304L were temperature-dependent and identified in [34][35], as shown in Tables 2-3.

5. SIMULATION RESULTS

5.1. TEMPERATURE VALIDATION WITH EXPERIMENT

Figure 6 shows the simulated temperature history at Point A and B where they are located at two end sides on the base substrate, 2 mm upon the tooth root, same location with the thermocouples of TC1 and TC2. The locations are shown in Figure 6a. The predicted temperature history has reheating and cooling stages during the deposition of all layer tracks. The temperature evolution in simulation and the experiments at thermocouples TC1 and TC2 during the actual manufacturing process are compared and presented in Figure 6b. It is observed that simulation has the same trend as the experimental measurement. Good agreement is achieved.

Figure 7a shows the temperature contour where the laser is applied to the end of the 1st track, followed by the 4^{th}, 16^{th}, and 28^{th} track in Figure 7b, 7c, and 7d. Because of the lower thermal conductivity within the small mass structure compared to the large support base, heat conduction from the heating area to the support base is considerably slower. This leads to higher temperature in the small heating area. Because of the zigzag

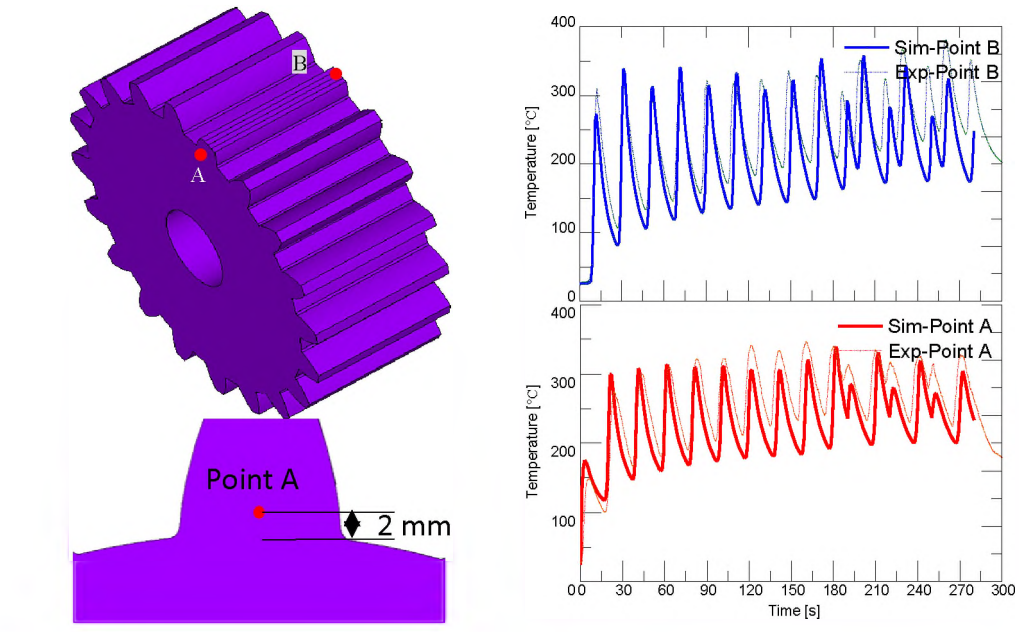

a b

Figure 6. (a) Location of Point A and B; (b) The simulated and measured temperature history during the deposition at each selected position, Point A and B.

infill pattern, the deposited track experiences an alternating sequence of heating and cooling. The transient temperature varies from the ambient temperature to a high temperature (even higher than melting temperature) and then cools down. The deposited wall has temperature variation from ambient temperature to 1846 ℃ in the first track. Measured from the zone in temperature contours, the depth of the area where the temperature was higher than the melting point is 0.55 mm. In Figure 7e, the zone encompassed by the grey color depicted the molten pool. It can be observed that the melting depth was deep enough to fully bond the first deposited layer and the base substrate. Because of thermal accumulation from previous deposition track, the highest temperature raised up to 1889 ℃ at the end of the 4th track in Figure 7b. Considerably higher temperatures are observed after the deposition of the last track, with the value of

1964 °C in the 28th track as seen in Figure 7d. Again, the melting depth of 0.7 mm makes fully metallurgical bonding in Figure 7f. This is because of the heat accumulation effect for additional layers of the successive deposition. In the LDMD process, when printing the upper layer, heat will transfer to the substrate, since the substrate acts as a heat sink in this situation. Therefore, when the deposited layer goes upper, the peak temperature of the upper layers increases.

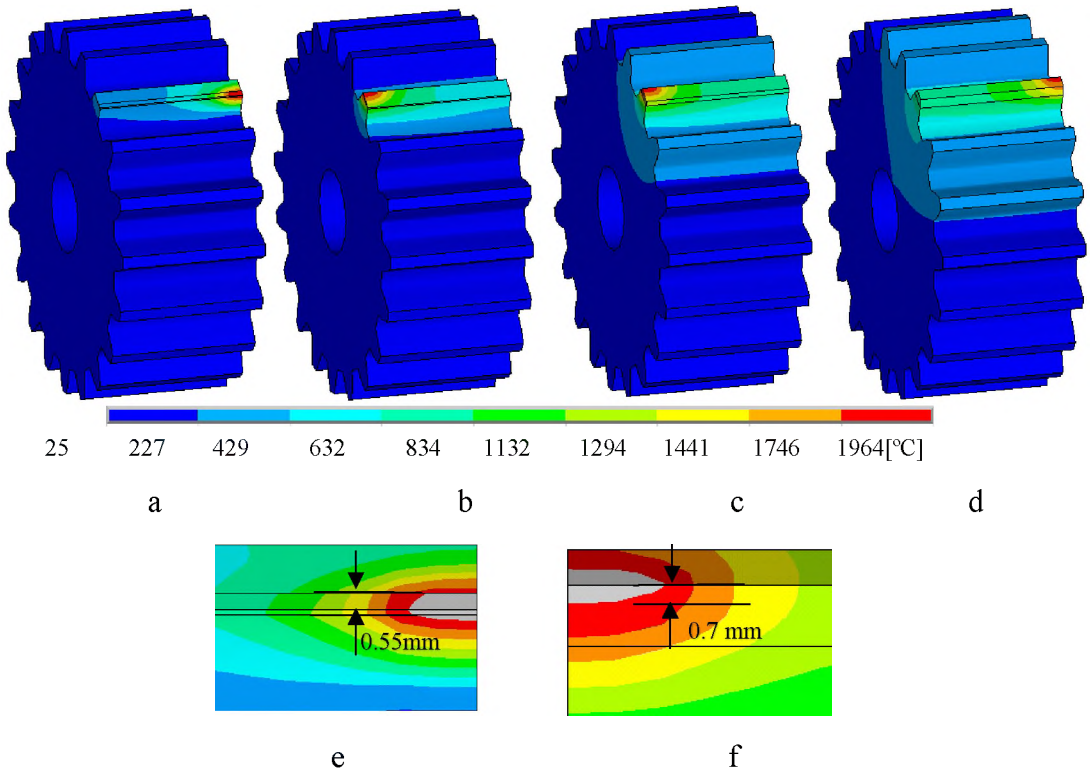

Figure 7. Temperature distribution at the middle of n^{th} track, n is 1 (a), 4 (b), 16 (c) and 28 (d); Zoom in of temperature contour at the end of 1^{st} in (e) and 28^{th} in (f) track to measure the melt pool depth.

5.2. RESIDUAL STRESS ANALYSIS IN SIMULATION

Laser melting trajectory can significantly affect the mechanical properties of deposits [36]. The back-and-forth laser traveling strategies imposed cyclic thermal heating and resulted in cyclic thermal stress. Thermal stress and deformation could be accumulated by the repeated thermal cycles in the material addition process and result in severe part distortions such as delamination and cracking [37]. Scanning parameters can also significantly affect the residual stress and deformation due to locally non-uniform laser heat. Poor path planning may create high residual stresses, gas pores, and distortion on deposits. High residual tensile stress, usually associated with the LDMD process, may cause cracking due to different thermal expansion coefficients between deposits and substrate [38]. Mechanical strain, plastic deformation, and high thermal stresses are important causes for gear damage. Thus, it is important to know the deformation and residual stress distribution of the gear during the repair process.

When all deposition completed and the component cooled down to ambient temperature, the displacement distributions are illustrated in Figure 8a-d. The displacement in the x-direction, y-direction (building up direction), z-direction (scanning direction), and total displacement vector are presented in sequence. The final displacement in the y-direction (building up direction) increases with increased layer numbers, and the peak value occurs at or near the free surface of the final deposited layer. This is shown in Figure 8b at the upper deposition region of the building part, with values of 0.035 mm, whereas the total displacement vector in Figure 8d has the maximum displacement value on top free surface of the final deposited layer. Subsequently, the residual stress distributions are illustrated in Figure 8e-h. The residual stress in the *x*-

direction, *y*-direction (building up direction), *z*-direction (scanning direction), and von Mises stress are presented in sequence. The *z*-component of tensile residual stress in Figure 8g has a value of 325 MPa near the top surface of the deposited layer, which is highest in all three directions. It is observed that residual stresses are larger along the scan direction than the perpendicular direction due to the larger thermal gradient along the scan direction. This can be explained by the fact that the latest melted and solidified material is subjected to the highest tensile stress when adding new materials. In this regard, the underneath parts are in compression caused by the cooling and contraction of the overlying new-molten material. The residual stress in the *x*- direction and *y*-direction (building up direction) implies that the residual stress profile is made up of large number of tensile stresses at the interface region of the deposits to the base part, whose value is up to 180MPa. This means the deposition strategy and track length also have a large influence on residual stress levels. It is well known that residual stress contributes to the crack formation in the part, which is not acceptable when printing the damaged part. Sometimes delamination of the supports at the intersection position can be observed in the printing field. High residual tensile stress could result in cracking due to different thermal expansion coefficients between deposits and substrate material. While in the current research, the average equivalent stresses show values of 165MPa at the interface section on the deposited tracks. That value is smaller than the yield stress of SS304L. The low equivalent stresses will not induce crack or delamination in repair case. Hence, this laser repairing task can be treated as successful. The thermo-mechanical FEA model further validated that the proposed repair algorithm is successful and efficient for the automated repair of the damaged gear.

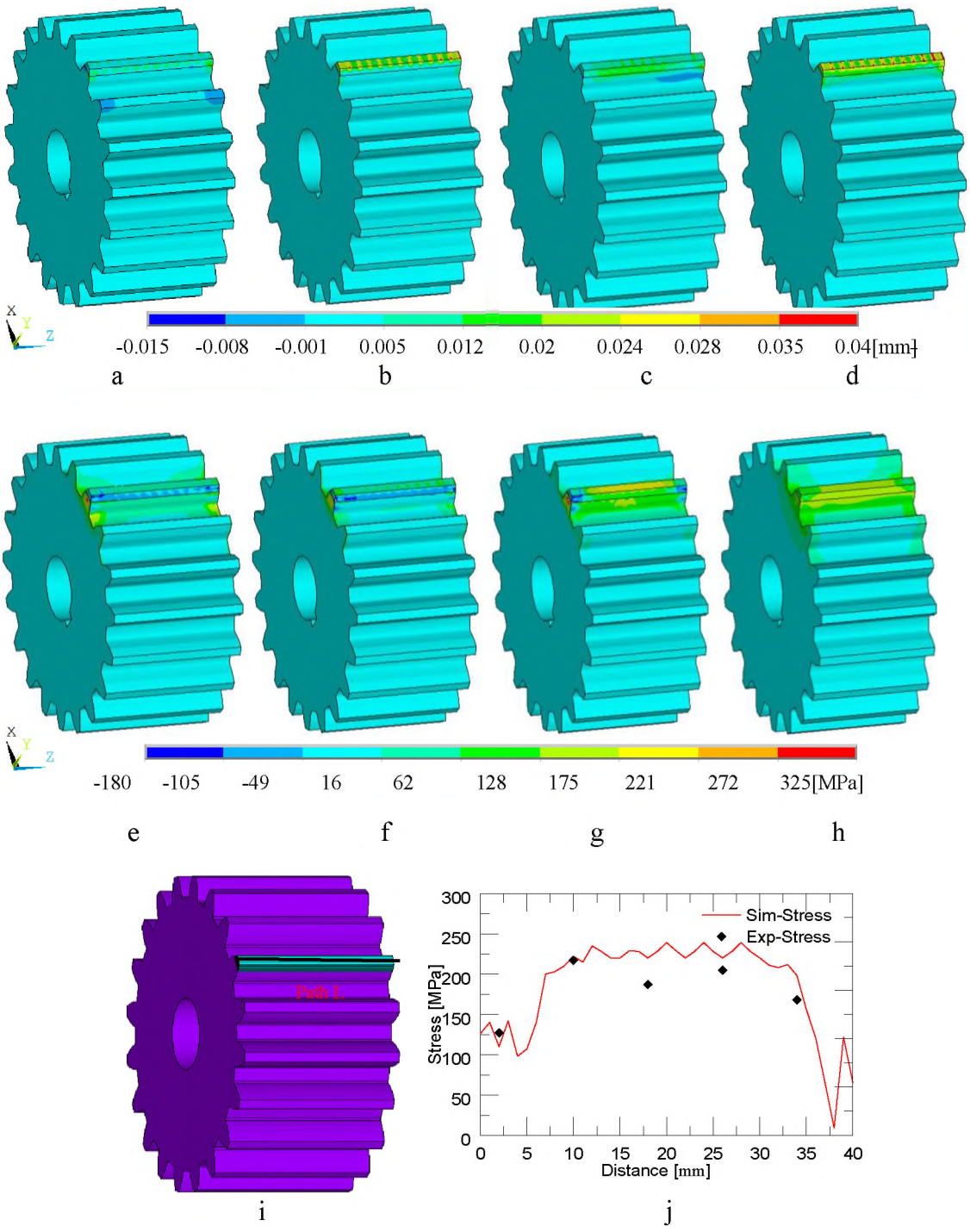

Figure 8. (a) Longitudinal displacement, Ux; (b) Transversal displacement, Uy; (c) Normal displacement, Uz; (d) Displacement vector sum, Usum; (e) Longitudinal stress, Sx; (f) Transversal stress, Sy; (g) Normal stress, Sz; (h) Von Mises stress, Seqv, after all deposition done until cooling to room temperature; (i) The monitoring locations of Path L, the middle point on the top surface along with layer 8; (j) Comparison of experimentally measured and numerically computed von Mises stress along Path L.

5.3. RESIDUAL STRESS VALIDATION WITH EXPERIMENTS

Numerically predicted von Mises stresses are compared with experimental measurement along Path L (the middle line on the top surface along deposited layer), as shown in Figure 8i-j. Measured von Mises stresses were obtained using XRD with $\sin 2\psi$ technique [39]. In XRD measurement, the residual stress is calculated from diffraction line displacement. When residual stress emerges in the sample, the interval between lattice planes will change. This can be manifested by the diffraction peak shift and the shift distance depends on the residual stress level. As X-rays scan the sample, this stress-induced diffraction shift can be measured by the change of diffraction angle 2θ. The stress is calculated from the slope of 2θ to $\sin 2\psi$, where ψ is orientation between normal to the diffracting lattice planes and the sample surface. In the FEA simulation, the stress curve can be readily extracted. Figure 8j shows that residual stress presents the greatest magnitude underneath the wall center and decreases as close to the wall end. Overall, the numerical and experimental curves show fairly good agreement. It can be concluded that simulation can successfully duplicate the stress evolution as experiments for laser repairing in the LDMD process.

6. CONCLUSIONS

This work presented an advanced automated damage detection and damage reconstruction algorithm for a damaged gear tooth repair. The defective geometry of the damaged model was detected and compared with the nominal model. Then the damaged model was aligned with the nominal model. After that, both models were sliced into

layers, and a set of parallel and equidistant casting rays were used to intersect with these layers to extract the repair volume. Based on the reconstructed 3D model of the gear, a processing strategy was developed to perform precision deposition on the repaired position to accurately restore the gear geometry. This advanced damage detection method fulfills fast and automated repair for complicated geometry.

Then, SS304L powder particles were deposited on the damaged region using the laser-aided direct metal deposition (LDMD) process to validate the repair through the proposed damage reconstruction method. In terms of repair duration, this automated damage reconstruction strategy is time saving than conventional method. Microstructure analysis and hardness were carried out to evaluate the quality of repaired part. Micrographs taken at cross-section near the bonding area were noticed at good metallurgical bonding and fabrication defects such as delamination, pores, and cracks were not detected in microstructure analysis. The hardness of deposition is between 400 HV and 450 HV, which is higher than that of the substrate. These repair experiments confirmed high efficiency and high quality of our repair algorithm.

Finally, a 3D finite element model based on thermo-mechanical analysis was developed to simulate the LDMD process of the gear repair process, for accurately predicting deformation and stress behavior of the repair process. It was observed that residual stresses are larger along the scan direction than the perpendicular direction. The average equivalent stresses show lower values than yield stress. The thermo-mechanical FEA model further validated that the proposed repair algorithm is successful and efficient for the automated repair of the damaged gear.

REFERENCES

[1] Zhang X, Li W, Adkison KM, Liou F (2018) Damage reconstruction from tri-dexel data for laser-aided repairing of metallic components. Int J Adv Manuf Technol.

[2] Davis JR (2005) Gear Materials, Properties, and Manufacture. ASM International.

[3] Zhang X, Li W, Cui W, Liou F (2018) Modeling of worn surface geometry for engine blade repair using Laser-aided Direct Metal Deposition process. Manuf Lett 15:1–4.

[4] Gao J, Folkes J, Yilmaz O, Gindy N (2005) Investigation of a 3D non - contact measurement based blade repair integration system. Aircr Eng Aerosp Technol 77:34 - 41.

[5] Pantazopoulos G, Zormalia S (2011) Analysis of the failure mechanism of a gripping tool steel component operated in an industrial tube draw bench. Eng Fail Anal 18:1595–1604.

[6] Grum J, Slabe JM (2003) A comparison of tool–repair methods using CO2 laser surfacing and arc surfacing. Appl Surf Sci 208–209:424–431.

[7] Pleterski M, Tušek J, Kosec L, et al (2010) LASER REPAIR WELDING OF MOLDS WITH VARIOUS PULSE SHAPES. Metalurgija 49:41–44.

[8] Song J, Deng Q, Chen C, et al (2006) Rebuilding of metal components with laser cladding forming. Appl Surf Sci 252:7934–7940.

[9] Nowotny S, Scharek S, Beyer E, Richter K-H (2007) Laser Beam Build-Up Welding: Precision in Repair, Surface Cladding, and Direct 3D Metal Deposition. J Therm Spray Technol 16:344–348.

[10] Rafi HK, Starr TL, Stucker BE (2013) A comparison of the tensile, fatigue, and fracture behavior of Ti – 6Al – 4V and 15-5 PH stainless steel parts made by selective laser melting. Int J Adv Manuf Technol 69:1299–1309.

[11] Al-Jamal OM, Hinduja S, Li L (2008) Characteristics of the bond in Cu–H13 tool steel parts fabricated using SLM. CIRP Ann 57:239–242.

[12] Pinkerton AJ, Wang W, Li L (2008) Component repair using laser direct metal deposition. Proc Inst Mech Eng Part B J Eng Manuf 222:827–836.

[13] Wilson JM, Piya C, Shin YC, et al (2014) Remanufacturing of turbine blades by laser direct deposition with its energy and environmental impact analysis. J Clean Prod 80:170–178.

[14] Graf B, Gumenyuk A, Rethmeier M (2012) Laser metal deposition as repair technology for stainless steel and titanium alloys. Phys Procedia 39:376–381.

[15] Paydas H, Mertens A, Carrus R, et al (2015) Laser cladding as repair technology for Ti–6Al–4V alloy: Influence of building strategy on microstructure and hardness. Mater Des 85:497–510.

[16] Liu R, Wang Z, Sparks T, et al (2017) Stereo vision-based repair of metallic components. Rapid Prototyp J 23:65–73.

[17] Song L, Zeng G, Xiao H, et al (2016) Repair of 304 stainless steel by laser cladding with 316L stainless steel powders followed by laser surface alloying with WC powders. J Manuf Process 24:116–124.

[18] Xinchang Zhang, Wei Li, Katelyn M. Adkison, Frank Liou, Damage reconstruction from tri-dexel data for laser-aided repairing of metallic components, The International Journal of Advanced Manufacturing Technology (2018), 96:3377–3390.

[19] Xinchang Zhang, Wei Li, Frank Liou, Damage detection and reconstruction algorithm in repairing compressor blade by direct metal deposition, The International Journal of Advanced Manufacturing Technology (2018) 95:2393–2404.

[20] Zhang, X., Pan, T., Li, W. et al. Experimental Characterization of a Direct Metal Deposited Cobalt-Based Alloy on Tool Steel for Component Repair. JOM 71, 946–955 (2019).

[21] G. Fang, C. -D. Matte, R. B. N. Scharff, T. -H. Kwok and C. C. L. Wang, "Kinematics of Soft Robots by Geometric Computing," in IEEE Transactions on Robotics, vol. 36, no. 4, pp. 1272-1286, Aug. 2020.

[22] Ghavidelnia, Naeim; Bodaghi, Mahdi; Hedayati, Reza. 2021. "Femur Auxetic Meta-Implants with Tuned Micromotion Distribution" Materials 14, no. 1: 114.

[23] Hedayati, Reza; Ghavidelnia, Naeim; Sadighi, Mojtaba; Bodaghi, Mahdi. 2021. "Improving the Accuracy of Analytical Relationships for Mechanical Properties of Permeable Metamaterials" Appl. Sci. 11, no. 3: 1332.

[24] Ghavidelnia, Naeim; Bodaghi, Mahdi; Hedayati, Reza. 2021. "Idealized 3D Auxetic Mechanical Metamaterial: An Analytical, Numerical, and Experimental Study" Materials 14, no. 4: 993.

[25] Li, L., Zhang, X., Cui, W. et al. Temperature and residual stress distribution of FGM parts by DED process: modeling and experimental validation. Int J Adv Manuf Technol 109, 451–462 (2020).

[26] Li, Qinan, Balachander Gnanasekaran, Yao Fu, and G. R. Liu. "Prediction of Thermal Residual Stress and Microstructure in Direct Laser Metal Deposition via a Coupled Finite Element and Multiphase Field Framework." JOM 72, no. 1 (2020): 496-508.

[27] Mukherjee, T., J. S. Zuback, W. Zhang, and T. DebRoy. "Residual stresses and distortion in additively manufactured compositionally graded and dissimilar joints." Computational Materials Science 143 (2018): 325-337.

[28] Yang, Qingcheng, Pu Zhang, Lin Cheng, Zheng Min, Minking Chyu, and Albert C. To. "Finite element modeling and validation of thermomechanical behavior of Ti-6Al-4V in directed energy deposition additive manufacturing." Additive Manufacturing 12 (2016): 169-177.

[29] M. Megahed, H.-W. Mindt, N. N'Dri, H. Duan, O. Desmaison, Metal additive manufacturing process and residual stress modeling, Integrat. Mater. Manuf. Innov. 5 (2016) 1–33.

[30] P. Peyre, P. Aubry, R. Fabbro, R. Neveu, A. Longuet, Analytical and numerical modelling of the direct metal deposition laser process, J. Phys. D Appl. Phys. 41(2018)025403.

[31] Jeff Irwin, P. Michaleris, A Line Heat Input Model for Additive Manufacturing, J. Manuf. Sci. Eng 138(11), 111004 (Jun 23, 2016).

[32] ANSYS Theory Manual, Release 8.1, ANSYS Inc., USA, 2004.

[33] Ole Sigmund, Notes and Exercises for the Course:FEM-Heavy (41525), Technical University of Denmark, 2011.

[34] Mills KC (2002) Recommended values of thermophysical properties for selected commercial alloys. Woodhead Publishing.

[35] Li L, Lough C, Replogle A, et al (2017) Thermal modeling of 304L stainless steel selective laser melting. In: Proceedings of the ASME 2017 International Mechanical Engineering Congress and Exposition, Advanced Manufacturing, Tampa, FL, USA. pp 1068–1081.

[36] Shamsaei N, Yadollahi A, Bian L, Thompson SM (2015) An overview of Direct Laser Deposition for additive manufacturing; Part II: Mechanical behavior, process parameter optimization and control. Addit Manuf 8:12–35.

[37] Cheng B, Shrestha S, Chou K (2016) Stress and deformation evaluations of scanning strategy effect in selective laser melting. Addit Manuf 12:240–251.

[38] Lin WC, Chen C (2006) Characteristics of thin surface layers of cobalt-based alloys deposited by laser cladding. Surf Coatings Technol 200:4557–4563. https://doi.org/10.1016/j.surfcoat.2005.03.033.

[39] Prevey PS (1986) X-ray diffraction residual stress techniques. ASM Int ASM Handbook 10:380–392.

IV. EXPERIMENTAL AND NUMERICAL INVESTIGATION IN DIRECTED METAL DEPOSITION FOR COMPONENT REPAIR

Lan Li, Xinchang Zhang, Frank Liou

Department of Mechanical and Aerospace Engineering, Missouri University of Science and Technology, Rolla, MO 65409

ABSTRACT

Directed energy deposition (DED) has been widely used for component repair. In the repair process, the surface defects are machined to a groove or slot and then refilled. The sidewall inclination angle of the groove geometry has been recognized to have a considerable impact on the mechanical properties of repaired parts. The objective of this work was to investigate the feasibility of repairing various V-shaped defects with both experiments and modeling. At first, the repair volume was defined by scanning the defective zone. Then, the repair volume was sliced to generate the repair toolpath. After that, the DED process was used to deposit Ti6Al4V powder on the damaged plates with two different slot geometries. Mechanical properties of the repaired parts were evaluated by microstructure analysis and tensile test. Testing of the repaired parts showed excellent bonding between the deposits and base materials with the triangular slot repair. 3D finite element analysis (FEA) models based on sequentially coupled thermo-mechanical field analysis were developed to simulate the corresponding repair process. Thermal histories of the substrate on the repair sample were measured to calibrate the 3D coupled thermo-mechanical model. The temperature measurements showed very good verification with the predicted temperature results. After that, the validated model was used to predict the

residual stresses and distortions in the parts. Predicted deformation and stress results can guide the evaluation of the repair quality.

1. INTRODUCTION

Many metallic components are frequently subjected to severe working conditions during service, such as alternating heavy loads, high temperature, high pressure, and wear, which can easily cause defects on these parts. Frequent failures of these components can lead to a severe drop in productivity and process efficiency. Repair or remanufacturing damaged components provides solutions to increase their life economically with minimal interruption in the production process. The typical repair process mainly involves two steps. First, the irregular surface defects are machined by creating a V-shaped groove. Second, suitable materials are deposited back into the damaged zone using welding or additive manufacturing methods [1]. The laser-aided directed energy deposition (DED) process has shown great applications in the field of component repair [2,3]. DED is a typical additive manufacturing process that can create fully dense complex parts by directly melting materials and depositing them on the workpiece layer-by-layer following a user-defined tool path [4–7]. In this process, a high-power laser with a very small concentration area is used to create a molten pool on the damaged parts. The filler material, usually powders, experiences melting and cooling, and then solidifies to form the deposits. The deposits are usually fully dense and can form an excellent bond with the base parts [8,9] and have high mechanical properties, including tensile strength and fracture toughness [10,11]. For component repair, DED

outperforms conventional repair approaches, with the following advantages: (1) precise control of the heating and deposition rate over the geometry and substrate; (2) better compatibility with many advanced materials; and (3) automation capability [12–16].

In the pre-repair process, a V-groove down to the defects is first obtained by removing the defects and surrounding materials so that the DED tools can access the damaged zone. After that, the repair volume is defined, and the damage is then refilled by depositing appropriate materials following the defined repair volume. In the DED process, a high-energy laser beam emits the powder nonuniformly. This high-intensity laser can produce complex thermal history and significant thermal residual stresses. Residual stress induced by a high thermal gradient is likely to cause distortion, cracking, and fatigue failure and impacts the quality of the repaired product. Many endeavors have been made to alleviate the undesirable effects and hence reduce the defects of the finished part. It has been recognized that V-groove geometry imposes a considerable impact on the mechanical performance of finished parts. For example, Graf [17] has analyzed the feasibility of laser metal deposition for refilling different V-groove shapes with both stainless steel and Ti6Al4V by experiments. They reported that the V-groove should be wide enough to ensure a successful rebuild without defects. Pinkerton [18] machined varied V-groove-shaped defects on H13 tool steel substrates and then repaired the missing volumes using the DED process. They concluded that a steep sidewall tilt angle cannot guarantee good metallurgical bonding between the as-deposited material and damaged parts because of the lower laser energy on the steep sidewall. Zhang et. al. [19] repaired three V-shaped defects with varied sidewall inclination angles on H13 tool steel

substrates with a cobalt-based alloy. The microstructure and mechanical properties of rebuilt samples revealed that materials can be successfully deposited on H13 tool steel, except for 90° sidewall damage with a lack of fusion and many pores. Some works have tried to accomplish better repair performance under slot geometry with various materials [20–23]. Paul et. al. [24] reported that they were able to produce fully dense and crack-free WC-Co coatings on low carbon steel with excellent interfacial bonding and much higher hardness. Zhang et al. [25–27] repaired damaged compressor blades and damaged dies using the DED process. They concluded that the sidewall inclination angle of the slot should be carefully determined to obtain high-quality repair.

It is instructed that the sidewall tilt angle for V-groove geometry considerably affects the bonding condition of the filler material and substrate since it affects how laser melts the materials on the sidewall. However, there is no direct evidence to demonstrate the causality in the current literature. A clear understanding of that causality helps to optimize the sidewall inclination angle and hence produces good products. Therefore, it is of particular importance to elucidate the fusion conditions and temperature distribution with metallurgical bonding. Previous studies mainly focused on microstructure and performance testing analysis by experiments, finding that it is not easy to measure temperature evolution in the melt pool. In this study, the temperature and stress evolution in the DED process was tracked by both numerical and experimental analysis. With this information, the effect of sidewall inclination angle on the emergence of defects in repaired parts can be clearly understood. The thermal history and laser intensity in the DED process can also be analyzed in order to optimize design or geometry.

The objective of this paper was to investigate the influence of V-groove geometry sidewall angles on the properties of repaired parts through both experiments and numerical modeling. In the experimental part of the study, to perform the repair, V-shaped defects with different sidewall inclination angles were prepared on Ti6Al4V substrates. The repair volume on each substrate was reconstructed by scanning the damaged region using a 3D scanner. After this, the repair toolpath was generated. Then, Ti6Al4V powders were deposited on the damaged parts using the DED process. Subsequently, the repaired parts were tested by microstructure analysis and mechanical testing. In the modeling part of the study, 3D FEA models based on sequentially coupled thermo-mechanical field analysis were developed to simulate the repair process. The simulation accurately predicted temperature and residual stress on the repaired parts. The distortion and residual stress were evaluated to study the influence of the sidewall inclination angles on repair quality. Finally, conclusions were drawn for these two repair samples.

2. EXPERIMENTAL PROCEDURE

2.1. MATERIAL PREPARATION AND EXPERIMENTAL PLANS

In order to perform the repair, Ti6Al4V rectangular plates with dimensions of 60 mm × 19 mm ×10 mm were selected as the substrate material. Two different slot geometries: one triangular (with sidewall inclination angle of 45°) and one rectangular (with sidewall inclination angle of 90°) in cross-section were machined along the mid-line of the upper surface: the slot of triangular cross-section, 6 mm wide and 3 mm deep

and with 45° included angle, the slot of rectangular cross-section with 3 mm wide and 3 mm deep, Therefore, same volume of material was thus removed from every substrate block, which are depicted in Figure 1(a), and 1(b). Ti6Al4V powders with a particle size of 50–150 mm are chosen as deposited materials. The chemical compositions of Ti6Al4V are listed in Table 1 [28].

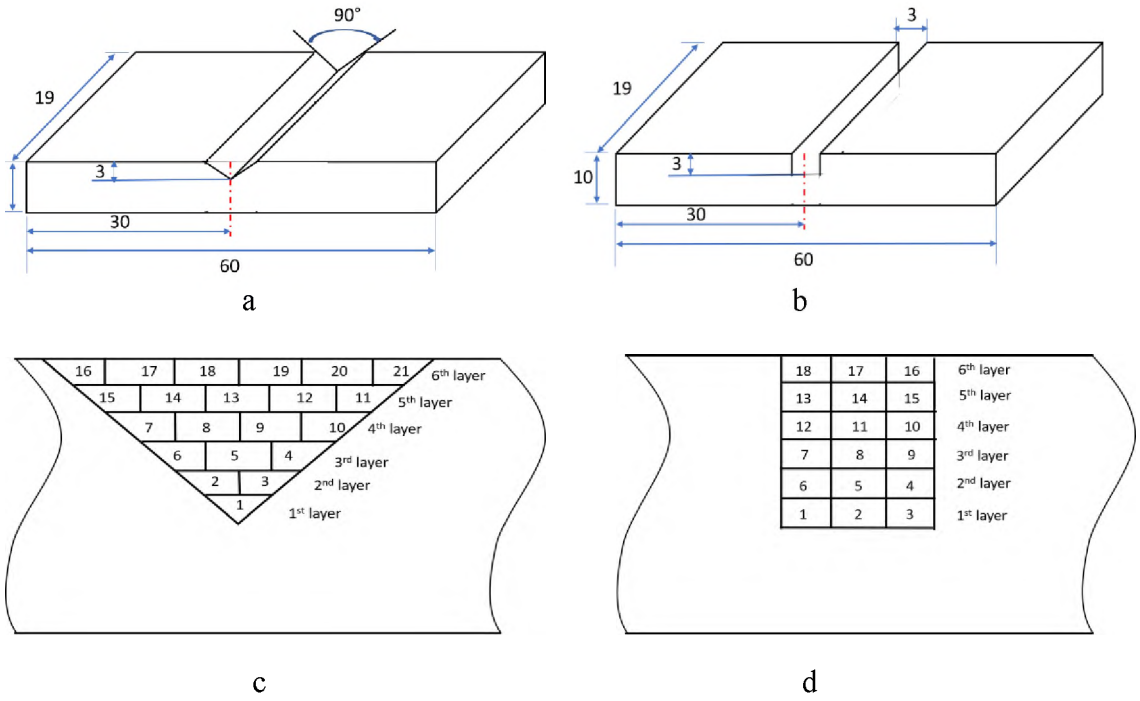

Figure 1. Schematic of the damaged component with triangular (a) and rectangular (b) slot; Schematic of scanning layers and tracks in the damaged component and repair tool path for two substrates with triangular (c) and rectangular (d) slot.

Table 1. Chemical component of the target materials (wt%).

Material	C	V	Fe	H	Al	O	Ti
Ti6Al4V	0.08	4.5	0.25	0.025	6.76	0.2	Bal.

The missing volume on each substrate should be determined to obtain the tool path for material deposition. The deposition tool path directly determines the restored geometry and has large effects on the quality of the repaired parts. In order to obtain the missing volume, the algorithm presented in [19] was used. In this process, the missing volume was directly reobtained by scanning the defective area using a structure-light 3D scanner (OptimScan 5M, Shining 3D, San Francisco, CA, USA). After the missing volume was reconstructed, the tool path was generated based on the missing volume. The missing volume was sliced into 6 layers with a layer thickness of 0.5 mm. The tool path consists of an outline contour and a zigzag infill pattern, which indicates that the laser scans the outline first and then the zigzag pattern. The laser tracks for the two different damaged geometries are schematically shown in Figure 1c, d.

After the repair tool path was acquired, the damaged substrates were repaired using a DED system. In this study, the DED system consisted of a YAG fiber laser (IPG

Table 2. Processing parameters for repair experiment.

Experiment parameters	Values
Power, P [W]	650
Powder flow rate, [g/min]	2.8
Scan speed, [mm/min]	210
Laser diameter, d [mm]	1
Layer thickness, [mm]	0.5
Number of laser tracks, N	21/18

Photonics, Oxford, MA, USA) with a peak power of 1 kW, a powder feeding system, a 3-axis worktable, and an enclosure purged with argon gas. During the repair process, the laser beam was kept stationary and the workpiece was moved according to the repair tool path. The processing parameters are listed in Table 2. In the experiment, the substrate was clamped at two ends to prevent rigid body motion. For the experiment planning, the same levels of power, powder flowrate, and traverse speed were used in each experiment.

2.2. SPECIMEN PREPARATION AND MATERIAL CHARACTERIZATION

The as-deposited samples were sectioned using a Hansvedt (Hansvedt Industries Inc., Rantoul, IL, USA) electric discharge machine (EDM). Then, the samples were ground using silicon carbide abrasive papers from 120 grit to 1200 grit in sequence. Next, the samples were polished using diamond suspensions (9 μm, 6 μm, 3 μm, and 1 μm) and finally polished with 0.04 μm silica suspension. After that, the polished specimens were etched with Kroll's reagent. The morphology and microstructures were examined using a HIROX KH-8700 (HIROX, Hackensack, NJ, USA) optical microscope and a Helios NanoLab 600 (Thermo Fisher Scientific, Waltham, MA, USA) Scanning Electron Microscope (SEM). The interfacial boundary between the refilled material and substrates was studied. An energy-dispersive X-ray spectroscopy (EDS) line scan was performed from deposits to substrates to analyze elemental composition and distribution. Tensile testing was conducted to test the mechanical properties of the repaired parts. For preparing the tensile specimens, 1.0-mm-thick layers were cut from each repaired substrate, with orientations as illustrated in Figure 2a. Then the tensile specimens were

sectioned from each thin slice. The dimensions of the tensile specimens are depicted in Figure 2b. Each tensile specimen consisted of deposits and substrate, with an interface located at the middle of the specimen. The tensile test was conducted using an Instron tester (Model 3300) with a crosshead speed of 0.015 mm/min. Tensile stress-strain curves were obtained.

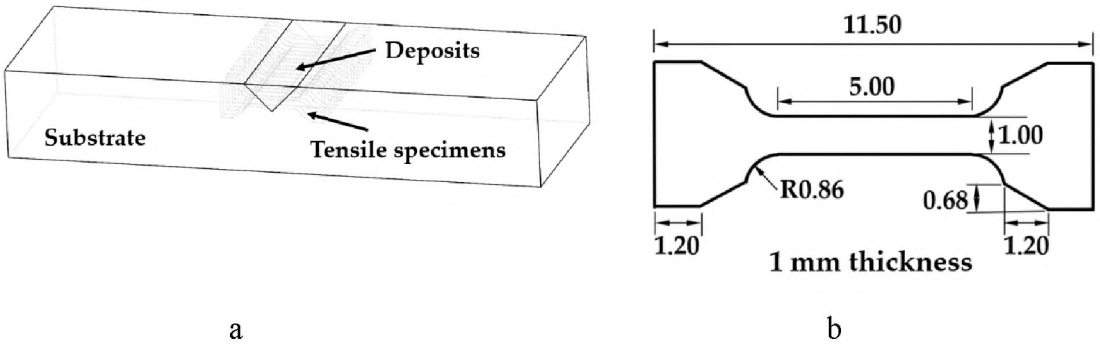

Figure 2. (a) Preparation of tensile specimens from repaired parts; (b) dimensions of tensile specimens (unit: mm).

2.3. MICROSTRUCTURE

Figure 3a, b reveal the images of the repaired parts with triangular and rectangular defects, respectively. An overview of the cross-sections of the triangular and rectangular defects is shown in Figure 3c, d, respectively. It can be observed from Figure 3c, d that the as-deposited materials bonded well with the base part for the triangular case. However, for the rectangular defect case, very large pores were found near the edge of the wall. This is because, in the repair process, the laser cannot access the sidewall due to its vertical geometry. Because of this large pore defect, the following microstructure analysis and tensile test analyses were not performed within the rectangular repair plate.

The repaired plate with triangular defects was prepared for microstructure analysis. The micrographs of the cross-sections of the deposits and the interface with the substrate are shown in Figure 4. In Figure 4a it can be seen that the interface between the as-deposited material and the substrate was very clear. In addition, there was no delamination or other defects at the interface, indicating good interfacial bonding. This excellent interfacial bonding was also confirmed by the tensile testing, described in Section 2.4. The deposits were dominated by a columnar microstructure that was growing perpendicular to the interface. These columnar structures were formed due to the directional high thermal gradient along the vertical direction. Micrographs were taken at the deposit–substrate interface (Figure 4b) and of the deposits (Figure 4c), which showed an α+β microstructure, which is typical for additively manufactured Ti6Al4V [29].

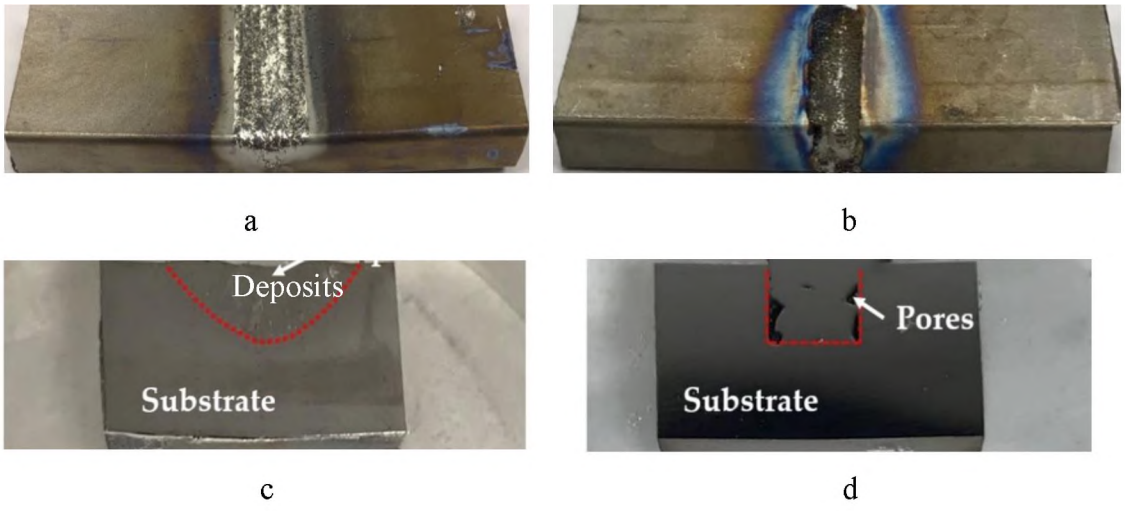

Figure 3. Repaired substrates with triangular (a) and rectangular (b) slots; overview of the cross-section of the repaired substrates with triangular (c) and rectangular (d) slots.

EDX line scan analysis were performed across the interface and the result is shown in Figure 3(d). The entire transition of Ti, Al and V was spanned in approximately 1.2mm distance, indicating the total layer diffusion. Within both sides of the interface, each content experienced smooth variation. No slight drop and rise were initiated.

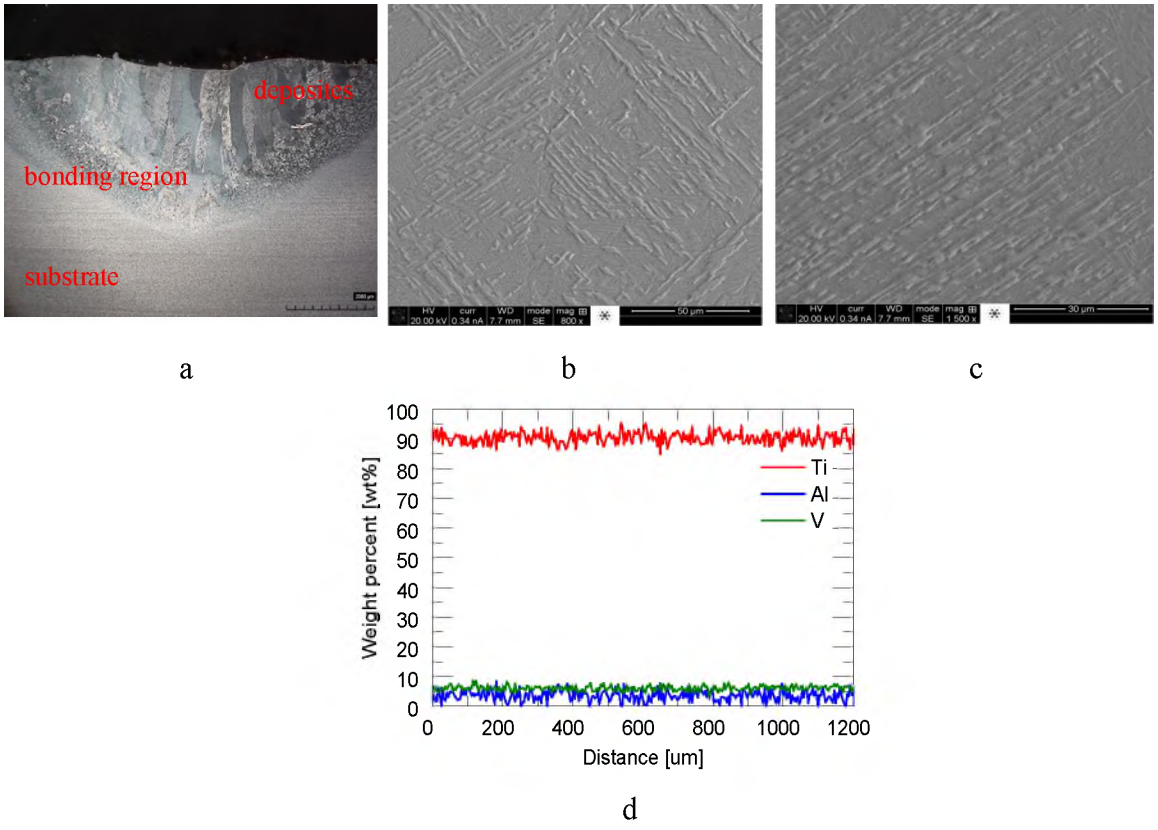

Figure 4. (a) Optical micrographs of materials on the bonding area; (b) Microstructure on deposits near the bonding area; (c) Microstructure on deposits far away the bonding area; EDS line scan cross deposits to substrates.

2.4. TENSILE BEHAVIOR

A total of nine tensile specimens for the triangular repair case were prepared and tested to evaluate the bonding strength between the as-deposited material and the

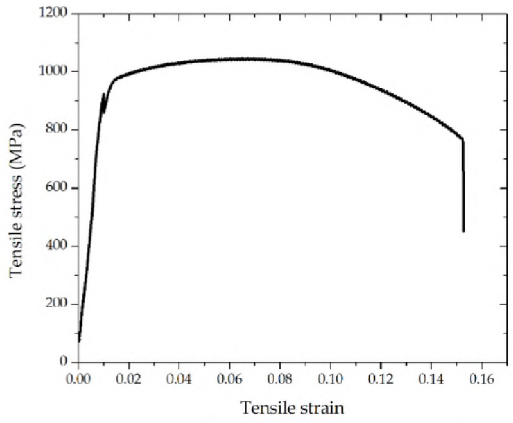

Figure 5. Tensile stress-strain curve.

Table 3. Yield strength (YS) and ultimate tensile strength (UTS) of the repaired parts.

Sample #	YS (MPa)	UTS (MPa)
1	862.08	1046.32
2	1011.82	1069.93
3	996.71	1058.80
4	905.13	1010.41
5	984.27	1029.54
6	962.05	1034.43
7	934.77	1028.68
8	955.25	1006.12
9	978.30	1050.29
Average	954.49	1037.17
S.D.	47	21

substrate. A representative tensile stress-strain curve is shown in Figure 5. The yield strength and ultimate tensile strength of all the specimens are summarized in Table 3. The testing showed that the yield strength and ultimate tensile strength of the repaired parts were 954 ± 47 MPa and 1037 ± 21 MPa, respectively. More importantly, the samples fractured at the deposit region, not at the interface, indicating a good interfacial bonding strength.

3. NUMERICAL ANALYSIS OF THE LASER REPAIR PROCESS

3.1. MODEL SETUP

In the additive manufacturing process, due to the existence of rapid thermal cycles, residual stress and deformation inevitably occur. Numerical simulation is able to capture the temperature field and thermal stress field in the repair process, which provides a theoretical basis for controlling, adjusting, and reducing residual stress, which has important academic value and practical application significance [30–35]. In this section, the Ansys® Mechanical APDL software (Ansys 2020 R1, Ansys, Inc., Canonsburg, PA, USA) was used as the platform to simulate the temperature field and the stress-strain field of the multi-layer laser repair process.

First, the geometric model with a triangular crack was established to explain the simulation procedure. According to the actual laser deposition process of multi-layer multi-pass, a 6-layer 21-pass geometric model was established. Figure 6a shows the geometry of the 3D numerical modeling domain of the damaged part. The intact section with the damaged slot is shown in Figure 6b, c. Therefore, 21 tracks were planned for

the total repair process. The laser transverse speed was 210 mm/min. The element of the new material addition with 0.5 mm thickness was activated sequentially in the laser scanning direction to simulate the material addition process. All processing parameters

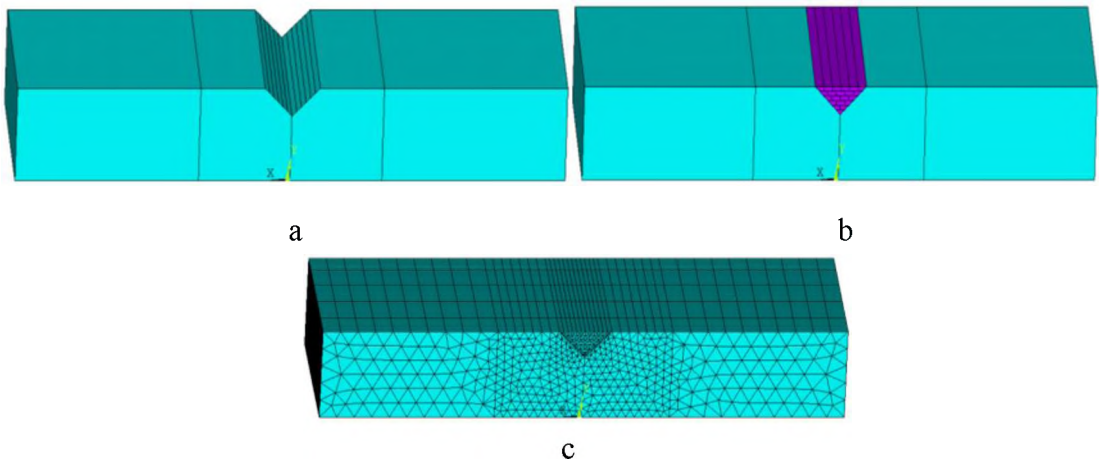

Figure 6. (a) FEA model geometry of the damaged die; (b) Laser scan strategy of 21 tracks of repair volume; (c) Finite element mesh for DMD process simulation.

Table 4. Input parameters for the numerical simulation.

Experimental Parameters	Values
Power	650 W
Laser absorptivity	0.3
Effective scan speed	210 mm/min
Laser diameter	1 mm
Time step	0.1 s

are listed in Table 4. The domain was meshed with one deposition layer, being one element tall (0.5 mm) and four elements wide. The final model contained a total of 37,920 elements. The finite element mesh configuration of the repair domain is shown in Figure 6c.

3.2. THERMAL AND MECHANICAL ANALYSIS

The transient temperature distribution in the entire volume of the material can be obtained from the 3D heat conduction equation [36]:

$$\frac{\partial(\rho c_p T)}{\partial t} = \frac{\partial}{\partial x}(k\frac{\partial T}{\partial x}) + \frac{\partial}{\partial y}(k\frac{\partial T}{\partial y}) + \frac{\partial}{\partial z}(k\frac{\partial T}{\partial z}) + Q \tag{1}$$

where k is the thermal conductivity, ρ is the density, c_p is the specific heat, all of these thermal mechanical properties are temperature dependent, T is the current temperature, Q is the internal heat generation rate per unit volume, t is the time, x, y and z are the coordinates in the reference system.

The plate is clamped at the left and right surfaces. Both convection and radiation conditions are considered in all external surfaces which are applied to all free surfaces. These heat transfer mechanisms are expressed as:

$$\ddot{q} = -k\frac{\partial T}{\partial z} + h\left(T - T_0\right) + \varepsilon\sigma\left(T^4 - T_0^4\right) \tag{2}$$

where T is temperature of the workpiece, h is the heat transfer coefficient of natural convection, which is assumed to be dependent on temperature and is presented in Table 3, σ is the Stefan—Boltzmann constant of 5.67×10^{-8} W/m^2·K^4 and ε is the surface emissivity of 0.3. where T_0 is the ambient temperature which equals to the temperature at

the initial time of 25°C. Moreover, heat conduction at the contact interface between the plate and the clamping system is considered to account for the thermal inertia of the supporting structure. By correlating simulated and experimental results, the heat transfer coefficient used for Newton's model is set to 100 [W/m^{2}·°C].

Table 5. The convection heat transfer coefficient used in the simulation.

Temperature (°C)	25	200	400	600	800	1000	1500	2000
h, (W/(m^2 • K))	12	24	40	72	80	100	100	100

The stress equilibrium equation is written as [37-38]:

$$\nabla \cdot \sigma = 0 \tag{3}$$

where σ is the second-order stress tensor associated with the material behavior law.

Total strain ε component, assuming small deformation thermo-elasto-plasticity, is represented as [39]:

$$\varepsilon = \varepsilon^{e} + \varepsilon^{p} + \varepsilon^{th} \tag{4}$$

where ε^{e}, ε^{p}, and ε^{th} are the elastic strain, plastic strain and thermal strain, respectively. The isotropic Hooke's law was used to model the elastic strain (ε^{e}) in Equation (5). The thermal expansion coefficient was adopted to calculate the thermal strain in Equation (6). Elastic-plastic stain stress behavior was described by a bilinear stress-strain curve starting at the origin with positive stress and strain values, which was defined by elastic modulus E, Poisson's ratio ν, yield strength σ_Y, and tangent modulus G. This is called bilinear isotropic hardening (BISO) model in ANSYS software.

The mechanical constitutive law can be written as [39]:

$$\sigma = C\varepsilon^{e} \tag{5}$$

where C is the fourth-order material stiffness tensor and ε^{e} is the second-order elastic strain tensor.

The thermal strain ε^{th} is given by:

$$\varepsilon^{th} = \alpha \cdot \triangle T \tag{6}$$

where α is the thermal expansion coefficient and ΔT is the temperature change in a certain time duration.

In the temperature field analysis, the heat flux density load with uniform power density, has been developed to model the heat input of the scanning laser. The heat flux is applied on the active element of the powder via an Ansys APDL subroutine. The heat source was considered a constant and uniformly distributed body heat flux defined as:

$$Q = \frac{\alpha P}{\pi r^{2} t} \tag{7}$$

where α is the laser absorption coefficient, set as 0.3 according to the experiments conducted, P is the power of the continuous laser, r is the radius of the laser beam and t is the layer thickness.

The thermo-physical properties and mechanical properties were temperature-dependent and identified in [35,40], as shown in Table 4.

Table 6. Thermo-mechanical properties of the tool steel Ti6Al4V.

Temperature (°C)	25	100	200	300	400	600	800	1200	1300	1600
Density, (kg/m3)	4420	4406	4395	4381	4366	4336	4309	4252	4240	3920
Thermal conductivity, (W/(mK))	7	7.45	8.75	10.15	11.35	4.2	17.8	23	24	50
Specific heat, (J/(kgK))	500	502	505	510	513	518	522	530	530	530
Thermal expansion coefficient, (10^{-6}/K)	10	10	10	10	10	10	10	11	11	11
Poisson's ratio	0.33	0.33	0.33	0.33	0.33	0.33	0.33	0.33	0.33	0.33
Elastic modulus, (GPa)	125	120	115	105	93	40	25	15	12	8
Yield strength, (MPa)	850	720	680	630	590	490	40	5	1	0.1

4. RESULTS AND DISCUSSION

4.1. TEMPERATURE EVALUATION

Figure 7 presents the simulated temperature distribution at each deposition in the triangular defect case, where the laser is applied to the end of the 1st track in Figure 7a, followed by the 16th and 21st tracks in Figure 7b, c, respectively. The deposition of the first track generates a temperature of 1854 °C, and the substrate remains at a transient room temperature. Measured from the zoom-in temperature contours, the depth of the area where the temperature was higher than the melting point was 0.85 mm, as shown in Figure 7d (the zone encompassed by the grey color depicted in the melt pool). It can be

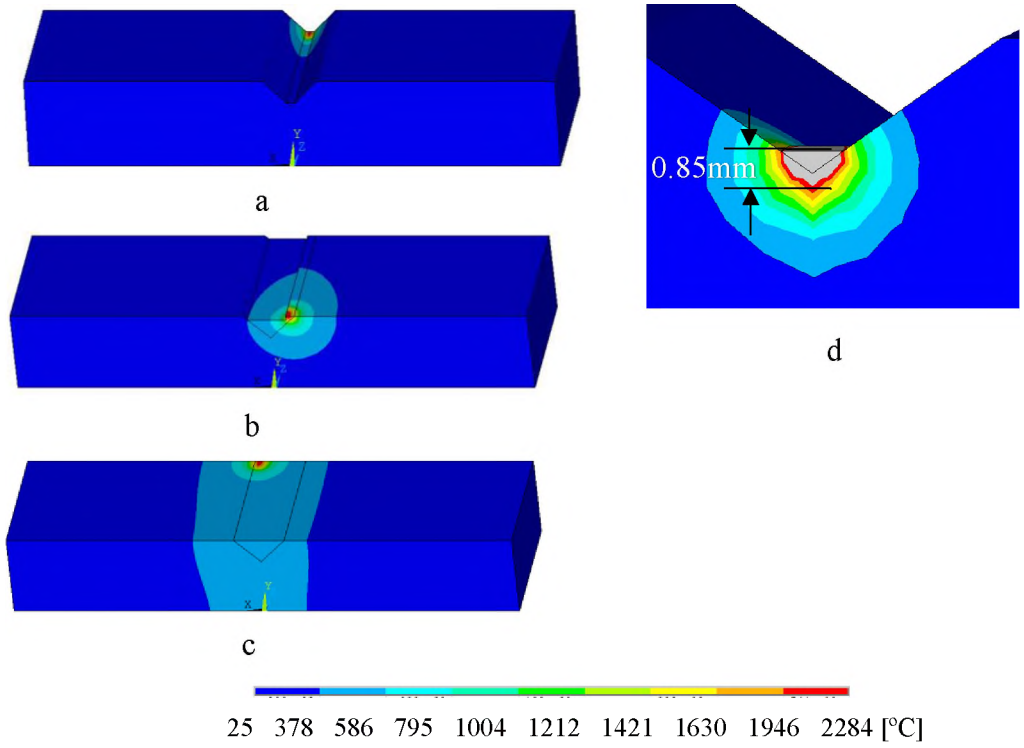

Figure 7. Temperature distribution at the end of nth track, n is 1 (a), 16 (b) and 21 (c).

observed that the melt depth was deep enough to enable fully metallurgical bonding be-tween the first deposited layer and the base substrate. The deposition of the 16th and 21st tracks experienced temperatures of 2029 °C and 2284 °C, respectively, but higher temperatures were observed in the substrate near the heat-affected zone compared to the first track due to the thermal accumulation.

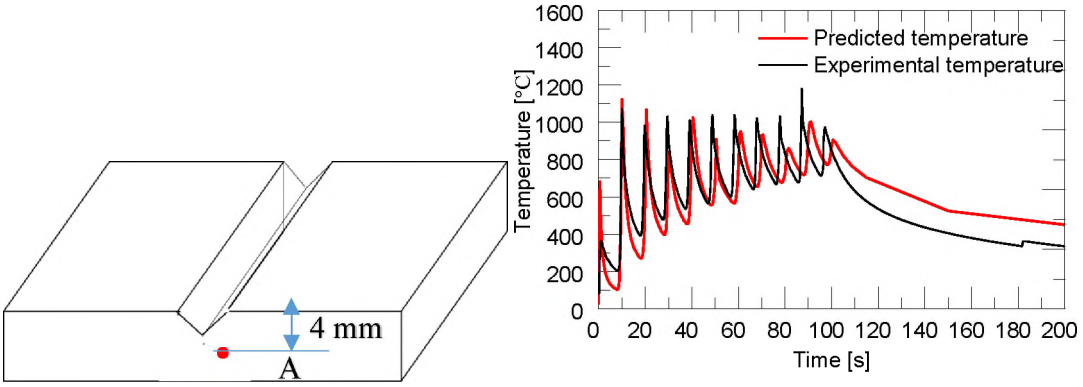

a b

Figure 8. (a) The locations of each measurement, Point A(TC1); (b) The simulated and measured temperature history during the deposition at each selected position, Point A.

Figure 8b shows the simulated temperature history during the deposition process at the selected position, Point A, as depicted in Figure 8a. Point A is located at the side sur-face of the substrate. Point A corresponds to experimental measurements at the thermo-couple location TC1 of the substrate. The temperature evolution obtained from numerical simulations and experimental measurements during the real manufacturing process are compared in Figure 8b. The red line and black lines indicate predicted temperature and experimental measurement data, respectively. It was observed that both simulation and experimental observations followed the same trends. The agreement is

notable. The heating stage corresponded to the deposition of the sequence of 21 deposited layers until completing the build, including 11 temperature peaks. After the deposition process was completed, the accumulated heat gradually dissipated, and the substrate gradually cooled down.

4.2. DISTORTION AND STRESS EVALUATION

Figure 9 shows the thermal stress and distortion evaluation in the longitudinal direction (along the laser moving direction) of two selected points, 1 and 2, which are located at the mid-points of the first and ninth deposition tracks (shown in Figure 9a; point 1 is in the substrate). Both numerical curves show several peaks due to the regular movement of the laser heat source to deposit the different layers. As the laser heat source approaches the selected point, the temperature and thermal stress at this point rise rapidly to the highest point. When the heat source is far away, the temperature and the thermal stress will gradually decrease until it is stable. After the depositing started, the temperature and thermal stress of point 1 were relatively high, with a temperature of 1854 °C. The thermal stress was in the tensile state, with a value of 199 MPa due to the material expansion by laser irritation. The deformation was relatively high because it was located at the bottom of the V-shaped groove. As the laser heat source moved, the temperature and thermal stress kept changing. With the movement of the heat source to the upper layers and far away from point 1, the temperature and thermal stress also showed a decreasing trend. When the deposition was completed, the accumulated heat gradually dissipated, and the part gradually cooled down. Material shrinkage was shown in the compressive state due to the cooling and shrinking of these deposited layers. This

explains the longitudinal stress distributions (Sz) (along the laser moving direction) for different process times, shown in Figure 9c.

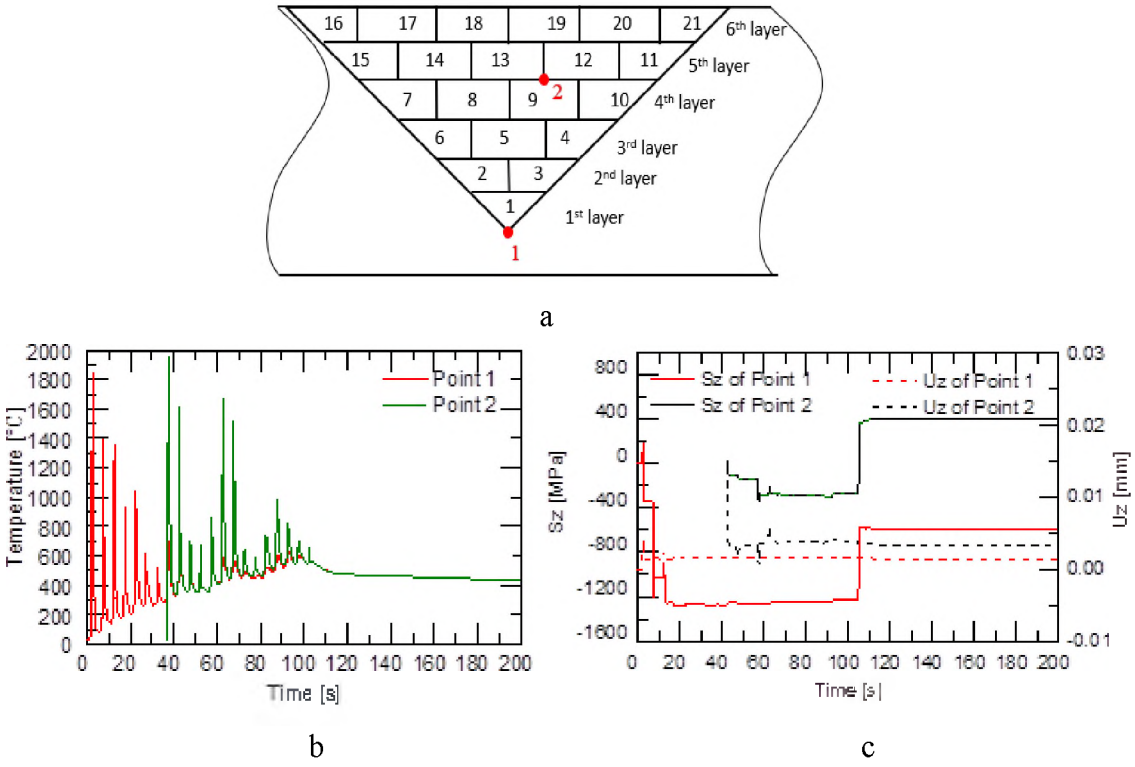

Figure 9. (a) Location of points 1 and 2; (b) Curve graph of cycles in temperature; (c) Thermal stress and distortion on the first and ninth track.

Figure 10a shows the variations in the longitudinal stress after the first track. The thermal expansion of the melt pool led to large compressions in the material around this zone. Next, as the melt pool moved to the 8th track in the fourth layer (Figure 10b), the maximum compressive stresses were transferred to the heat affected zone (HAZ) below the melt pool. After the deposition (Figure 10c), large longitudinal tensile stresses of 1030 MPa were induced at the interface with the substrate. The continuous cooling to

room temperature resulted in very high tensile stress values of 1525 MPa at the top surface of the substrate.

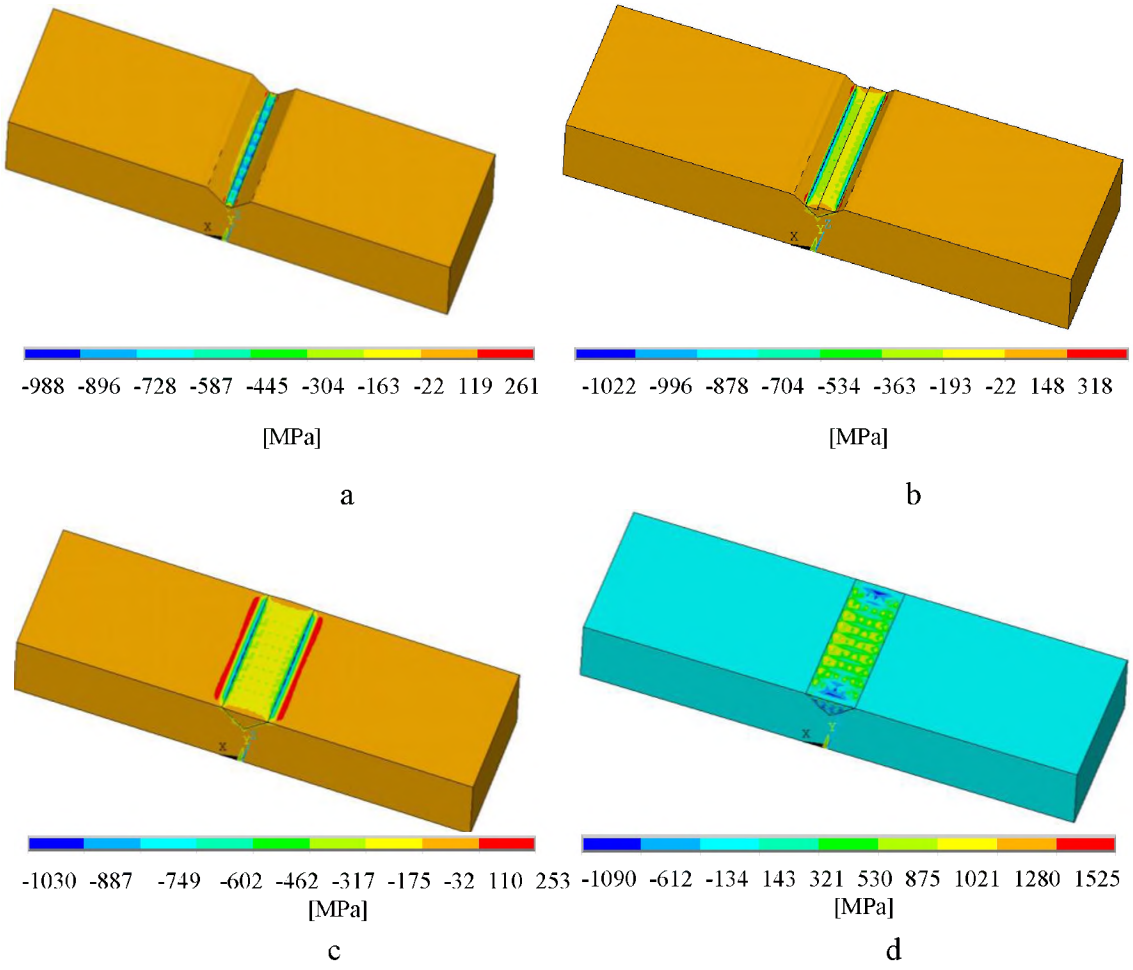

Figure 10. Graph of the longitudinal stress distributions for different track.

Figure 11c, d show the longitudinal stress distribution (Sz) along the interface line between the substrate and the deposition (Lbottom refers to the interface line between the deposit and the substrate on the bottom surface) after the deposition time of 1st, 5th, 13th, and last layers and cooling to room temperature in the triangular and rectangular repair cases, respectively. The locations of different lines are depicted in Figure 11a, b, in which

the left and right lines refer to the interface lines between the deposit and substrate on the top surface, Lleft and Lright. The middle line is represented by Lmiddle of the deposit on the top surface. The magnitude of the thermal stress near the center decreased with the progress of the deposition process due to repetitive heating and cooling. At the end of the deposition process, the top free end of the deposit cooled down to room temperature at the very end. Because of this, tensile stress accumulated near the top free end. This resulted in the accumulation of large compressive stress near the substrate–deposit interface. After the deposition was completing, due to the cooling and shrinking of these deposited layers, the distortion of the substrate sharply decreased. When cooled to room temperature, the magnitude of the compressive stress and the stress quickly transitioned into tensile stress. Hence, almost all the residual distortion developed during the initial part of the cooling phase. This can explain the trend shown in Figure 11c. The same trend was observed in the two cases and there were some differences when cooling to room temperature, which may be due to a vertical sidewall on the bottom region. The longitudinal stress after the deposition was completed and after cooling to room temperature in the rectangular repair case was slightly higher than that in the triangular case. This situation may be worsened when the defect is deep and when the open area is narrow. Figure 11e, f show the von Mises stress distributions along three lines after cooling to room temperature in the trian-gular and rectangular repair cases, respectively. When referring to Lleft and Lright, we ob-served the same trend and magnitude level with each case in respect to the von Mises stress distribution. As for the middle line, the von Mises stress values of the rectangular case (600–700 MPa) were higher than those of the triangular case (800–1000 MPa).

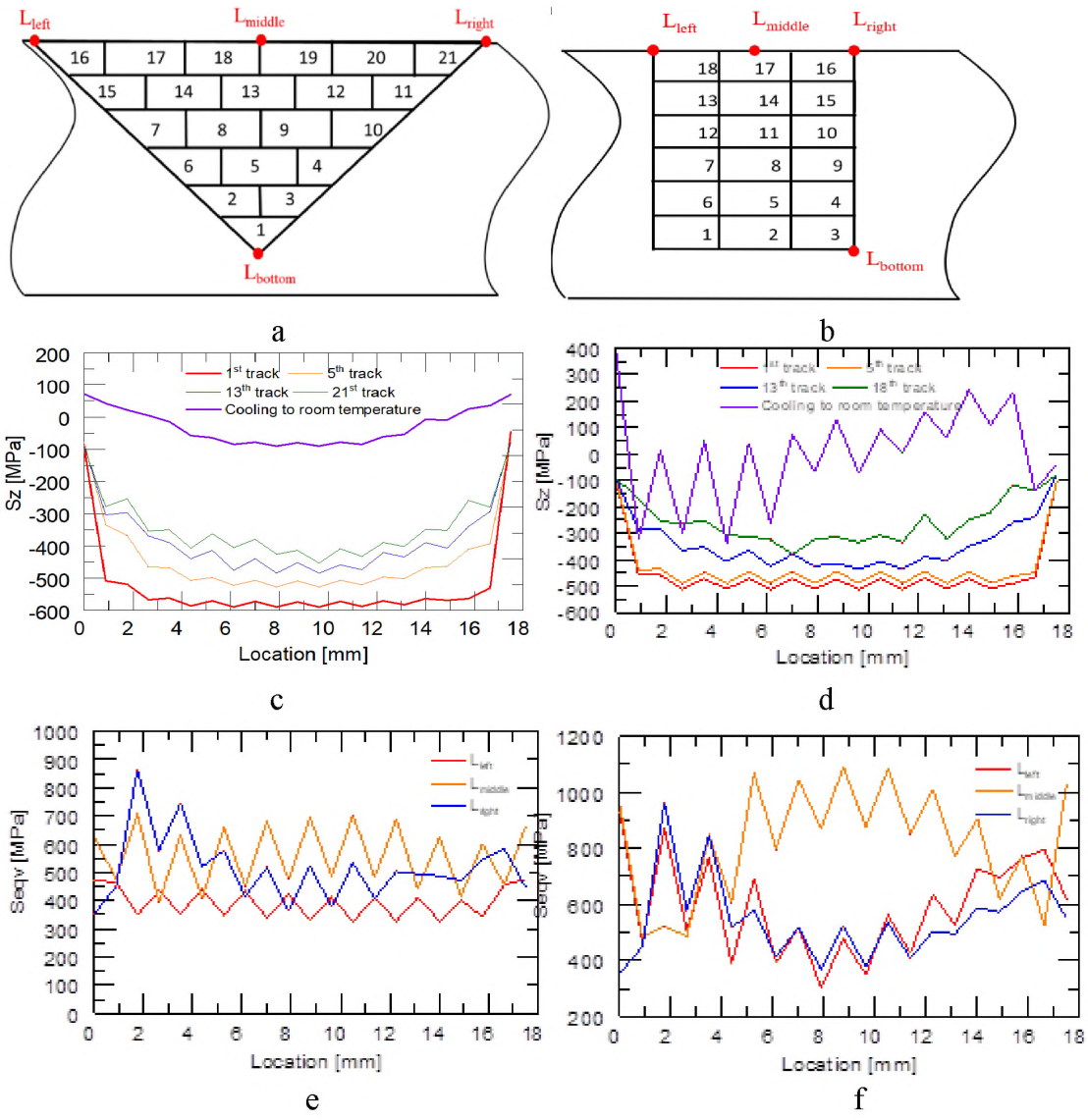

Figure 11. Schematic showing the definition of Lleft, Lright, Lmiddle, and Lbottom for the triangular (a) and rectangular (b) case; longitudinal residual stress distribution along the interface line after the deposition of 1st, 5th, 13th, and last layers in the triangular (c) and rectangular (d) repair cases; Von Mises stress distributions along three lines in the triangular (e) and rectangular (f) repair cases.

The sum displacement and von Mises stress distribution after the deposition was completed and after cooling to room temperature in the triangular case are illustrated in Figure 12a–b. The maximum displacement was formed at the interface region of the

building part, with a value of 0.08 mm. Near the bottom surface of the deposited layer, the highest residual stress was observed, with a value of 797 MPa. Residual stress could also introduce some deformation problems to the damaged plate. In the current study, the average equivalent stresses showed low values compared with the yield stress of Ti6Al4V (σy=954 MPa). As a result, no cracks were observed in deposited layers and bonding areas (Figure 4). Hence, this laser repair task can be considered successful. The

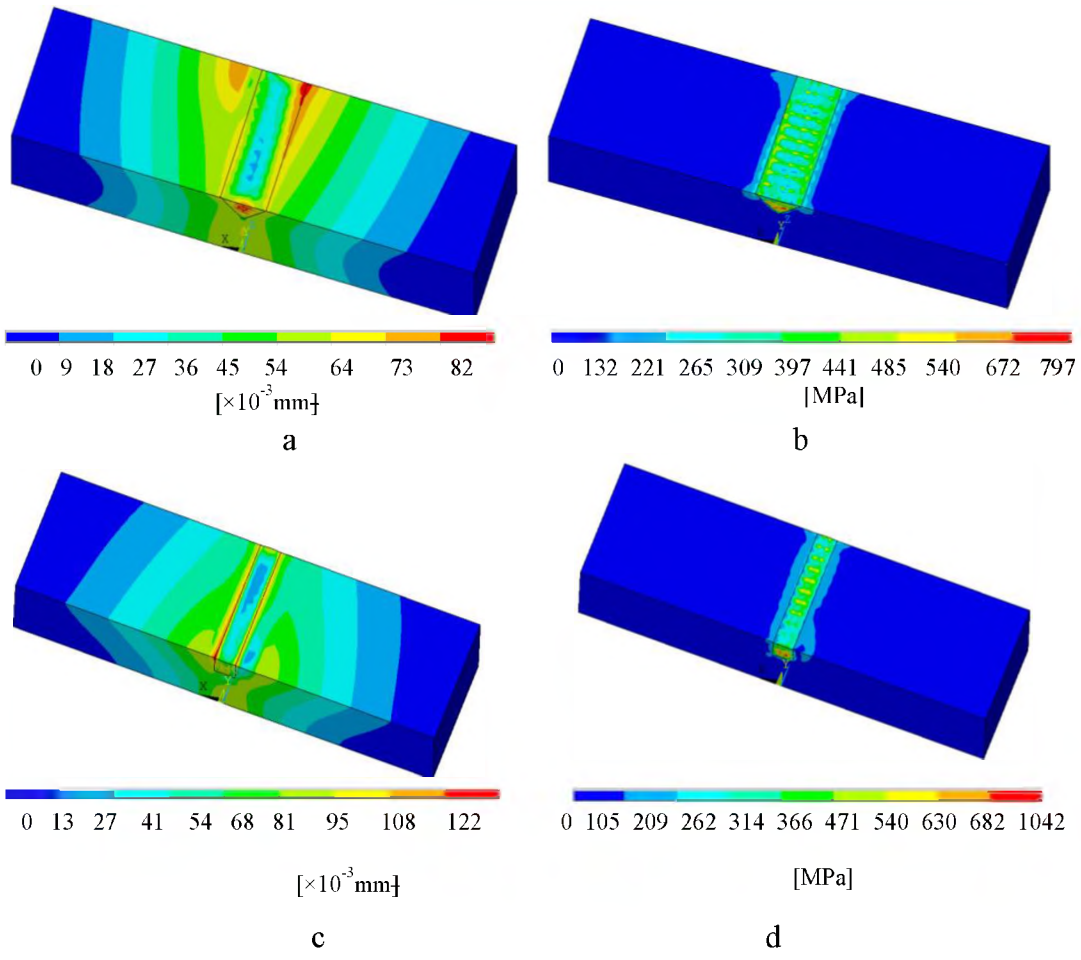

Figure 12. (a) Displacement vector sum, Usum; (b) Von Mises stress, Seqv, after all deposition done until cooling to room temperature in triangular and rectangular case (c) (d), respectively.

sum displacement and von Mises stress distribution after the deposition was completed until cooling to room temperature in the rectangular case are illustrated in Figure 12c–d. It was observed to have the same trend as the first case in respect to the sum displacement and von Mises stress distribution, except for a slightly higher value of 0.122 mm in the displacement vector. The average equivalent stresses showed that near the bottom of the deposition some values exceeded the yield stress, which may induce cracks or delamination there.

5. CONCLUSIONS

In this study, we have presented a damage reconstruction method for V-shaped groove repairs using the directed energy deposition (DED) process. The damaged parts had triangular or rectangular defects in cross-section. In this work, we investigated the feasibility of repairing two V-shaped defects with both experiments and modeling. The main conclusions are indicated below.

Ti6Al4V powder particles were deposited on the damaged region using the DED technique, following the repair toolpath. The microstructure analysis and tensile testing confirmed solid bonding along the interface for the triangular defect repair case. The tensile test showed an average ultimate tensile strength of 1037 MPa for the repaired parts, and samples fractured at the region of the deposits, not at the interface. However, for re-pairing the sample with rectangular damage, the filler material did not bond well with the substrate, causing a large number of pores.

3D finite element models based on sequentially coupled thermo-mechanical field analysis were developed to simulate the corresponding repair deposition processes. Finally, the average equivalent stresses and deformation in the triangular repair case showed low values at the intersection between the base plate and the deposited tracks than those in the rectangular repair case. The high equivalent stresses near the bottom deposition may induce cracks or delamination in the rectangular repair case. The predicted deformation and stress results will guide the evaluation of the quality of repaired parts based on repair slot geometry.

REFERENCES

[1] Zhang, X.; Cui, W.; Li, W.; Liou, F. A hybrid process integrating reverse engineering, pre-repair processing, additive manufacturing, and material testing for component remanufacturing. Materials 2019, 12, 1961, doi:10.3390/ma12121961.

[2] Nowotny, S.; Scharek, S.; Beyer, E.; Richter, K.-H. Laser beam build-up welding: precision in repair, surface cladding, and direct 3D metal deposition. J. Therm. Spray Technol. 2007, 16, 344–348, doi:10.1007/s11666-007-9028-5.

[3] Song, J.; Deng, Q.; Chen, C.; Hu, D.; Li, Y. Rebuilding of metal components with laser cladding forming. Appl. Surf. Sci. 2006, 252, 7934–7940.

[4] Li, W.; Chen, X.; Yan, L.; Zhang, J.; Zhang, X.; Liou, F. Additive manufacturing of a new Fe-Cr-Ni alloy with gradually changing compositions with elemental powder mixes and thermodynamic calculation. Int. J. Adv. Manuf. Technol. 2018, 95, 1013–1023.

[5] Zhang, K.; Liu, W.; Shang, X. Research on the processing experiments of laser metal deposition shaping. Opt. Laser Technol. 2007, 39, 549–557.

[6] Mançanares, C.G.; de Zancul, S.E.; da Silva, C.J.; Cauchick, M.P.A. Additive manufacturing process selection based on parts' selection criteria. Int. J. Adv. Manuf. Technol. 2015, 80, 1007–1014.

[7] Vaezi, M.; Seitz, H.; Yang, S. A review on 3D micro-additive manufacturing technologies. Int. J. Adv. Manuf. Technol. 2013, 67, 1721–1754.

[8] Rafi, H.K.; Starr, T.L.; Stucker, B.E. A comparison of the tensile, fatigue, and fracture behavior of Ti-6Al-4V and 15-5 PH stainless steel parts made by selective laser melting. Int. J. Adv. Manuf. Technol. 2013, 69, 1299–1309.

[9] Al-Jamal, O.M.; Hinduja, S.; Li, L. Characteristics of the bond in Cu-H13 tool steel parts fabricated using SLM. CIRP Ann. 2008, 57, 239–242.

[10] Li, T.; Chen, Y.; Wang, L. Enhanced fracture toughness in architected interpenetrating phase composites by 3D printing. Compos. Sci. Technol. 2018, 167, 251–259.

[11] Khosravani, M.R.; Zolfagharian, A. Fracture and load-carrying capacity of 3D-printed cracked components. Extrem. Mech. Lett. 2020, 37, 100692.

[12] Borrego, L.P.; Pires, J.T.B.; Costa, J.M.; Ferreira, J.M. Fatigue behaviour of laser repairing welded joints. Eng. Fail. Anal. 2007, 14, 1586–1593, doi:10.1016/j.engfailanal.2006.11.054.

[13] Zhong, M.; Liu, W.; Ning, G.; Yang, L.; Chen, Y. Laser direct manufacturing of tungsten nickel collimation component. J. Mater. Process. Technol. 2004, 147, 167–173, doi:10.1016/j.jmatprotec.2003.12.009.

[14] Borrego, L.P.; Pires, J.T.B.; Costa, J.M.; Ferreira, J.M. Mould steels repaired by laser welding. Eng. Fail. Anal. 2009, 16, 596–607, doi:10.1016/j.engfailanal.2008.02.010.

[15] Wang, W.; Pinkerton, A.J.; Wee, L.M.; Li, L. Component repair using laser direct metal deposition BT. In Proceedings of the 35th International MATADOR Conference, Taipei, Taiwan, July 27, 2007; Hinduja, S., Fan, K.-C., Eds.; Springer London: London, UK, 2007; pp. 345–350.

[16] Nikam, S.H.; Jain, N.K. Laser-based repair of damaged dies, molds, and gears BT. In Advanced Manufacturing Technologies: Modern Machining, Advanced Joining, Sustainable Manufacturing; Gupta, K., Ed.; Springer International Publishing: Cham, Switzerland, 2017; pp. 137–159, ISBN 978-3-319-56099-1.

[17] Graf, B.; Gumenyuk, A.; Rethmeier, M. Laser metal deposition as repair technology for stainless steel and titanium alloys. Phys. Procedia 2012, 39, 376–381, doi:10.1016/j.phpro.2012.10.051.

[18] Pinkerton, A.J. Advances in the modeling of laser direct metal deposition. J. Laser Appl. 2014, 27, S15001, doi:10.2351/1.4815992.

[19] Zhang, X.; Pan, T.; Li, W.; Liou, F. Experimental characterization of a direct metal deposited cobalt-based alloy on tool steel for component repair. JOM 2019, 71, 946–955, doi:10.1007/s11837-018-3221-5.

[20] Renwei, L.; Zhiyuan, W.; Todd, S.; Frank, L.; Cedo, N. Stereo vision-based repair of metallic components. Rapid Prototyp. J. 2017, 23, 65–73, doi:10.1108/RPJ-09-2015-0118.

[21] Paydas, H.; Mertens, A.; Carrus, R.; Lecomte-Beckers, J.; Tchuindjang, J.T. Laser cladding as repair technology for Ti-6Al-4V alloy: Influence of building strategy on microstructure and hardness. Mater. Des. 2015, 85, 497–510, doi:http://dx.doi.org/10.1016/j.matdes.2015.07.035.

[22] Mudge, R.P.; Wald, N.R. Laser engineered net shaping advances additive manufacturing and repair. Weld. J. N. Y. 2007, 86, 44.

[23] Song, L.; Zeng, G.; Xiao, H.; Xiao, X.; Li, S. Repair of 304 stainless steel by laser cladding with 316 L stainless steel powders followed by laser surface alloying with WC powders. J. Manuf. Process. 2016, 24, 116–124, doi:10.1016/j.jmapro.2016.08.004.

[24] Paul, C.P.; Alemohammad, H.; Toyserkani, E.; Khajepour, A.; Corbin, S. Cladding of WC-12 Co on low carbon steel using a pulsed Nd:YAG laser. Mater. Sci. Eng. A 2007, 464, 170–176, doi:10.1016/j.msea.2007.01.132.

[25] Zhang, X.; Li, W.; Adkison, K.M.; Liou, F. Damage reconstruction from tridexel data for laser-aided repairing of metallic components. Int. J. Adv. Manuf. Technol. 2018, 96, 1–14, doi:10.1007/s00170-018-1830-3.

[26] Zhang, X.; Li, W.; Chen, X.; Cui, W.; Liou, F. Evaluation of component repair using direct metal deposition from scanned data. Int. J. Adv. Manuf. Technol. 2018, 95, 3335–3348, doi:10.1007/s00170-017-1455-y.

[27] Zhang, X.; Li, W.; Liou, F. Damage detection and reconstruction algorithm in repairing compressor blade by direct metal deposition. Int. J. Adv. Manuf. Technol. 2018, 95, 2393–2404, doi:10.1007/s00170-017-1413-8.

[28] Li, W., Liou, F., Newkirk, J.; Taminger, K.M.B.; Seufzer, W.J. Investigation on Ti6Al4V-V-Cr-Fe-SS316 multi-layers metallic structure fabricated by laser 3D printing. Sci. Rep. 2017, 7, 7977.

[29] Mills, K.C. Recommended Values of Thermophysical Properties for Selected Commercial Alloys; Woodhead Publishing, Cambridge, UK, 2002; ISBN 1855735695.

[30] Farahmand, P.; Kovacevic, R. An experimental-numerical investigation of heat distribution and stress field in single- and multi-track laser cladding by a high-power direct diode laser. Opt. Laser Technol. 2014, 63, 154–168.

[31] Li, Q.; Gnanasekaran, B.; Fu, Y.; Liu, G.R. Prediction of thermal residual stress and microstructure in direct laser metal deposition via a coupled finite element and multiphase field framework. JOM 2020, 72, 496–508, doi:10.1007/s11837-019-03922-w.

[32] Mukherjee, T.; Zuback, J.S.; Zhang, W.; DebRoy, T. Residual stresses and distortion in additively manufactured compositionally graded and dissimilar joints. Comput. Mater. Sci. 2018, 143, 325–337, doi:10.1016/j.commatsci.2017.11.026.

[33] Yang, Q.; Zhang, P.; Cheng, L.; Min, Z.; Chyu, M.; To, A.C. Finite element modeling and validation of thermomechanical behavior of Ti-6Al-4V in directed energy deposition additive manufacturing. Addit. Manuf. 2016, 12, 169–177, doi:10.1016/j.addma.2016.06.012.

[34] Li, L., Zhang, X., Cui, W.; Liou, F.; Deng, W.; Li, W. Temperature and residual stress distribution of FGM parts by DED pro-cess: Modeling and experimental validation. Int. J. Adv. Manuf. Technol. 2020, 109, 451–462.

[35] Li, L.; Tan, P.; Xinchang, Z.; Yitao, C.; Wenyuan, C.; Lei, Y.; Liou, F. Deformations and stresses prediction of cantilever structures fabricated by selective laser melting process. Rapid Prototyp. J. 2021, 39, 464–470.

[36] Incropera, F.P.; DeWitt, D.P.; Bergman, T.L.; Lavine, A.S. Introduction to Heat Transfer. John Wiley & Sons, NJ, 2006.

[37] Megahed, M.; Mindt, H.-W.; N'Dri, N.; Duan, H.; Desmaison, O. Metal additive-manufacturing process and residual stress modeling. Integr. Mater. Manuf. Innov. 2016, 5, 61–93, doi:10.1186/s40192-016-0047-2.

[38] Peyre, P.; Aubry, P.; Fabbro, R.; Neveu, R.; Longuet, A. Analytical and numerical modelling of the direct metal deposition laser process. J. Phys. D. Appl. Phys. 2008, 41, 25403, doi:10.1088/0022-3727/41/2/025403.

[39] Irwin, J.; Michaleris, P. A line heat input model for additive manufacturing. J. Manuf. Sci. Eng. 2016, 138, 33662, doi:10.1115/1.4033662.

[40] Lu, X.; Lin, X.; Chiumenti, M.; Cervera, M.; Hu, Y.; Ji, X.; Ma, L.; Yang, H.; Huang, W. Residual stress and distortion of rec-tangular and S-shaped Ti-6Al-4V parts by Directed Energy Deposition: Modelling and experimental calibration. Addit. Manuf. 2019, 26, 166–179.

SECTION

2. CONCLUSION

The combined approach in this work involving experiments and thermo-mechanical FEA models to investigate the key parameters to improve the mechanical properties of different fabricate parts in LMD manufacturing. Therefore, several sets of experiments were designed to reveal the processing parameters on properties of deposited components in the method of LMD process. The microstructure, Vickers hardness, phase identification, tensile properties of LMD parts are measured to investigate the fabricated qualities. The temperature history, residual stress, and deformation of LMD parts are captured to investigate the fabricated qualities. This work helps to fully study the thermal analysis to analyze the temperature profile, cooling rate and temperature gradients on microstructure and further influences the engineered mechanical properties of build parts.

In the first work, a 3D thermo-mechanical FEA model is established to investigate the thermal and mechanical behavior of LMD technology for one Ti6Al4V coupon. The evolution of both temperature and residual stresses are analyzed. Test coupon was designed and fabricated according to the optimized process parameters. The microstructure and mechanical properties were evaluated to provide fundamental knowledge for large scale Ti6Al4V process in industry. In LMD processes, thermal gradient and cooling rate of Ti6Al4V component were found to decreases gradually along the building up direction. Thus, the maximum temperature gradient and the maximum tensile stress values occur in the first deposited layer. The cooling process and thermal

gradient show correlation to the microstructure size and mechanical performance. Along the building up direction, the cooling rate gradually decreases. As such, martensitic structure was fine at the 1st layer and turned coarser to the 10th layer. Correlatedly, the hardness reached at the highest level at the 1^{st} layer (380 HV) and gradually decreased to (340 ± 10 HV) at the 10^{th} layer.

A predictive model is developed to simulate thermal and stress evolution during the LMD process to study the feasibility of joining copper to stainless steel with nickel base alloy as intermediate layers. The transient temperature field of multiple-layer deposition of multi-structures are simulated with finite element method. The FE model can predict stress evolution as the cycling heating and cooling occurs when depositing Cu on steel with or without intermediate layers. It has been found that by introducing nickel-based alloy buffer layers, stress between the interface with buffer layers is less than that in direct joining. Again, defect-free Cu can be successfully deposited on SS304L by LMD process with experimental validation. This model can be used to predict the stress behavior of products fabricated by DED process and to help with the optimization of design and material chosen of FGMs process.

The thermo-mechanical models can be performed to test the propriate of tool path and experimental parameters for remanufacturing volume based on the repair quality. Fracture remanufacturing by LMD process was accomplished to assure a successful repair based on microstructure, predicted deformation and stress results, accuracy and quality of the repaired parts are fulfilled. When investigating the feasibility of repairing two V-shaped defects with both experiments and modeling, the microstructure analysis and tensile testing confirmed solid bonding along the interface for the triangular defect

repair case. Samples fractured at the region of the deposits, not at the interface. However, for re-pairing the sample with rectangular damage, the filler material did not bond well with the substrate, causing a large number of pores. Finally, the average equivalent stresses and deformation in the triangular repair case showed low values at the intersection between the base plate and the deposited tracks than those in the rectangular repair case. The high equivalent stresses near the bottom deposition may induce cracks or delamination in the rectangular repair case. The predicted deformation and stress results will guide the evaluation of the quality of repaired parts based on repair slot geometry.

BIBLIOGRAPHY

[1] Zhang K, Liu W, Shang X (2007) Research on the processing experiments of laser metal deposition shaping. Opt Laser Technol 39(3):549–557. https://doi.org/10.1016/j.optlastec.2005.10.009.

[2] I. Gibson, D.W. Rosen, B. Stucker, Additive Manufacturing Technologies, Springer, 2010.

[3] M. K. Imran, S. H. Masood, M. Brandt, S. Bhattacharya, and J. Mazumder, "Direct metal deposition (DMD) of H13 tool steel on copper alloy substrate: Evaluation of mechanical properties," Mater. Sci. Eng. A, vol. 528, no. 9, pp. 3342–3349, 2011.

[4] S. Bhattacharya, G. P. Dinda, A. K. Dasgupta, and J. Mazumder, "Microstructural evolution of AISI 4340 steel during Direct Metal Deposition process," Mater. Sci. Eng. A, vol. 528, no. 6, pp. 2309–2318, 2011.

[5] B. Baufeld, O. Van der Biest, and R. Gault, "Additive manufacturing of Ti–6Al–4V components by shaped metal deposition: Microstructure and mechanical properties," Mater. Des., vol. 31, pp. S106–S111, Jun. 2010.

[6] B. Dutta and F. H. (Sam) Froes, "The Additive Manufacturing (AM) of titanium alloys," Met. Powder Rep., vol. 72, no. 2, pp. 96–106, 2017.

[7] S. Gorsse, C. Hutchinson, M. Gouné, and R. Banerjee, "Additive manufacturing of metals: a brief review of the characteristic microstructures and properties of steels, Ti-6Al-4V and high-entropy alloys," Sci. Technol. Adv. Mater., vol. 18, no. 1, pp. 584–610, Dec. 2017.

[8] K. Zhang, S. Wang, W. Liu and X. Shang, Characterization of stainless steel parts by laser metal deposition shaping, Materials & Design, 55 (2014) 104-119.

[9] Z. Wang, T. A. Palmer and A. M. Beese, Effect of processing parameters on microstructure and tensile properties of austenitic stainless steel 304L made by directed energy deposition additive manufacturing, Acta Materialia, 110 (2016) 226-235.

[10] H. R. Sistla, J. W. Newkirk, and F. Frank Liou, "Effect of Al/Ni ratio, heat treatment on phase transformations and microstructure of AlxFeCoCrNi2-x (x=0.3, 1) high entropy alloys," Mater. Des., vol. 81, pp. 113–121, Sep. 2015.

[11] C. M. Lin and H. L. Tsai, "Evolution of microstructure, hardness, and corrosion properties of high-entropy Al0.5CoCrFeNi alloy," Intermetallics, vol. 19, no. 3, pp. 288–294, Mar. 2011.

[12] C. Katinas, S. Liu, Y.C. Shin, Self-sufficientmodeling of single track deposition of Ti– 6Al–4V with the prediction of capture efficiency, J. Manuf. Sci. Eng. 141 (1) (2018) (011001-011001-10).

[13] S. Liu, Y.C. Shin, Simulation and experimental studies on microstructure evolution of resolidified dendritic TiCx in laser direct deposited Ti-TiC composite, Mater. Des. 159 (2018) 212–223.

[14] L. Parry, I.A. Ashcroft, R.D.Wildman, Understanding the effect of laser scan strategy on residual stress in selective laser melting through thermo-mechanical simulation, Addit. Manuf. 12 (2016) 1–15.

[15] S. Tammas-Williams, H. Zhao, F. Léonard, F. Derguti, I. Todd, P.B. Prangnell, XCT analysis of the influence of melt strategies on defect population in Ti–6Al–4V components manufactured by selective electron beam melting, Mater. Charact. 102 (2015) 47–61.

[16] M. Strantza, R. Vafadari, D. de Baere, B. Vrancken,W. van Paepegem, I. Vandendael, H. Terryn, P. Guillaume, D. van Hemelrijck, Fatigue of Ti6Al4V structural health monitoring systems produced by selective laser melting, Materials (Basel) 9 (2) (2016).

[17] N. Biswas, J.L. Ding, V.K. Balla, D.P. Field, A. Bandyopadhyay, Deformation and fracture behavior of laser processed dense and porous Ti6Al4V alloy under static and dynamic loading, Mater. Sci. Eng. A 549 (2012) 213–221.

[18] S. Beretta, S. Romano, A comparison of fatigue strength sensitivity to defects for materials manufactured by AM or traditional processes, Int. J. Fatigue 94 (2017) 178–191.

[19] V.T. Em, S.Y. Ivanov, I.D. Karpov, S.A. Rylov, E.V. Zemlyakov, K.D. Babkin, Residual stress measurements of laser metal deposited Ti- 6Al-4V parts using neutron diffraction, Journal of Physics: Conference Series, 1109 (1) (2018) 012049.

[20] Z. Wang, E. Denlinger, P. Michaleris, A.D. Stoica, D. Ma, M. Beese, Residual stress mapping in Inconel 625 fabricated through additive manufacturing: Method for neutron diffraction measurements to validate thermomechanical model predictions, Materials & Design, 113 (2017) 169-177.

[21] L. Sochalski-Kolbus, E.A. Payzant, P.A. Cornwell, T.R.Watkins, S.S. Babu, R.R. Dehoff, M. Lorenz, O. Ovchinnikova, C. Duty, Comparison of residual stresses in Inconel 718 simple parts made by electron beam melting and direct laser metal sintering, Metall Mater Trans A 46 (3) (2015) 1419-1432.

[22] V. Luzin, N. Hoye, Stress in thin wall structures made by layer additive manufacturing, Materials Research Proceedings, 2 (2016) 497–502.

[23] J.C. Heigel, P. Michaleris, E.W. Reutzel, Thermo-mechanical model development and validation of directed energy deposition additive manufacturing of Ti–6Al–4V, Addit. Manuf. 5 (2015) 9–19.

[24] R. Ye, J.E. Smugeresky, B. Zheng, Y. Zhou, E.J. Lavernia, Numerical modeling of the thermal behavior during the LENS® process, Mater. Sci. Eng. A 428 (1–2) (2006)47–53.

[25] S. Ghosh, J. Choi, Three-dimensional transient finite element analysis for residual stresses in the laser aided direct metal/material deposition process, J. Laser Appl.17 (2005) 144.

[26] G. Vastola, G. Zhang, Q.X. Pei, Y.W. Zhang, Controlling of residual stress in additive manufacturing of Ti6Al4V by finite element modeling, Addit. Manuf. 12 (2016) 231–239.

[27] H. Weiwei, J. Wenpeng, L. Haiyan, T. Huiping, K. Xinting, H. Yu, Research on preheating of titanium alloy powder in electron beam melting technology, Rare Metal Mater. Eng. 40 (12) (2011) 2072–2075.

[28] V. Chastand, P. Quaegebeur, W. Maia, E. Charkaluk, Comparative study of fatigue properties of Ti-6Al-4V specimens built by electron beam melting (EBM) and selective laser melting (SLM), Mater. Charact. 143 (2018) 76–81.

[29] Y. Zhai, H. Galarraga, D.A. Lados, Microstructure, static properties, and fatigue crack growth mechanisms in Ti-6Al-4V fabricated by additive manufacturing: LENS and EBM, Eng. Fail. Anal. 69 (2016) 3–14.

[30] L. N. Carter, M. M. Attallah, and R. C. Reed, "Laser Powder Bed Fabrication of Nickel-Base Superalloys: Influence of Parameters; Characterisation, Quantification and Mitigation of Cracking," in Superalloys 2012, ed: John Wiley & Sons, Inc., 2012, pp. 577-586.

VITA

Lan Li was born in Nanyang city, Henan province, China. She received her Bachelor of Science degree in Mechanical Engineering in July 2012 from Henan University of Science and Technology, Luoyang City, China. In July 2015, she received her Master of Science degree in Mechanical Engineering from Tianjin University of Commerce, Tianjin city, China. In July 2021, she received her Doctor of Philosophy in Mechanical Engineering from Missouri University of Science and Technology, Rolla, Missouri, USA. Her research interests included additive manufacturing, microstructure characterization, heat transfer simulation, stress and deformation prediction, laser metal deposition. During her Ph.D. study, she authored and co-authored seven journal papers, and four conference papers.